

Investigations on the Kinetics of Small Oxygen-Containing Radicals by Laser-Induced Fluorescence

zur Erlangung des akademischen Grades eines

DOKTORS DER NATURWISSENSCHAFTEN

(Dr. rer. nat.)

der Fakultät für Chemie und Biowissenschaften der

Universität Karlsruhe (TH)

angenommene

DISSERTATION

von

Dipl.-Chem.-Phys. Nikolina Kirilova Krasteva

aus Sofia, Bulgarien

Dekan: Prof. Dr. H. Puchta

Referent: Prof. Dr. H. Hippler

Korreferent: Prof. Dr. W. Freyland

Tag der mündlichen Prüfung: 13.12.2005

Contents

Zusammenfassung	5
1 Summary	7
2 Introduction	9
3 Experimental Part	13
3.1 Detection Technique. LIF.	13
3.2 Experimental Setup	16
3.2.1 The High-Pressure Cell	18
3.2.2 The Mixture Preparation	19
4 Theoretical Part	21
4.1 The Reaction Step	24
4.1.1 Tight Transition State	25
4.1.2 Loose Transition State	26
4.2 The Thermal Rate Constant	27
4.2.1 RRKM Model	27
4.2.2 Troe Formalism	30
4.2.3 Master Equation Analysis	32
4.2.4 Complex Forming Bimolecular Reactions	34
4.2.5 Non - Statistical Models	37
5 The Decomposition of Formyl Radicals	39
5.1 Introduction	39
5.2 Experimental Details	45

5.2.1	Generation and Detection of Formyl Radicals	45
5.2.2	Temperature Control	46
5.3	Experimental Results	47
5.4	Discussion	50
5.4.1	Effects of the State Specific Rate Constant on $k(T,[M])$. .	51
5.4.1.1	Statistical Models	51
	RRKM Model	51
	Troe Formalism	53
	Master Equation Analysis	54
5.4.1.2	Non - Statistical Model	56
5.4.2	Falloff in Different Bath Gases	66
5.4.2.1	Falloff in He	66
5.4.2.2	Falloff in Ar	72
5.4.2.3	Falloff in N ₂	73
5.4.3	Isotope Effect	75
5.5	Conclusions	79
5.6	Outlook	80
6	The Recombination of CH₂CHO and O₂	81
6.1	Introduction	81
6.2	Experimental Details	86
6.3	Experimental results	87
6.3.1	Low Temperature Range	87
6.3.2	Intermediate Temperature Range	89
6.3.3	High Temperature Range	91
6.4	Discussions	92
6.4.1	The Reaction Threshold	93
6.4.1.1	The Recombination Barrier.	94
6.4.1.2	The Reaction Enthalpy	94
6.4.1.3	The Isomerization Barrier	96
6.4.2	Pressure Dependence of the Rate Constant	98
6.4.2.1	The High Pressure Range	105
6.4.2.2	The Low Pressure Range	107

6.4.2.3	The Low Pressure Addition Rate Constant . . .	109
6.4.2.4	The Broadening Factor	110
6.5	Conclusions	112
7	Appendix	115
7.1	Experimental Results for the HCO Decomposition	115
7.2	Parameters for Analysis of the HCO Decomposition	125
7.3	Experimental Results for the DCO Decomposition	126
7.4	Parameters for Analysis of the DCO Decomposition	128
7.5	Experimental Results for the Reaction of CH ₂ CHO and O ₂	129
7.6	Parameters for Analysis of the Reaction of CH ₂ CHO and O ₂ . . .	132
	Bibliography	133
	Acknowledgments	141
	Curriculum Vitae	143

Zusammenfassung

In der vorliegenden Arbeit werden experimentelle Untersuchungen von Reaktionen in der Gasphase unter Hochdruckbedingungen vorgestellt. Während zur Analyse experimenteller Daten im allgemeinen statistische Theorien geeignet sind, zeigen die Ergebnisse dieser Arbeit einige Einschränkungen statistischer Modelle und ferner die Komplexität der Reaktionskinetik auf.

Im ersten Teil werden experimentelle Untersuchungen zum thermischen Zerfall des Formylradikals (HCO / DCO) über weite Temperatur- und Druckbereiche vorgestellt. Es war nicht möglich, die experimentellen Daten lückenlos mit statistischen Modellen zu beschreiben. Die beobachtete Druckabhängigkeit der Geschwindigkeitskonstanten für den thermischen Zerfall konnte hingegen mit einem isolierten Resonanzmodell beschrieben werden, welches die nicht-statistische mikroskopische Kinetik von HCO und DCO berücksichtigt. Ein Vergleich der Geschwindigkeitskonstanten für die thermischen Zerfälle von HCO und DCO zeigt, dass diese trotz unterschiedlicher mikroskopischer Dynamik der Radikale mit dem gleichen Modell wiedergegeben werden konnten.

Im zweiten Teil der Arbeit wurden Untersuchungen zur Rekombination des Vinoxylradikals mit molekularem Sauerstoff vorgelegt. Diese bestätigen, daß die Reaktion über ein komplexbildendes Intermediat verläuft, im Gegensatz zum bisher angenommenen einfachen Additionsmechanismus. Die sich anschließende Kinetik wurde aus dem Verhältnis zwischen Folgereaktionen und Stabilisierungsprozessen bestimmt. Wichtige Parameter für die Analyse sind dabei die Potentialfläche und die Energieübertragungsprozesse. Experimentelle Untersuchungen der Hochdruckgeschwindigkeitskonstanten in einem weiten Temperaturbereich und ein Vergleich mit *ab initio*-Rechnungen erlaubte die Bestimmung thermochemischer Daten. Damit und mit detaillierten statistischen Verfahren war eine Beschreibung des Falloff-Verhaltens der Geschwindigkeitskonstante für die Rekombination möglich. Eine weitere Parametrisierung führte zu einfachen analytischen Ausdrücken, welche für Modellierungen in der Atmosphären- und Verbrennungschemie verwendet werden können.

Chapter 1

Summary

A general objective of this work is to provide experimental data on the kinetics of gas phase reactions under high-pressure conditions. Statistical rate theories have proved to be a powerful tool for the analysis of kinetic data, yet the results from this work reveal some restrictions of statistical models and the complexity of the reaction kinetics.

The first part presents experimental investigations on the thermal decomposition of the formyl radical (HCO / DCO) in wide temperature and pressure ranges. It was not possible to represent the experimental data accurately with statistical models. However, an isolated resonance model, which takes into account the non-statistical microscopic kinetics of HCO / DCO radicals, allowed for a representation of the observed pressure dependence of their thermal decomposition rate constants. A comparison between the thermal decomposition rate constants of HCO and DCO, shows that these can be represented with the same model in spite of the different microscopic dynamics of the radicals.

The investigations on the recombination of vinoxy radicals (CH_2CHO) with molecular oxygen presented in the second part of this work show, that this reaction proceeds via a complex formation, as opposed to the simple addition mechanism assumed in previous experimental studies. The overall kinetics is determined by the competition between a consecutive unimolecular reactions of the complex and its collisional stabilization. Crucial features for the analysis are the potential energy surface and the energy transfer processes. Experimental determination of the

high-pressure rate constants in a wide temperature range and comparison of the results with *ab initio* calculations allowed for the determination of thermochemical data. With these as input parameters and detailed statistical approaches it was possible to reproduce the falloff behavior of the recombination rate constant. Further parametrization of the results yielded simple analytical expressions, which are recommended for atmospheric and combustion modeling.

Chapter 2

Introduction

Simulations of unsteady combustion processes, considering variable temperature and pressure gradients, require data on the kinetics of elementary reactions in wide ranges of experimental conditions. In the last years the non-statistical behavior of the microscopic kinetics ($k(E)$) of two- and three- atomic species (e.g. HCO, DCO, HO₂, HNO etc.), associated with their low density of states, is a subject of discussions (for summary see Ref. [1]).

The thermal decomposition of the formyl (HCO) radicals under low temperature combustion conditions is a main objective of this work. Due to the low dissociation barrier, the competition between the HCO dissociation, which is a chain carrier, and bimolecular reactions with e.g. H, OH, O₂, leading to chain termination, is critical for the combustion dynamics.

The HCO dissociation is interesting from a theoretical point of view as well. Statistical rate theories are based on the ergodic assumption, which postulates fast internal vibrational energy redistribution (IVR) above the reaction barrier. This requires a large number of states per energy interval, which allows to approximate the specific rate constant $k(E)$ by statistical (average) functions, increasing with energy. In HCO / DCO radicals isolated resonance states exist above their dissociation barriers [1,2], which leads to weak mode coupling and hence to slow IVR. These cause fluctuations of the specific rate constants by orders of magnitude from resonance to resonance, depending on the modes which are excited (mode specificity). Furthermore, the dynamics of HCO is strictly mode specific, while this of

DCO is non-regular, mainly due to vibrational coupling effects.

As opposed to numerous studies on non-statistical effects in the microscopic dynamics of the radicals, there is no experimental confirmation for such effects on their macroscopic decomposition rate constant ($k(T, [M])$), which is of practical relevance. Comparison between the kinetics of the two radicals allows to test if *i) the fluctuating lifetimes of the resonance states* and *ii) the mode specificity* cause deviations from statistical predictions on their thermal decomposition rate constant. There are three direct studies on the formyl (HCO) decomposition at combustion relevant temperatures [3, 4, 5]. Timonen et al. [3] investigated the decomposition rate constant at pressures of few mbar, while the measurements from Refs. [4, 5] were performed in overlapping pressure ranges (≈ 1 bar). Based on a comparison of the second order rate constants from Refs. [3, 4, 5], Krasnoperov et al. [5] reported discrepancies between the results from Ref. [3] and Refs. [4, 5] by a factor 2.2 to 3.5. Possible falloff effects (deviations from the assumed linear dependence of the rate constant on pressure) have not been discussed. Statistical models predict that the rate constant for the formyl decomposition is in the low pressure limit in this experimental range (e. g. up to $p = 2$ bar [4]), which has been widely accepted for modeling till now. Theoretical investigations from Refs. [6, 7] predict deviations of $k(T, [M])$ from the linear range at much lower pressures (e. g. at $p > 1$ mbar in Ref. [7]), due to the non-statistical microscopic dynamics of the radical. Yet there is still no explicit experimental confirmation of such effects.

This work presents investigations on the decomposition of the HCO / DCO radicals under low temperature combustion conditions ($T < 800$ K, $p < 200$ bar). The experimental results are compared to statistical models, as well as to an isolated resonance model, which takes into account the fluctuations of $k(E)$.

Another goal of this study is to find a theoretical description of the experimental results and to identify if the non-statistical specific decomposition rates ($k(E)$) influence the thermal rate constant ($k(T, [M])$). This would provide accurate information on their dissociation kinetics, as well as simple analytical expressions, which can be directly used for modeling.

In recent years, progress has been made in understanding the kinetics of complex-forming association reactions. These are in general reactions of reactive species (radicals) with stable molecules, in which a complex with a finite lifetime is

formed (chemical activation). The lifetime is comparable to the timescale of reaction and stabilization processes, hence the competition between these introduce a complicated temperature and pressure dependence.

It has been shown that (for summary see Ref. [8]) the chemical activation is important for the chemistry of some alkoxy radicals in the atmosphere. The second part of this work presents investigations on the recombination of vinoxy radicals (CH_2CHO) with O_2 . The CH_2CHO radical is an important intermediate in atmospheric and combustion processes (see e. g. [9, 10, 11]). Due to the relatively high oxygen concentrations under practical relevant environments, the above reaction is the main oxidation pathway for CH_2CHO [12, 13].

The scarce experimental investigations on the kinetics of the above reaction [12, 13, 14, 15] do not allow for a reliable theoretical modeling. These adopt a simple addition mechanism for the data interpretation, while theoretical calculations do not exclude the possibility of complex formation. The mechanism and the kinetics of the complex-forming reactions are very sensitive to the reaction channel barriers (see e. g. [8]), since these have in general comparable heights. Unfortunately these barriers are still not calculated with sufficient accuracy, hence experimental confirmation of the results is necessary.

This work presents investigations of the recombination of vinoxy radicals with O_2 in broad temperature and pressure ranges ($T = 298 - 660\text{K}$, $p = 1 - 50\text{bar}$). Experimental data on the high-pressure rate constant at high temperatures allow for a direct access to the rate determining reaction barriers. Comparison of these data to *ab initio* calculations [16] yields reliable information on the potential energy surface.

The molecular parameters (vibrational frequencies, rotational constants) obtained by *ab initio* calculations [16] can be adjusted to represent the experimental results as well. The obtained parameters are used for modeling of the falloff behavior of the title reaction with detailed statistical approaches (e.g. Master Equation [16]). Further parametrization of the results yields simple analytical expressions for the rate constant, which can be directly used for modeling.

Chapter 3

Experimental Part

3.1 Detection Technique. LIF.

The detection of radical species under high pressure conditions demands experimental techniques capable of detecting low concentrations selectively.

The disadvantage of *absorption based approaches* is the relatively low selectivity - the absorption spectra of different species might be in similar spectral ranges. To get reliable data modeling of the observed signals is necessary, which introduces uncertainty in the data interpretation.

The response of non-resonant *Raman scattering* [17] is fast and thus insensitive to quenching (loss) processes, due to the short lifetime of the excited states. Disadvantage of this approach is its low cross section, due to which the emitted signals are weak.

The high spectral selectivity and sensitivity (large absorption cross sections) of the *laser induced fluorescence (LIF)* make it a premier candidate for detection of radical species under high pressure conditions.

Laser Induced Fluorescence

Laser Induced Fluorescence (LIF) for detection of species under high pressure conditions has been established in the group of Prof. H. Hippler [18, 19]. The basic concepts of this detection method are described in the literature [17], so

only a brief description of a simplified two-level model, which is schematically presented in Fig. 3.1, will be discussed.

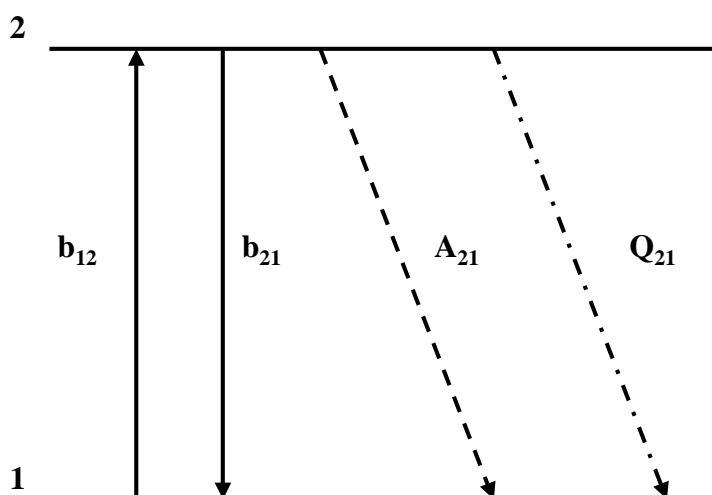


Figure 3.1: Two level energy diagram for a qualitative description of LIF.

As shown in Fig. 3.1, initially an electron is excited from level 1 to level 2 by stimulated absorption of a photon. The rate coefficient of this process is given by b_{12} , which is related to the Einstein coefficient B_{12} ($b_{ij} = B_{ij}I_{\nu}/c$, where I_{ν} is the spectral intensity of the laser beam and c is the light speed). The spontaneous emission of a photon, due to which the excited electron falls back to level 1, is called fluorescence, characterized by the Einstein coefficient A_{21} . Parallel to spontaneous emission, different competition processes take place. The absorption process can be followed by a stimulated emission of a photon (b_{21}). The absorbed energy might be lost in concurrent radiationless transitions, such as energy transfer to other species by collisions, in which no emission of photons is observed. The last are termed as quenching processes and are characterized by pseudo-first order rate coefficient Q_{21} .

In order to derive the dependence of the fluorescence intensity on the external conditions some approximations are made [17]. It is assumed that prior to laser excitation all the electrons are in level 1, and in the course of laser excitation steady state

among the absorption and emission processes is reached. Furthermore the laser linewidth is stated to be equal or larger than the absorption linewidth (in general pressure broadening is not accounted for). Applying these approximations and considering that the rates of the stimulated processes are proportional to the laser intensity, one can show that the fluorescence intensity is related to the Einstein coefficient for spontaneous emission and the population of state 2 [17, 20]:

$$F \propto N_2 A_{21} \propto N_1^0 \frac{B_{12}}{B_{12} + B_{21}} \frac{1}{1 + \frac{I_v^{sat}}{I_v}} A_{21} \quad (3.1)$$

Eq. 3.1 relates F also to the initial population of level 1 (N_1^0). F depends on the laser intensity I_v and the saturation spectral intensity I_v^{sat} , defined as:

$$I_v^{sat} = \frac{(A_{21} + Q_{21})c}{B_{12} + B_{21}}, \quad (3.2)$$

For quantitative measurements one should consider the signal loss due to reflection and quenching processes. Q_{21} depends on the quenching partner and the temperature. It is known for some species at given external conditions, but in general no sufficient information on this are available [17].

Considering Eq. 3.1 one can distinguish two limiting cases:

$I_v \ll I_v^{sat}$ - linear regime:

$$F \sim N_1^0 \frac{B_{12}}{B_{12} + B_{21}} \frac{I_v}{I_v^{sat}} A_{21} \quad (3.3)$$

The fluorescence intensity is proportional to the population of the excited state and hence to the intensity of the laser beam.

$I_v \gg I_v^{sat}$ - saturated regime:

$$F \sim N_1^0 \frac{B_{12}}{B_{12} + B_{21}} A_{21} \quad (3.4)$$

At higher laser intensities a regime of saturation is reached. Due to the equilibrium population distribution between the excited and the ground states, the rates of the stimulated processes dominate. The advantages of the saturation regime are clear: the fluorescence signal is maximal and independent on the fluctuations of the ex-

citation laser energy, which leads to an optimal signal to noise ratio. Furthermore, the dependence of the fluorescence signal on the quenching rate constant, which is usually unknown, is eliminated.

To reach a regime of saturation one needs laser energies higher than the characteristic saturation intensity I_v^{sat} , which is proportional to the quenching rate and hence to the type and the concentration of the detected species and the collision partner(s). In experiments under high pressure conditions the concentrations of the bath gases are high. In order to reach saturation regime at lower laser intensities one chooses inefficient collision partners as He and Ar [19, 21, 22, 23]. In this work N_2 has been used as well.

A consequence of the absorption process is that the photon is not irradiated instantly but with a time delay with respect to the absorption, which depends on the lifetime of the excited state of the molecule. In this work transitions between electronic levels of the detected radicals were employed. The longer lifetimes of vibrationally and rotationally excited states makes them difficult for detection under high pressure conditions since the quenching processes, whose rate depends on the concentration of the collision partner, occur prior to fluorescence.

3.2 Experimental Setup

The experimental conditions in this work ($p < 1000$ bar, $T < 1000$ K) demand a special experimental configuration. The experimental setup employed for the investigations presented in this work is schematically given in Fig. 3.2.

The measurements were performed in a T - shaped high pressure cell, supplied with three windows (Suprasil I). The photolysis and excitation laser beams counterpropagated coaxially through two of the cell windows, while the LIF signal was collected perpendicularly through the third one. This construction, as well as the additionally used monochromator (Zeiss, M4 QIII), allowed minimization of the scattered light. The detector was a photomultiplier tube (Hamamatsu R212 / Hamamatsu 1P28). The obtained output voltage was amplified (Stanford Research System SR240), integrated over a definite time interval (Stanford Research System SR250) and digitalized (Stanford Research System SR245) and transferred to a computer interface via a GPIB card.

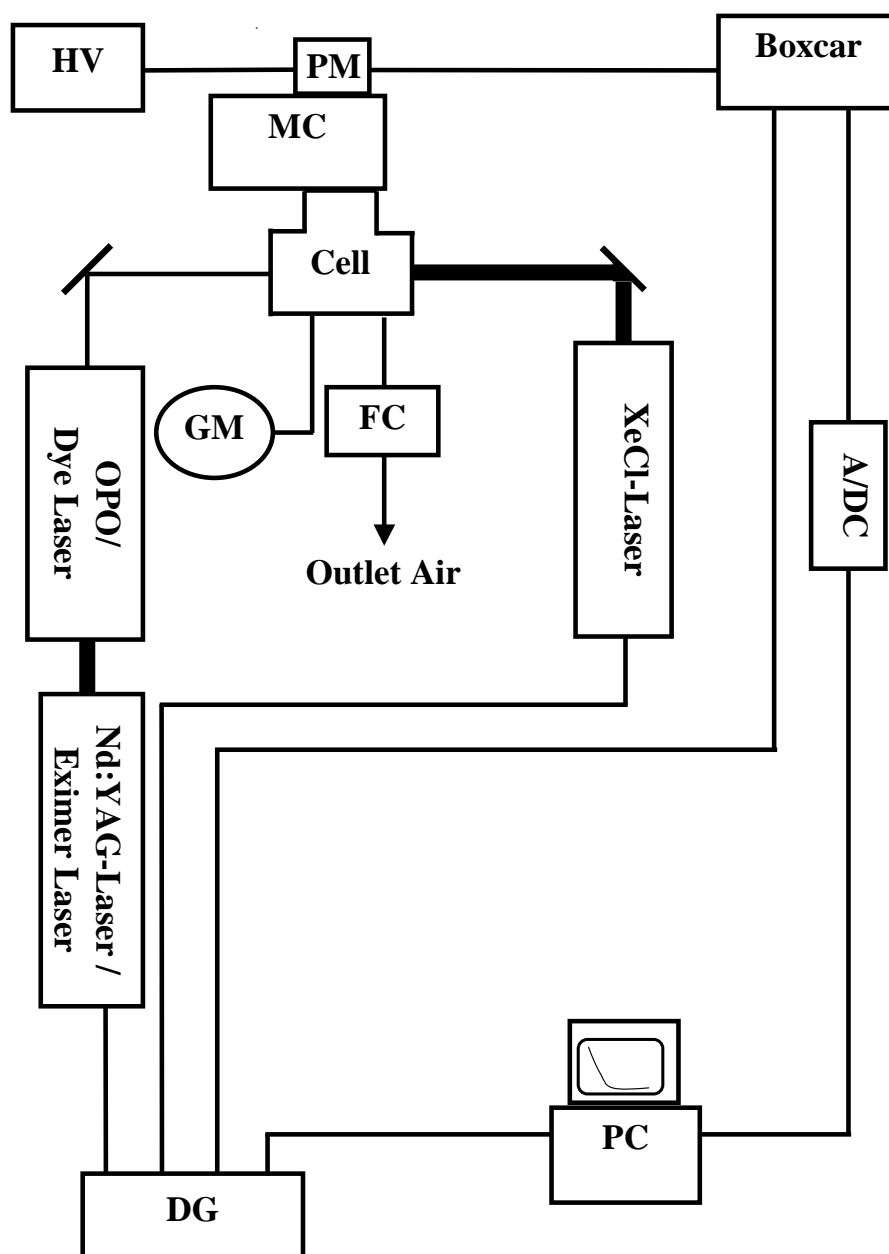


Figure 3.2: Setup of the high pressure system. Legend: HV - High Voltage, PMT - Photomultiplier, MC - Monochromator, Boxcar - Boxcar Integrator, GM - Gas Mixture, DG - Delay Generator, ADC - A/D Converter, FC - Flow Controller

An internally triggered Delay Generator (DG535) controlled the delay between the photolysis and the excitation lasers. Furthermore it triggered a boxcar to integrate over a time interval defined by the boxcar integrator. The delay generator (DG) was controlled by a personal computer (program package LabView). In the experiments where the OPO was used as a probe laser, the variation of its repetition rate required a second delay generator. The reason is that the pump Nd:YAG laser was constructed for a repetition rate of 10 Hz, which assured an optimal temperature profile in the Nd:YAG crystals. A home-built frequency divider was used to keep the repetition rate of the flash lamps for the Nd: YAG laser at 10 Hz, and split the frequency of the Q - switch.

The gas mixtures flew perpendicularly to the plane defined by the three windows of the cell, through 2 separate bores. The flow rate was controlled by a flow meter (Bronkhorst, F-231M-FAC-33-P). Two thermocouples were used to measure the temperature in the reactor.

The experiments were performed under flow (quasi - stationary) conditions. The flow rate was high enough to assure that reaction (photolysis) products do not interfere the observed concentration decays. Still this allowed thermal equilibrium conditions in the reaction volume (within 10 K temperature gradient).

3.2.1 The High-Pressure Cell

The stainless steel cell (material RGT 601) used in this work allows measurements up to temperatures of 1000 K and pressures of 1000 bar (Fig. 3.3).

The cylindrical cell has a diameter of about 7 cm (9 cm including the heating coating), which allows preheating of the gas mixture before reaching the reaction zone. The cell volume (1.5 cm^3) was enclosed by three windows (Suprasil I, diameter and length = 10 mm, Heraeus), built in three bored holes. The windows were placed in windows caps and fixed to the stamp with a graphite seal. The construction of the cell and the sealing are described in detail in [22].

The reaction volume (about 0.2 cm^3) is determined from the profile of the photolysis laser beam in the cell (diameter $\approx 0.5 \text{ cm}$, length = 1.2 cm). Two thermocouples, implemented in the high-pressure capillaries, allowed for an accurate determination of the temperature in the reaction zone.

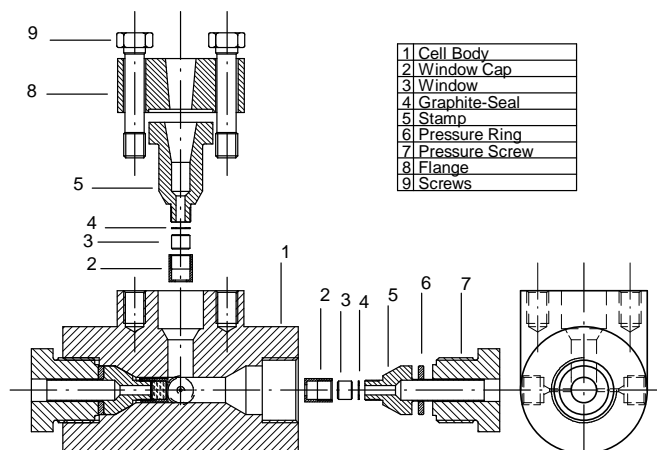


Figure 3.3: The high pressure cell. For a detailed description see Ref. [22].

3.2.2 The Mixture Preparation

The reactivity of the radical species being detected in this work demanded mixtures with high purity and, for reactions performed under pseudo first order conditions, an exact determination of concentrations of the reaction partners. The setup consisted of a low- and a high- pressure sections, as shown in Fig. 3.4. The low pressure section contained a stainless steel tube with several KF-16 ports. This connected the mixing bottle (Messer Griesheim, 40 dm³, 300 bar) with a rotary vane pump (VakUUbrand RD-4) and a pressure gauge (Pfeiffer Compact Capacitance Gauge, Type CMR 263, 0.001-10 mbar, digital read out system - Pfeiffer Single Gauge Type 251A). Prior to mixture preparation, the bottles were evacuated to a pressure of less than 10⁻⁵ bar, after which the radical precursor and the reaction partners were allowed to flow in. Careful control of the pressure allowed a determination of the initial concentrations of the reactants. The bottles were then connected to the high-pressure part of the setup and filled with the collision partner to the desired pressure (max 200 bar).

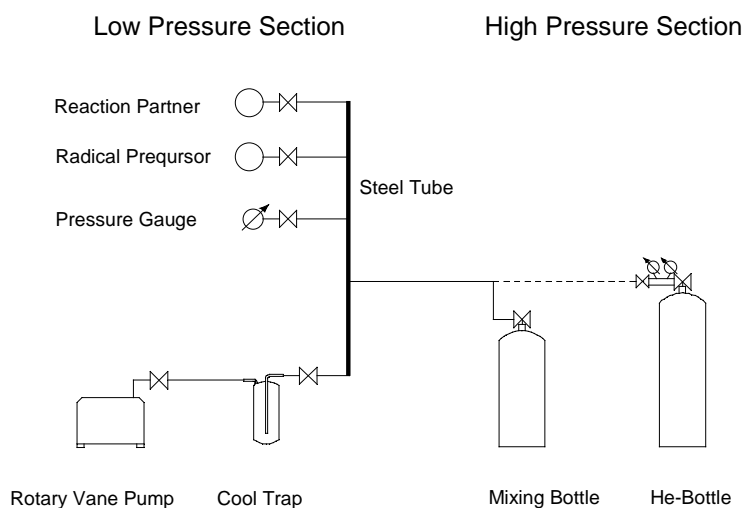


Figure 3.4: Schematic representation of the setup used for preparation of the high-pressure mixtures.

The mixtures were left for at least 12 hours to homogenize, which has been proved to be sufficient for complete mixing (e.g. [21, 24]). The chemicals used are listed in Table 3.1.

Table 3.1: Chemicals used for mixture preparation. The radical precursors were degassed several times prior to use. Reaction partners and bath gases were used without further purification.

Chemical	Manufacturer	Purity [%]
CH ₃ CHO	Roth	> 99.5
CD ₃ CDO	Sigma	> 99.0
C ₂ H ₅ OC ₂ H ₅	Merck	> 99.0
O ₂	Messer Griesheim	> 99.995
He	Messer Griesheim	> 99.999
N ₂	Messer Griesheim	> 99.996
Ar	Messer Griesheim	> 99.999

Chapter 4

Theoretical Part

The discussions in the following sections are concentrated on the theoretical background of unimolecular reactions. These are related to the respective recombination reactions by the principle of microscopic reversibility. Some details on the kinetics of complex forming reactions are presented as well.

The first step toward understanding of the pressure dependence of unimolecular reactions is the recognition from Lindemann in 1922, that these can be separated into activation and reaction steps [25]. Weaknesses of this model are: *i*) Concerning the activation step, it is assumed that each collision leads to activation / deactivation of a molecule (strong collision assumption); *ii*) The energy dependence of the rate of the reaction step (R 4.3) is not accounted for.

The model was further developed by Hinshelwood, who considered both effects. The Lindemann - Hinshelwood model for unimolecular reactions can be presented by the following mechanism:



In R 4.1 a molecule A is activated by collision with a bath gas molecule M. The activated molecule A*(E) can be deactivated by another collision with M (R 4.2). In general large number of collisions take place until a sufficient amount of

energy is accumulated in the molecule to allow for reaction (R 4.3), characterized by a rate constant $k_2(E)$.

The microscopic rates of these processes depend except on the energy also on the rotational excitation of the molecule (J). At first, for simplicity, rotational excitation will be neglected in the discussions.

In order to visualize the processes discussed above, these are schematically presented in Fig. 4.1 for a two channel reaction:

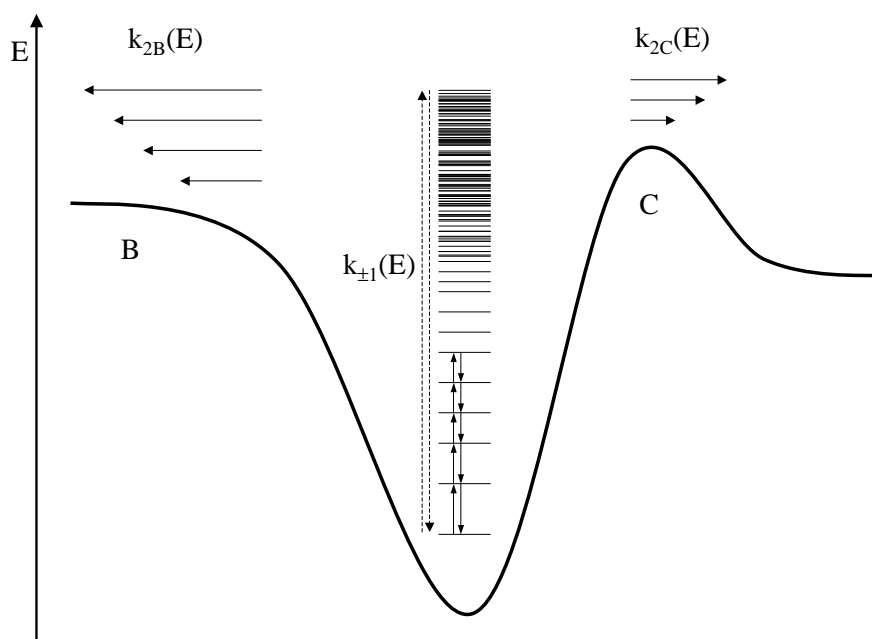


Figure 4.1: The competition between energy transfer and reaction processes. Tight and loose transition states. See text for further discussions.

The solid curve represents the variation of the potential energy along the reaction coordinate for a reaction with two possible transition states (B and C). The energy levels of the reactant are presented by horizontal lines. The corresponding rates of collisional energy transfer between these are labeled with $k_{\pm 1}(E)$ for up and down transitions, respectively. The reaction rates along the two possible transition states are indicated by $k_{2B}(E)$ and $k_{2C}(E)$.

The overall reaction rate is determined by the competition between the processes of collisional excitation / deactivation ($k_{\pm 1}(E)$) and, reaction, with a rate constant $k_2(E)$.

It is difficult to describe the microscopic dynamics even for the simplest reactions, but this problem is overcome if one considers the statistical properties of the processes described above. The statistical approaches used to calculate the unimolecular reaction rate are based on two assumptions:

Ergodicity Assumption. This postulates, that the internal energy of a molecule is redistributed statistically among its internal degrees of freedom prior to any other dynamical processes.

In the energy range above the threshold, which is of interest for the reaction kinetics, the density of states is in general very high. This allows fast energy flow between the vibrational modes of the reaction species and strong coupling between the reaction coordinate and the other degrees of freedom. Hence the reaction rate can be calculated from the statistical properties of the equilibrium distribution of states;

Transition State (TS) Assumption. This postulates the existence of a critical surface along the reaction coordinate, and any trajectory passing through it leads to product formation, without recrossing this so called transition state.

In order to calculate the thermal rate constant as a function of the pressure, one has to determine the population of the different energy levels ($N(E)$) considering the energy transfer and reaction processes (Eq. 4.1).

$$k(T, p) = \int_{E=E_0}^{\infty} N(E)k_2(E)dE \quad (4.1)$$

In order to solve Eq. 4.1, one needs information of the energy dependence of the reaction rate $k_2(E)$ for energy interval dE , the models for which will be discussed below. Furthermore, this requires a proper energy weighting of the population distribution $N(E)$, depending on the macroscopic factors like the temperature and pressure. There is a direct connection between the energy distribution and the temperature. The pressure dependence of the rate constant arises because the population, maintained by collisional energy transfer, is depleted relative to the

thermal population by reaction processes (except, as shown below, in the high-pressure limit).

In the following sections first the models used to calculate the rate constant of the reaction step (R 4.3) will be discussed, and then the ones used to estimate the population distribution. Integration of these over the energy gives the overall thermal rate constant (see Eq. 4.1).

4.1 The Reaction Step

In general the rate of the reaction step is given by the following expression [25,26]:

$$k(E) = \frac{W^\ddagger(E - E_0)}{h \cdot \rho(E)} \quad (4.2)$$

where $\rho(E)$ the density of states of the reactant, defined as the number of states per energy interval, and h the Planck's constant. $W^\ddagger(E - E_0)$ is the number of "open channels", which lead to reaction, or the number of internal states in the TS with energy higher than the dissociation threshold. $1/h\rho(E)$ gives the reaction rate through a single open channel, which, multiplied by the number of open channels $W^\ddagger(E - E_0)$ determines the rate of the reaction step.

Until the 1970's, the density of states have been mainly approximated with analytical expressions (e.g. Whitten - Rabinovitch Approximation [27]) and the quantization of the vibrational energy levels has been neglected. In 1973 Beyer and Swineheart developed mathematically a direct count algorithm (Beyer - Swineheart - Algorithm [26]), which has been widely used to count the harmonic density of states. Approximating a molecule as a harmonic oscillator introduces some uncertainty in the calculations. In some models additional corrections for anharmonicity and rotational / vibrational coupling are included.

In order to calculate the $W^\ddagger(E - E_0)$, one considers two types of transition states (TS), shown in Fig. 4.1 with B and C, respectively: *loose* - there is not a defined barrier (TS) for the reaction; *tight* - there is a fixed maximum in the potential along the reaction coordinate.

$W^\ddagger(E - E_0)$ depends strongly on the properties and the position of the transition

state. In the discussions till now only the dependence of the microscopic rate coefficients on the energy has been considered. One should keep in mind, that these depend also on the angular momentum of the reaction species. This is assumed to be conserved by the motion along the transition state, but the rotational energy still varies since the geometry of the molecule changes. This causes additional centrifugal barriers, which depend on the angular momentum of the molecule J [26]. Except for very high J , the centrifugal barrier is in general positioned near the barrier for reaction [26]. For reactions with tight transition states, the significant chemical barrier dominates the rotational term and determines the potential maximum. The effect is stronger in reactions with loose transition states, in which the differences between the geometry of the transition state and the reactants is significant. In this case the contributions from rotational excitation are important for the position and the barrier height of the transition state, due to the low chemical barrier.

Some of the models used to calculate the number of open channels for the two types of transition states shown in Fig. 4.1 will be shortly discussed in the following sections.

4.1.1 Tight Transition State

An approach, which is widely used to describe the microscopic rate coefficients for reactions which proceed via a tight TS, is the Rice - Ramsperger - Kassel - Marcus (RRKM) model [26, 28, 29, 30].

The ergodicity assumption postulates a fast energy flow due to a strong coupling between the reaction coordinate and the other vibrational degrees of freedom. The reaction rate is calculated for modes which participate in the reaction process, i. e. their energy can flow into the reaction coordinate and allow for the molecule to react ("active" degrees of freedom). The modes which stay unchanged (conserved) during the reaction process have no influence on the reaction rate. In general all of the vibrational modes are considered as active, while the treatment of rotational degrees of freedom depends on the reaction under consideration.

The zero point energies (E_z) of the reaction species can not be redistributed to the reaction coordinate [1], i. e. this is always "conserved". Hence E_z for the reactants

and the transition state should be excluded from the energy available for reaction. According to the RRKM model, $W^\ddagger(E - E_0)$ is equal to the sum of states in the transition state, which have an energy that is equal to or higher than the dissociation barrier. In order to estimate the number of open channels one can use similar approaches as those used for the calculations of the density of states. For more details see Sec. 4.1 and Refs. [25, 26, 29].

The reaction species are approximated as harmonic oscillators and their energy and angular momentum as conserved quantities. In reality rotational effects as the centrifugal barriers or anharmonic effects as rotational - vibrational (Coriolis) coupling affect the reaction and stabilization processes. As stated above, the centrifugal barriers are more important for reactions with loose TS.

The coupling between the rotational and vibrational modes (Coriolis coupling) allows an energy flow between these, which is restricted by the energy conservation law. The total rotational energy of a molecule is related to its three moments of inertia (I_x, I_y, I_z) [1]. One can approximate a molecule as a "symmetric" top, if two of its moments of inertia have similar magnitude, which differ from the third one. In general the rotation along the degenerate axes is accounted for by the quantum number K , and along the symmetry axis - by J . In general one assumes that J is an active degree of freedom, while the K rotor can be treated as an active or adiabatic degree of freedom, respectively for strong or weak Coriolis coupling [1, 26, 31].

4.1.2 Loose Transition State

As stated above the position and the barrier height for reactions with loose TS are very sensitive to the available angular momentum.

Wide practical applications for description of the kinetics of this class of reactions is a simplified Statistical Adiabatic Channel Model (SACM). In its original version [32], the molecular modes are assumed to be conserved along the reaction path, and the reaction channels to be *adiabatic* - i. e. the reaction takes place from a defined reactant state to a defined product state, characterized with one set of quantum numbers. The modes which are similar for the reactant and the product stay in the same quantum state during the reaction process. The calculations are performed for reaction coordinate, which is assumed to be separated from all

other molecular motions. The channels are considered as open if there is a sufficient amount of energy for the reactants to overcome the channel barrier for a specified J .

For the model it is important that the adiabatic assumption is valid on average, even if the individual reaction channels are not strictly adiabatic. Exact SACM calculations are possible only for small species, since the adiabatic channels have to be calculated for each quantum state of the reactant, considering the available energy and angular momentum.

The simplified version of this model (s - SACM) has been developed by Troe [33, 34]. In this, the number of open channels is determined by an interpolation of the reaction channels between the product and reactant states. The reaction coordinate is in general approximated as a Morse potential [33, 34].

4.2 The Thermal Rate Constant

Let's consider again the Lindemann - Hinshelwood mechanism. Solving the rate equations for this with the steady state approximation for $[A^*(E)]$ [1, 26] one obtains the following equation for the specific rate constant [25, 30]:

$$k_{uni}(E)dE = k_{-1}(E)[M] \frac{k_2(E)[k_1(E)/k_{-1}(E)]}{k_{-1}(E)[M] + k_2(E)} dE \quad (4.3)$$

In order to integrate this equation one needs a properly weighting of the rate coefficients among the energy. The experimental data gives information on the rate constant as a function of the temperature and pressure, which are macroscopic factors. Different levels of theory are used to calculate the overall thermal rate constant as a function of these.

4.2.1 RRKM Model

An approach which is directly associated with Eq. 4.3 is the Rice - Ramsperger - Kassel - Marcus (RRKM) model. Here one calculates the strong collision rate constant (as shown with vertical dashed arrows in Fig. 4.1), and the weak collision effects are considered by multiplication with a correction factor.

The models used to calculate $k_2(E)$ have been already discussed.

As stated above, in order to determine the thermal rate constant (see Eq. 4.1) one needs the population distribution. Applying the steady state approximation for $[A^*(E)]$ for the Lindemann - Hinshelwood mechanism, this can be expressed as:

$$N(E) = \frac{[A^*(E)]}{[A]} = \frac{k_1(E)[M]}{k_{-1}(E)[M] + k_2(E)} \quad (4.4)$$

At high pressures ($k_{-1}(E)[M] \gg k_2(E)$) a rapid pre - equilibrium is reached:

$$N(E) = \frac{[A^*(E)]}{[A]} = \frac{k_1(E)}{k_{-1}(E)} = \frac{\rho(E) \exp\left(-\frac{E}{k_B T}\right)}{Q_{vib}} \quad (4.5)$$

where Q_{vib} is the vibrational partition function of the reactant [25].

If the pressure is decreased, the equilibrium population between $[A]$ and $[A^*(E)]$ is depleted by the reaction. The highly excited $A^*(E)$ react faster, since their $k_2(E)$ is higher, which introduces pressure dependence of the population (and hence of the rate constant).

As seen from reaction R 4.2 in the Lindemann - Hinshelwood mechanism, $k_{-1}(E)$ is the rate constant for deactivation of the molecule. In general the deactivation is an efficient process, which shows a weak energy dependence. $k_{-1}(E)$ is approximated with βZ , where Z is the overall collisional frequency [25] and β is a collision efficiency factor, which allows for weak collision effects.

Substituting these approximations in Eq. 4.3, one gets the following expression for the thermal rate constant:

$$k(T, [M]) = \frac{\beta Z [M]}{Q_{vib}} \cdot \int_{E=E_0}^{\infty} \frac{k_2(E) \rho(E) \exp\left(-\frac{E}{k_B T}\right)}{k_2(E) + \beta Z [M]} dE \quad (4.6)$$

In this $[M]$ is the concentration of the bath gas, which is proportional to the pressure. From Eq. 4.6 one can distinguish two limiting cases:

Low Pressure Range: $k_2(E) \gg Z[M]$:

$$k_0(T, [M]) = \frac{\beta Z[M]}{Q_{vib}} \int_{E=E_0}^{\infty} \rho(E) \exp\left(-\frac{E}{k_B T}\right) dE \quad (4.7)$$

The low pressure rate constant $k_0(T, [M])$ depends on the density of states of the reactant and the rate of the energy transfer processes. In this limit the rate constant contains information on the energy transfer processes, but not on the reaction step, since under these conditions once the molecule reaches the dissociation threshold it reacts further. As seen from Eq. 4.7 in $k_0(T, [M])$ increases linearly with pressure ($[M]$).

High Pressure Range: $k_2(E) \ll Z [M]$:

$$k_{\infty}(T) = \frac{1}{Q_{vib}} \int_{E=E_0}^{\infty} k_2(E) \rho(E) \exp\left(-\frac{E}{k_B T}\right) dE \quad (4.8)$$

In the high-pressure regime the Boltzmann distribution can not be depleted by reaction, due to the large number of collisions, which maintain it. In this range the kinetics depends on the rate of the reaction step, but not on the bimolecular energy transfer processes. $k_{\infty}(T)$ is pressure independent, and, substituting the Boltzmann distribution function [25, 26] in Eq. 4.8, one receives the standard transition state expression (Eq. 4.9):

$$k_{\infty}(T) = \frac{k_B T}{h} \frac{Q_{vib}^{\ddagger}}{Q_{vib}} \exp\left(-\frac{E_0}{k_B T}\right) \quad (4.9)$$

where E_0 is the energy difference between the zero point levels of the transition state and the reactant.

In the so called "falloff" range between the high- and the low- pressure limits the competition between collisional stabilization and reaction processes determine the overall rate constant.

The rate constant can be represent in reduced falloff curves, which allow extrapolation of the rate constant in the falloff range if sufficient information on the limiting ranges is available. For the Lindemann mechanism, the reduced falloff

curve is given by the following expression [35]:

$$\frac{k_{uni}}{k_{\infty}} = \frac{k_0/k_{\infty}}{1 + k_0/k_{\infty}} \quad (4.10)$$

in this k_0 has units s^{-1} , i.e. this is multiplied by the pressure (concentration). The energy dependence of the rate of the reaction step introduces a broadening of the falloff curves. Based on comparisons with experimental data, Troe [36] extracted an empirical factor ($F_{c,sc}(k_0/k_{\infty})$), which accounts for this effect. The reduced falloff curves are corrected with this so called strong collision broadening factor $F_{c,sc}(k_0/k_{\infty})$ (see also Ref. [35]):

$$\frac{k_{uni}}{k_{\infty}} = \frac{k_0/k_{\infty}}{1 + k_0/k_{\infty}} F_{c,sc} \left(1 + \left(\frac{\log(k_0/k_{\infty})}{0.75 - 1.27 F_{c,sc}} \right)^2 \right)^{-1} \quad (4.11)$$

In the RRKM model the weak collision effects are accounted for by the collision efficiency parameter β , which do not change the broadening of the falloff curve. One of the weak points of the model is that the additional broadening caused from these is not accounted for.

The RRKM model is a great success for the reaction rate theories. This could represent the experimentally observed rate constant for unimolecular reactions with tight transition state. The model fails for reactions where rotational excitation and weak collision effects play a significant role.

4.2.2 Troe Formalism

A different approach has been developed by Troe [25, 37, 38]. The starting point of the model is to calculate the *low pressure rate constant* (see Eq. 4.7) in the *strong collision limit*, so that the population can be approximated by the Boltzmann distribution function [22, 25]. The density of states corresponds that at the dissociation threshold, since almost all molecules which reach this barrier react further. The reaction species are approximated as non-rotating harmonic oscillators. These assumptions are substituted in Eq. 4.7 and the obtained rate constant

is multiplied with a number of correction factors to allow for these:

$$k_0^{sc}(T) = \beta Z[M] \frac{\rho_{v,h}(E_0) k_B T}{Q_{vib}} \exp\left(-\frac{E_0}{k_B T}\right) F_{anh} F_E F_{rot} F_{rotint} F_{corr} \quad (4.12)$$

where $\rho_{v,h}(E_0)$ is the harmonic density of states at the dissociation threshold. Approximating a molecule as a harmonic oscillator introduces uncertainty, e. g. its vibrational levels are not equally spaced but get closer together with increasing energy. This effect is corrected by F_{anh} . F_E accounts for the dependence of the density of states on the internal energy of the molecule, F_{rot} for the rotational contributions to $\rho(E_0)$ and F_{rotint} accounts for possible internal rotations. F_{corr} is introduced for the assumption that there is no coupling between the other correction factors. For more details see Ref. [25].

The *high-pressure rate constant* is calculated with the standard transition state expression (Eq. 4.9).

In order to extrapolate the rate constant in the *falloff range*, one needs information on the broadening effects. The strong collision broadening factor ($F_{c,sc}$) has been already discussed in the previous section. Troe recognized that the weak collision effects broaden additionally the falloff curves and introduced the weak collision broadening factor $F_{c,wc}(k_0/k_\infty)$ [39]. This is related to the collision efficiency β , which is extracted from comparison of the calculated strong collision low pressure rate constant with experimental results ($\beta = k_0^{exp}/k_0^{sc}$). The efficiency of the energy transfer processes, which are rate determining in the low pressure range, depend strongly on the properties of the bath gas. Inefficient collision partners are gases which have in general only translational degrees of freedom (e. g. He, Ar), since they are not able to accumulate a large amount of energy. For these $\beta = 0.1 - 0.2$, while for effective partners (e.g. CF_4), the strong collision limit can be reached ($\beta = 1$).

The dependence of the weak collision broadening factor on k_0/k_∞ is found to be similar to the one of $F_{c,sc}(k_0/k_\infty)$ and its magnitude is related to the collision efficiency with the following expression [35]:

$$F_{c,wc} \approx \beta^{0.14} \quad (4.13)$$

The total broadening factor is $F_c = F_{c,sc} \times F_{c,wc}$, and the falloff behavior of the thermal rate constant can be represented by Eq. 4.14:

$$\frac{k_{uni}}{k_\infty} = \frac{k_0/k_\infty}{1 + k_0/k_\infty} F_c \left(1 + \left(\frac{\log(k_0/k_\infty)}{0.75 - 1.27F_c} \right)^2 \right)^{-1} \quad (4.14)$$

The model developed by Troe is a powerful tool for analyzing experimental data if sufficient information of the temperature dependence of the rate constant in the two limiting cases (high- and low- pressure ranges) is available. Furthermore, parametrization of the results from complicated rate theories (e. g. Master Equation) with Eq. 4.14 yields simple analytical expressions for the falloff behavior of the rate constant, which can be directly used for combustion and atmospheric modeling.

4.2.3 Master Equation Analysis

More detailed information on the weak collision effects can be obtained if one examines the energy transfer processes between the individual energy levels (as shown with solid vertical arrows in Fig. 4.1).

Considering the microscopic dynamics in the Lindemann - Hinshelwood mechanism, one obtains a system of coupled differential equations (Eq. 4.15), called Master Equation (ME):

$$\frac{dN(E_i)}{dt} = Z[M] \sum_j [P(E_{ij})N(E_j) - P(E_{ji})N(E_i)] - k_2(E_i)N(E_i) \quad (4.15)$$

where $i = 0, \dots, n$ and $j = 0, \dots, n$, and n is the number of differential equations, which should be solved in order to determine the population of the individual energy levels. $N(E_i)$ is the population of level E_i , $P(E_{ij})$ the probability collision induced redistribution of energy between levels i and j and $k_2(E_i)$ is the specific rate constants. The first two terms in Eq. 4.15 describe the population redistribution induced by collision. The third one represents the population lost by reaction.

Eq. 4.15 is the one dimensional ME. The system of differential equations (Eq. 4.15) can be solved also for a given energy as a function of the angular momen-

tum (two dimensional ME, e.g. [40]).

In order to solve Eq. 4.15 one separates the energy range above the threshold in equal intervals (grains) [1, 41]. The energy of the states in a particular interval is assumed to be the same. The Master equation describes the probability for a molecule to be in a particular grain.

The rate of the *reaction step* is approximated with some of the models described above (see Sec. 4.1 and Ref. [26]).

The *probability for energy transfer* between the energy grains is approximated by model functions [26]. A relative simple approximation for this is the exponential down model, given by the following expression:

$$P(E_i, E_j) \propto \exp \left[- \left(\frac{E_j - E_i}{\alpha} \right) \right] \quad (E_i < E_j) \quad (4.16)$$

where α determines the average downward energy transferred per collision ($\alpha \cong \Delta \langle E_{down} \rangle$). The respective upwards transferred energy is determined by the principle of microscopic reversibility. For more details on this and other models used for estimation of the probability for energy transfer processes see Ref. [26]. This is the most uncertain part in this approach and in general comparison with experimental data is needed for the analysis.

Different program packages for solving Eq. 4.15 are available (e.g. [42]).

The ME analysis is the most detailed statistical approach with respect to the approximation used for the energy transfer processes. Even for this model comparison with experimental data is needed in order to extract the collision efficiency and validate the model for the energy transfer probability.

Based on comparison between the results obtained from the Master Equation and the ones received from analysis with the Troe formalism, Troe [38] extracted the following connection between the collision efficiency and the mean energy transferred per collision $\langle \Delta E \rangle$:

$$\frac{\beta}{1 - \beta^{1/2}} = - \frac{\langle \Delta E \rangle}{F_E(T) k_B T} \quad (4.17)$$

F_E accounts for the change in the density of states with energy (see Sec. 4.2.2).

4.2.4 Complex Forming Bimolecular Reactions

Investigations on the kinetics of complex forming reactions (CFR) is a challenging task. The complexity of this class of reactions results from the competition between different reaction channels, which occur on similar time scales. In general, information on the rate constant of CFR can be obtained with detailed models like the Master Equation analysis if an accurate potential energy surface and information on the energy transfer processes is available.

This section presents a simplified model, which can be applied if information on the rate constant in broad temperature and pressure ranges exists or for parametrization of the results obtained by detailed statistical rate calculations.

A schematic representation of the mechanism of a complex forming reaction is presented in Fig. 4.2. The fate of the complex (AB), formed by the so called chemical activation, is determined by its lifetime [8], for which the heights of the entrance (to complex) and the exit (to products) barriers are of crucial importance. Its further kinetics can be investigated with theories for reactions with several channels (see Fig. 4.2).

For the discussions in this section, it is assumed that the stabilized part of the population does not contribute to the reaction processes and that the back reaction of the products negligible. Hence these are shown in Fig. 4.2 with gray arrows. Both of these channels can open at particular external conditions, but this is not a subject of the discussions in this chapter.

The gray regions in Fig. 4.2 represent the population distribution of the complex in the two limiting cases - high- and low- pressure ranges (shown respectively with dashed and dotted gray lines). The pressure dependence of the rate coefficients for stabilization / direct reaction processes (respectively $k_f([M])$ and $k_D([M])$), and the sum of these is presented in Fig. 4.3.

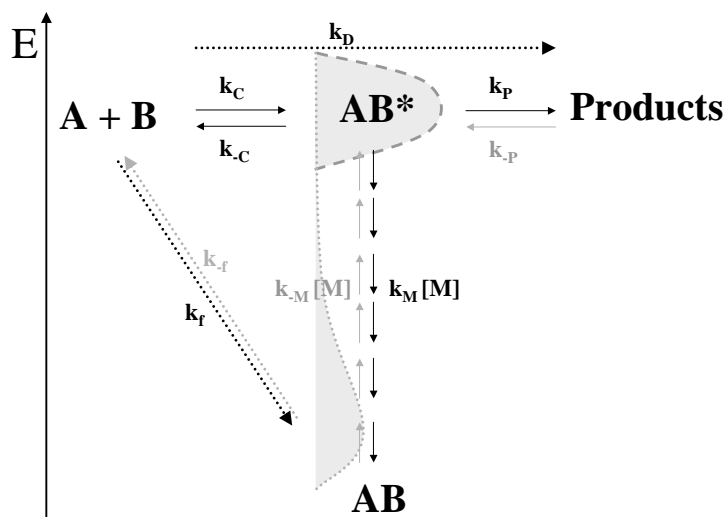


Figure 4.2: Reaction mechanism for complex-forming reactions. The gray regions represent the population in the two limiting pressure ranges. The dotted lines represent schematically the addition and direct reaction pathways.

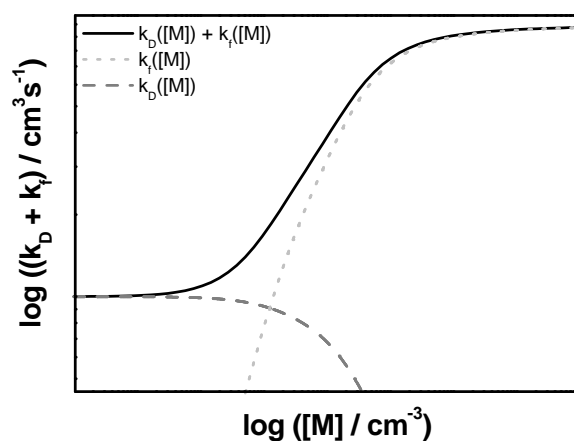


Figure 4.3: The pressure dependence of complex-forming reactions, determined from the pressure dependent addition and the pressure independent reaction to products.

At *low pressures* the reaction processes dominate the collisional stabilization. Solving the rate equations for the Lindemann - Hinshelwood model with the mechanism presented in Fig. 4.2 and steady state approximation for $[AB^*]$, one obtains the following expression for the rate constant for product formation [19, 21, 18]:

$$k_D([M]) = \frac{k_C k_P}{k_{-C} + k_P + k_M [M]}, \quad k_D^0 = \frac{k_C k_P}{k_{-C} + k_P}, \quad k_D^\infty = \frac{k_C k_P}{k_M [M]} = 0 \quad (4.18)$$

$k_D([M])$, presented with dashed line in Fig. 4.3 decreases with pressure, since the concentration of the complex $[AB^*]$ is depleted by collisional stabilization. k_D^0 determines the low pressure range of the overall rate constant.

The stabilization rate $k_f([M])$ is directly related to the pressure, so at *high pressures* the reaction leads to the formation of the stabilized complex AB:

$$k_f([M]) = \frac{k_C k_M [M]}{k_{-C} + k_P + k_M [M]}, \quad k_f^0 = \frac{k_C k_M [M]}{k_{-C} + k_P}, \quad k_f^\infty = k_C \quad (4.19)$$

The falloff behavior of $k_f([M])$ is as the one of simple recombination reactions. In the high-pressure limit a thermal distribution of AB is reached, as shown in Fig. 4.2 with dashed gray line. The overall rate constant in this range is pressure independent and is determined from the rate constant for the complex formation k_C .

In order to describe the population between these two cases, one applies steady state approximation for the concentration of the intermediate (AB^*) , governed by the rates of the processes described above [43].

As seen from Fig. 4.3 in complex forming reactions S - shaped falloff curves are observed. The pressure dependence of the overall rate constant, which is the sum of $k_f([M])$ and $k_D([M])$ can be presented by the following expression [20, 44]:

$$k = k_D^0 \left[1 - \frac{y}{1+y} F_c^{(1+\{\log y\}^2)^{-1}} \right] + k_f^0 \left[\frac{1+z}{1+y} F_c^{(1+\{\log y\}^2)^{-1}} \right] \quad (4.20)$$

$$k_f^0 = \frac{k_C k_M [M]}{k_{-C}}, \quad y = \frac{k_f^0}{k_f^\infty - k_D^0}, \quad z = \frac{k_D^0}{k_f^\infty - k_D^0}$$

In this expression it is assumed that the broadening of the falloff curves (F_c) is equal for the two transition regions ($k_f^\infty \rightarrow k_f^0$, $k_f^0 \rightarrow k_D$).

The properties of the complex AB^* , the reaction channel barriers and the energy transfer processes determine the temperature and pressure dependence of the overall rate constant [20, 21].

The analysis presented in this section allows for a simple extrapolation of the falloff curves if experimental data in broad p - and T - ranges are available. Furthermore, this allows for a parametrization of the results from more complicated theoretical models and yields simple expressions, which can be directly used for modeling.

4.2.5 Non - Statistical Models

Statistical models require high density of states of the reactants above the reaction barrier. In the last years discussions on non - statistical microscopic kinetics of some reaction species is a subject of discussions (see [1]). State resolved experiments as well as quantum mechanical calculations for some reaction species with low density of states (e. g. HCO, DCO, HO₂, HNO etc., for summary see Ref. [1]) reveal significant fluctuations of their specific rate constants. The slow IVR caused by the large distance between their vibrational states contradicts the ergodic assumption, which allows for the statistical approximations of $k(E)$. Whether these affect the thermal rate constant can be proved by using the exact quantum mechanical calculations on $k(E)$ instead of the statistical approximations presented above. There are a few non - statistical models presented in the literature (see e.g. Ref. [45, 29]), which use the average value of the specific rate constants calculated quantum mechanically. These predict deviations of the thermal rate constant from statistical predictions, but these are not experimentally confirmed so far.

Another possibility is to implement directly the quantum mechanical values of $k(E)$ in the calculations. This can be done by exchanging the integral in the RRKM model for the thermal rate constant (Eq. 4.6) with a discrete summation over nu-

merical results on $k(E)$, as shown in Eq. 4.21:

$$k(T, [M]) = \frac{\beta Z[M]}{Q_{vib}} \sum_i \frac{k(E_i) \exp(-\frac{E_i}{k_B T})}{k(E_i) + \beta Z[M]} \quad (4.21)$$

Further improvement of the model would be to consider the state specific nature of the activation / deactivation processes, but this is a subject which is quite poorly understood till now. In order to make some estimations on these, one should consider the energy transferred per collision depending on the mode which is activated / deactivated. More details on the model are given later in this work.

Chapter 5

The Decomposition of Formyl Radicals

5.1 Introduction

The formyl radical (HCO) is an important intermediate in combustion processes, e. g. in the oxidation of methane:



Similar processes occur in the oxidation of higher hydrocarbons.

Due to the low C-H bond energy ($\approx 6000 \text{ cm}^{-1}$) the thermal decomposition competes with bimolecular reactions even under low temperature combustion conditions (up to 1000 K).



The decomposition (R 5.1) is a chain propagating step, while the recombination reactions (R 5.2) lead to chain termination. Hence the fate of the formyl radical is crucial for ignition and combustion processes. A detailed knowledge of its kinetics of the thermal decomposition is needed for accurate combustion modeling.

Another aspect which makes the reaction interesting is its so called non-statistical

behavior. The base of statistical rate theories is the ergodicity assumption (see Ch. 4). The hypothesis of fast internal vibrational energy redistribution (IVR) allows for the rate of reaction step to be calculated assuming that the energy levels of the reactant(s) are statistically populated.

The fast IVR demands a sufficient density of states ($\rho(E)$). In general, at energies as high as the dissociation threshold, there are a lot of states per energy interval (e. g. for the HNO_3 decomposition $\rho(E_0) > 100 \text{ cm}^{-1}$). The energy levels of HCO, calculated quantum mechanically in Ref. [2] are illustrated in Fig. 5.1.

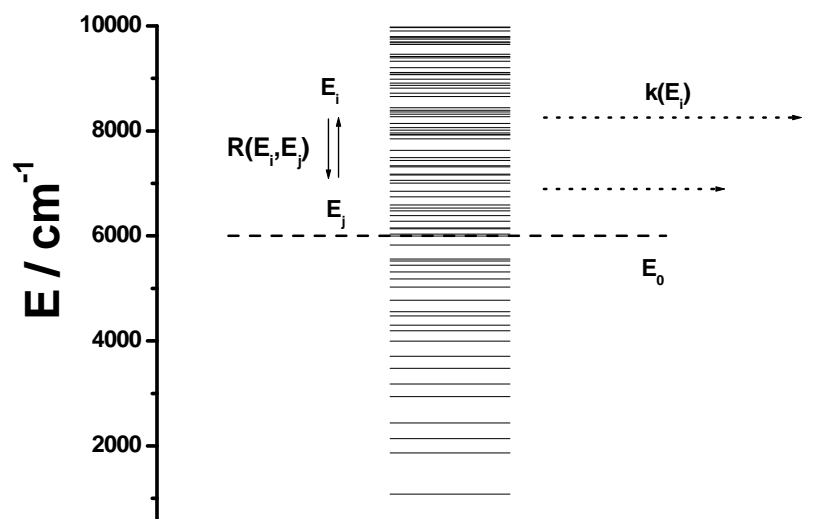


Figure 5.1: Energy level diagram of HCO. The positions of the energy levels were calculated quantum mechanically [2]. E_0 is the dissociation threshold, $k(E_i)$ - the specific rate constant for level E_i , and $R(E_i, E_j)$ - the rate of energy transfer processes between the levels E_i and E_j .

As one can see from Fig. 5.1, the spacing between the energy states is significant even at energies above the threshold, which is the range important for the kinetics of the radical. The reason for this anomalous low density of states ($\rho(E_0) \ll 0.01 \text{ cm}^{-1}$) is the structure of the radical. HCO has only three vibrational degrees

of freedom and a low dissociation barrier ($E_0 \approx 6000 \text{ cm}^{-1}$). Furthermore, its frequencies, which are related to the reduced mass of the vibrating fragments, are large due to the light H atom involved in two of the three vibrational modes. This causes isolated quasi-bounded vibrational states, or so called resonances, which are characterized with a energy width (Γ), defined as its full width at half maximum. These states are termed as isolated if their widths are small compared to the spacing between them ($\Gamma \ll 1/\rho(E)$ [1]). The decomposition rate constant of each resonance is related to its width ($k(E_i) = \Gamma_i/\hbar$). The large spacing and weak coupling between the energy levels in HCO restricts the IVR between these. Hence, oppositely to statistical predictions, the microscopic decomposition rates of neighboring resonances vary by orders of magnitude [2,46,47,48,49,50,51,52], depending on the modes which are excited in a particular state (Fig. 5.2).

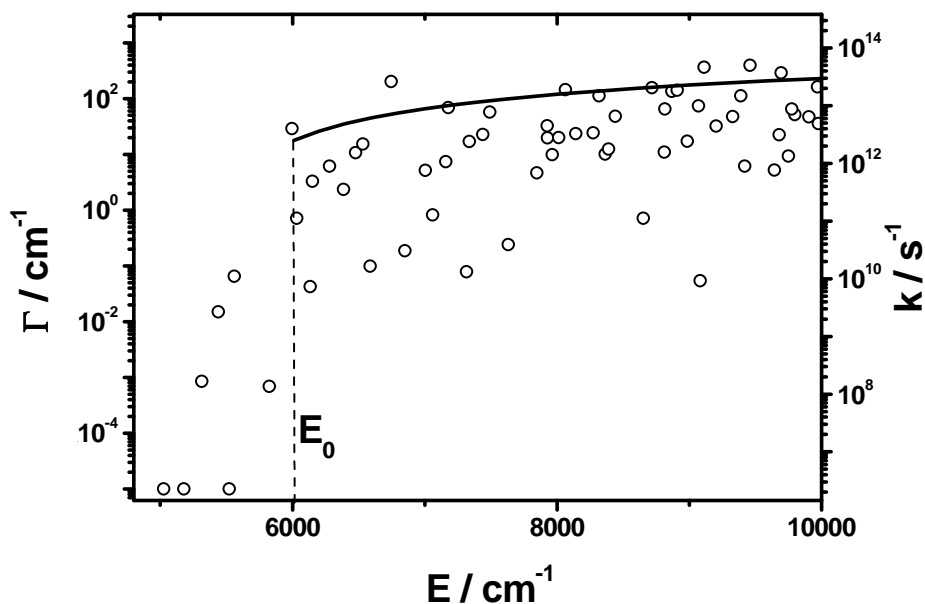


Figure 5.2: State specific rate constants of HCO. Open circles - QM calculations from Schinke and co. [2], solid line - Whitten-Rabinovitch Approximation, dashed line - dissociation threshold.

The investigations show, that states in which the dissociation coordinate (the CH

stretch) is excited decompose fast, while excitation in the CO vibration results in a long resonance lifetime, since a sufficient time is needed to redistribute the energy into the dissociation mode. In other words the dissociation dynamics of HCO is strictly mode specific, or regular.

Investigations of the isotope effects by the decomposition of DCO have been performed as well:



Substituting the hydrogen atom in HCO with deuterium, which is twice as heavy, leads to significant decrease of the vibrational frequencies, and subsequently higher density of states. The dynamics of this radical is found to be different from the mode specific (regular) behavior of HCO [53]. This is a result of coupling effects, which will be discussed later in this work. Due to these the microscopic dynamics of DCO, on the contrary to this in HCO, is not mode specific [54, 53]. Although the resonance states in DCO are not assignable with regard to the modes which are excited, strong fluctuations of their lifetimes are observed as well.

The studies on the HCO / DCO radical till now were focused on examining its state specific dynamics [2, 47, 48, 54, 49, 50, 51, 52, 55]. Experiments determining the resonance positions and widths have been performed mainly with high resolution Stimulated Emission Pumping (SEP) spectroscopy [49, 50, 51, 52, 54, 55, 56]. The main idea of this technique will be shortly discussed. HCO radicals are produced by the photolysis of a proper precursor (e.g. CH_3CHO) and subsequently cooled so that almost all of them are rotationally and vibrationally cold. They are then promoted to a specific energy level with a pump laser, and simulated emission is initiated by a shifted (dump) laser. One monitors the changes in the fluorescence intensity as a function of the wavelength of the dump laser. From the spectrum one can extract information for the resonance positions and widths. In some studies Dispersed Fluorescence [52] was employed as well.

The experimental studies proved the existence of metastable resonances in HCO up to energies of more than 20000 cm^{-1} , which correspond to 12 excitation quanta in the CO stretching mode [52]. Similar observations are reported for the DCO

radical as well. The experimental results have been confirmed by quantum mechanical calculations [2,46,47,48,54], based on an accurate potential energy surface [46,57,58]. Strong fluctuations of the resonance lifetimes, depending on the modes which are excited are reported (see Fig. 5.2).

As opposed to the extensive studies of the state specific dynamics of HCO, there are only a few direct measurements of the thermal rate constant $k(T,p)$ [3,4,5,59]. Timonen et al. [3] performed experiments on this at pressures between 3 and 8 mbar and temperatures ranging from 637 K to 832 K. Mixtures of CH₃CHO (CD₃CDO) and different collision partners (He, N₂, Ar) were photolysed to generate the formyl radicals (HCO / DCO), which were subsequently detected by photoionization mass spectrometry. The experimental data were represented well by an "isolated resonance model", developed by Wagner and Bowman [6].

Friedrichs et al. [4] performed experiments behind incident and reflected shock waves ($p = 0.28 - 1.90$ bar, $T = 835 - 1230$ K). Frequency Modulation spectroscopy was used to detect the HCO, generated by photodissociation of CH₂O / Ar mixtures. The experimental data were compared to a Master Equation analysis, but the narrow pressure range did not allow for a rigorous test of the model.

Krasnoperov et al. [5,59] examined the decomposition rate constant at pressures 0.8 - 100 bar ($T = 498 - 769$ K). The HCO were produced by photolysis of CH₃CHO / He mixtures. As detection techniques were employed Cavity Ring Down Spectroscopy (CRDS), single- and multi- pass absorption spectroscopy.

In the data interpretation in Refs. [3,4,5] was assumed that the rate constants is in the low pressure limit, i. e. the experimentally obtained first order rate coefficients are divided by the bath gas concentration. The results reported by Timonen et al. [3] are a factor of 3.5 to 2.2 (respectively at 498 and 769 K) higher than these by Refs. [4,5]. Possible falloff effects, which would cause deviations from the adopted linear pressure dependence of $k(T,[M])$, are not discussed. The non-Arrhenius behavior of the rate constant above 10 bar observed in [5] were attributed to the non-statistical behavior of the radical, discussed in Ref. [6].

Wagner and Bowman [6] presented the first theoretical model, which tries to associate the non statistical behavior of HCO to its thermal rate constant. In this the integral in the standard RRKM expression is exchanged with a summation over

isolated resonance states. Their decomposition rates are assumed to be the same, since there was no information on the exact resonance lifetimes at this time. Decomposition of the molecule was considered only at vibrational energy where a resonance exists.

The model was compared to the experimental data available till then [3, 60, 61]. The only direct high temperature study was the one from Timonen et al. [3], where the thermal decomposition of HCO was investigated in a limited pressure range, as discussed above. Refs. [60, 61] presented investigations on the recombination of H and CO at lower temperatures, and in order to interpret the results correctly, one should consider the temperature dependence of the collision efficiency.

The theoretical model predicted, that the tunneling states have strong influence on the thermal rate constant due to their significant populations [6, 7, 62, 63]. These would cause deviation from the low pressure limit at extremely low pressures, which was not confirmed from the experimental data [3, 60, 61]. Hence the authors in Ref. [6] concluded that the tunneling states are not dynamically accessible and postulated deviations from the linear range at pressures above 10 bar, and lower high-pressure rate constant compared to the standard RRKM model.

In a later work Wagner and co. [7] reexamined the conclusions of Ref. [6]. Deviations of the rate constant from the linear regime are predicted at much lower pressures (> 1 mbar). In [7] a new model was also presented, in which, in a similar approach, the exact lifetimes of some of the resonances are implied. The work is mainly concentrated on the contribution of individual resonances to the thermal rate constant. In order to calculate the overall decomposition rate one must include all the resonance states important for the kinetics. The reason for the discrepancies between the two theoretical studies [6, 7] is the treatment of the tunneling effects. Some further discussions on the problem are made in Ref. [62, 63].

Investigations of the influence of non - statistical effects on the thermal decomposition of HOCl were performed by Hase et al. [29, 64]. The authors use RRKM based approach, in which they implement the average value of the quantum mechanically calculated [65] specific rate constants and compare this to a standard SACM model. Differences between the approximations for $k(E)$ are found only at higher energies, and thus deviations in the falloff- and the high- pressure- ranges compared to the statistical model are reported, while the low pressure rate con-

stant is stated to be the same.

Another example for a radical with strong fluctuations of the specific decomposition rate constant is HO₂ [66]. Adversely to the HCO and HOCl the fluctuations of $k(E)$ of HO₂ are statistically distributed and unassignable. In other words these are not mode specific and have been described with a statistical distribution model. In [45] the averaged specific rate constants from this model are implemented in an RRKM based approach and used to calculate the decomposition rate constant. Compared to the applied statistical model, deviations are reported in the low pressure and the falloff ranges.

The theoretical investigations of HOCl and HO₂ can be used only as model studies, since no comparison with experiments is presented.

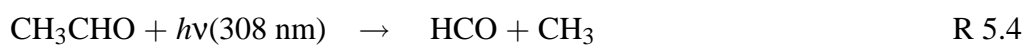
Statistical theories postulate that both the state specific, and the thermal rate coefficients, can be presented with proper average functions ([1, 26]). The literature data proves the strong influence of the low density of states of some radicals [1] on their state specific dynamics. A goal of this study is to prove if this affects their macroscopic decomposition as well.

The HCO and DCO are probably the most appropriate candidates for these studies. Their microscopic dynamics have been subject to numerous studies, and the extended experimental conditions covered in this work allow the testing of different levels of theory on their macroscopic decomposition rate. The investigations in this work would also allow to check if the mode specific microscopic behavior of HCO affects the thermal rate in a different manner compared to the not assignable dynamics of DCO.

5.2 Experimental Details

5.2.1 Generation and Detection of Formyl Radicals

Photodissociation of acetaldehyde was used to generate the formyl radicals:



where the major channel (95 %) is reaction R 5.4 [67].

The output of an excimer laser (Lambda Physik, Compex 102, XeCL), operated at 308 nm was used to generate the radicals. The beam was focused before the cell with a lens or a telescope, so the laser fluency was up to 60 mJ cm^{-2} .

An Optical Parametric Oscillator (OPO, Continuum Sunlite EX), pumped from an Nd:YAG-Laser (Continuum PL8010, 310mJ at 335 nm, pulselength 5-7 ns) was used for the excitation of the formyl radicals. The HCO (DCO) radicals were excited at about 258.5 (259) nm. The excitation wavelength was varied with the temperature.

The fluorescence signal was passed through a monochromator (Zeiss, M4 QIII) centered at 335 nm. The slit of the monochromator was set to 20 nm, which enabled the detection of different rotational and vibrational transitions. More details on the setup are given in the experimental part of this work.

5.2.2 Temperature Control

The significant temperature dependence of the rate constant of the title reaction demands an accurate determination of the temperature in the reaction zone. The difference between the readings of the two thermocouples, positioned in the cell volume, was kept below 5 K (10 K at the highest temperatures). This is an upper estimate for the uncertainty in the temperature determination and this could lead to max 15 % deviation of the rate constant.

The flow was set from 0.5 to 3 standard liters minute⁻¹, depending on the pressure and the temperature. It was verified that the reaction volume ($\approx 0.15 \text{ cm}^3$, determined by the profile of the photolysis laser beam in the cell) was completely scavenged by the flow before each laser shot. To ensure this, experiments were performed at various repetition rates of the lasers. No influence on the temporal concentration profiles was observed.

The relatively short fluorescence lifetime of HCO allowed measurements in N₂ despite its higher quenching rate. Due to the higher thermal conductivity of N₂, it was difficult to control the temperature in these experiments. Preheating the mixture before it enters the cell resulted in a decrease of the observed fluorescence intensity. No further efforts were made to overcome this problem, since it was

possible to keep the temperature gradient in the cell low by decreasing the flow. Thus the flow rates in N_2 as a collision partner were in general lower than these in He.

As bath gases were used He, Ar, N_2 (see Table 3.1). The precursors, acetaldehyde and d4 - acetaldehyde, were degassed several times and used without further purification.

5.3 Experimental Results

The temporal profiles of the relative HCO concentration showed single exponential decays (Fig. 5.3):

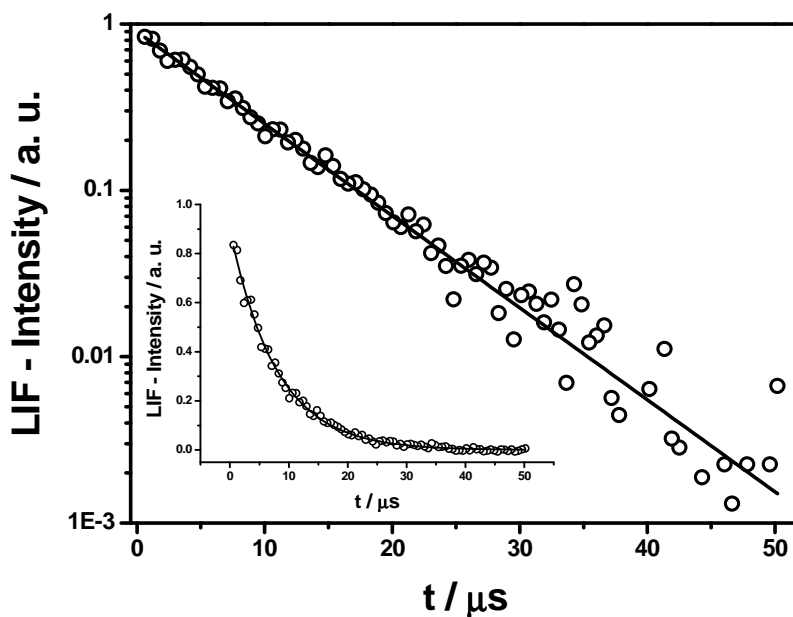


Figure 5.3: Typical time profile, $T = 590$ K, $p = 122.7$ bar. The fit with Eq. 5.1 yields a rate constant of $k = 1.2 \times 10^5 \text{ s}^{-1}$.

The signals were fitted with a nonlinear least-squares procedure to a monoexponential function:

$$I_t = I_0 \exp(-kt) \quad (5.1)$$

where k is the first order rate constant and I is the LIF intensity.

The photolysis of CH_3CHO yields CH_3 and CHO radicals. The unimolecular decomposition of HCO plays a dominant role for the observed $[\text{HCO}]$ decays under the experimental conditions in this work. Other possible reactions are radical-radical recombinations (second order), and reactions of the radicals with the precursor (pseudo first order). In order to get reliable data, the thermal decomposition was isolated from competing reactions, since a modeling of the observed decay would introduce additional uncertainties due to uncertainties of the rates of interfering reactions.

The rates of radical recombination reactions depend slightly on the temperature due to the low activation energy. The pressure dependence is also weaker compared to the unimolecular decomposition. On the contrary the unimolecular decomposition rate has a significant p - and T - dependence. It is proportional to the initial concentration of the radicals, compared to the quadratic dependence of the rate of bimolecular reactions on this. Thus the experiments were performed with low initial radical concentrations and at high temperatures and pressures in order to isolate the HCO decomposition. The influence of interfering reactions was checked by variation of the laser energy (radical-radical reactions) and the precursor concentrations (radical-precursor reactions). These were found to be significant under the experimental conditions in this work if the decomposition rate was less than 10^4 s^{-1} . Hence in this experiments the radical concentrations were kept low. Additionally, an accurate modeling was performed to examine the conditions by which the loss reactions have no influence on the observed signal. This determined the low temperature limit of 590 K. At temperatures higher than 800 K, the reaction was too fast to be resolved on the experimental time scale and the temperature was difficult to control. The pressure was varied between 1 and 170 bar.

Different initial HCO concentrations were obtained by variation of the photolysis laser energy, which was measured behind the cell. The absorption cross section of acetaldehyde (308 nm) of $3 \times 10^{-20} \text{ cm}^2$ [68] and the quantum yield of 0.95 [67] were adopted for estimation of the radicals concentrations. Extensive tests have been done at 700 K and $p \approx 10$ bar, where the radicals concentration was varied in the range $(3 - 40) \times 10^{12} \text{ cm}^{-3}$ and the precursor concentration $(2 -$

$20) \times 10^{15} \text{ cm}^{-3}$. The results are shown in Fig.5.4.

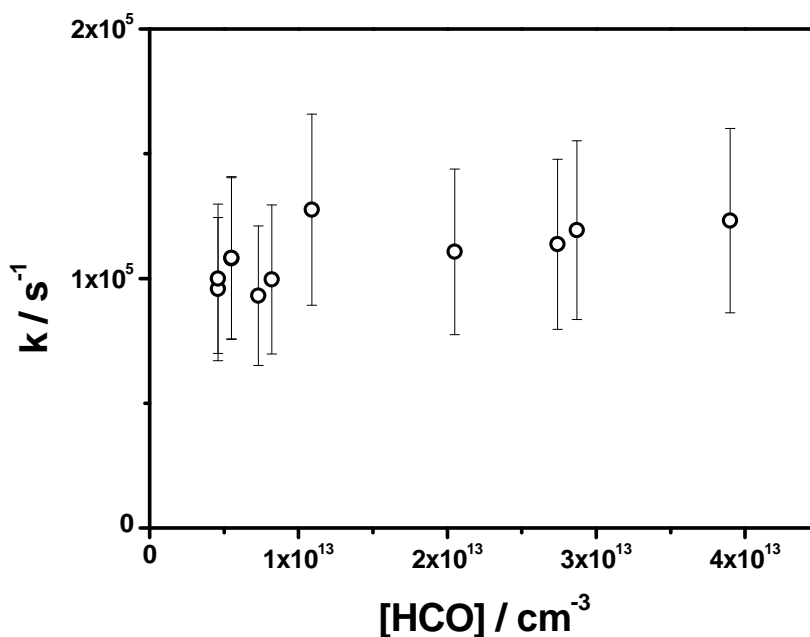


Figure 5.4: Experimental results of the thermal decomposition of HCO at 700 K at various precursor and radical concentrations.

No influence of this on the rate constants were observed beyond the experimental uncertainty. At these experimental conditions the rate constant was in the order of $1 \times 10^5 \text{ s}^{-1}$. At lower temperatures and pressures, the radical concentrations were kept low. No dependence of the initial precursor concentrations was observed, which indicates that under these experimental conditions, secondary reactions with the precursor are unimportant. These observations have also been proved with a modeling of the concentration / time decays of HCO (see Ref. [69]). The experimental results, as well as the radical and precursor concentrations are listed in Table 5.1. The concentrations of the HCO and CH_3 radicals are the same, so only values for [HCO] are given.

Table 5.1: Experimental results at 700K. No significant deviations of the experimentally determined rate constant is observed in spite of the strong varied radical and precursor concentrations. See text for further discussions.

$E/$ mJ/cm^{-2}	$p(\text{He})/$ bar	$[\text{CH}_3\text{CHO}]/10^{15}$ cm^{-3}	$[\text{HCO}]/10^{12}$ cm^{-3}	$k/10^4$ s^{-1}	Exp.
10.0	8.9	16.5	7.3	9.3	1
7.5	9.0	16.5	5.5	10.8	1
35.0	9.8	18.6	28.7	11.9	3
12.5	10.1	8.3	4.6	9.6	3
22.5	10.4	8.3	8.2	10.0	3
45.0	10.6	19.6	39.0	12.3	3
30.0	10.8	8.3	10.9	12.8	3
50.0	11.2	2.1	4.6	10.0	3
30.0	11.2	20.7	27.4	11.4	3
60.0	11.4	2.1	5.5	10.8	3
50.0	12.1	9.2	20.5	11.0	3

5.4 Discussion

The thermal decomposition of formyl radicals has been investigated in broad temperature and pressure ranges. The mixtures were prepared in He, Ar or N_2 in order to examine the dependence of the collision efficiency on the type of the bath gas. Strong fluctuations of the specific rate constants of HCO and DCO are observed in state resolved experiments and numerical stimulations [2, 46, 47, 48, 49, 50, 51, 52, 54, 55]. The widths of neighboring resonances are found to differ by more than three orders of magnitude (see Fig. 5.2). The reason is the low density of states resulting in weak mode coupling and hence slow IVR. The competition between decomposition and IVR processes contradicts the ergodicity assumption (see Sec. 5.1), which is the base of the statistical theories.

It is well known that the specific rate constants of all reaction species fluctuate to some extent [1], though statistical (averaged) approximations of these prove to work well in most of the cases. The question is, where is the limit of statistical theories? Are there molecules in which the fluctuations of the specific decompo-

sition rates can not be approximated with statistical models or average functions without introducing uncertainty in the calculations on their macroscopic kinetics? This work presents experimental investigations on the thermal decomposition rate of formyl radical, comparison of the results with statistical models as well as with an isolated resonance model.

The experimental results at 752 K in Helium have been used to test the predictions of different levels of theory. These will be shortly discussed in the following sections.

5.4.1 Effects of the State Specific Rate Constant on $k(T,[M])$

5.4.1.1 Statistical Models

RRKM Model

For unimolecular reactions with tight transition states generally the RRKM model (see Sec. 4.2.1) allows a good representation of the pressure dependence of the rate constant.

The reaction step. Some details on the calculation of the specific rate constant with the RRKM model are given in the theoretical part of this work (see Sec. 4.1.1). This is calculated with Eq. 4.2, for which here the sum and density of states are approximated with the Whitten - Rabinovitch approximation [27]. Tunneling corrections are not included, but the tunnel effects are found to have no influence on the shape of the falloff curve in the range of the measurements in this work (see Ref. [70]). The influence of rotational excitation is not accounted for, in general this is found to have a minor influence on the shape of the falloff curves for reactions with tight transition states [26].

The thermal rate constant. The RRKM model is based on a number of assumptions, which are presented in detail in Sec. 4.2.1. The thermal rate constant is calculated with Eq. 4.6.

Weak collision effects. In the RRKM model, one calculates the strong collision rate constant and then multiplies it with a factor (β) to allow for the weak collision effects. The collision efficiency (β) is the only fit parameter in the model (see Eq. 4.6), it is extracted from comparison with the experimental data. Variations

of this parameter have no influence on the shape of the falloff curve, since the correction factor is the same for the whole pressure range.

The parameters used for the calculations are given in the appendix. In Fig. 5.5 experimental results from this work, Timonen et al. [3], Krasnoperov et al. [5] are compared with this model. Since there were no measurements reported at the same temperature, the expressions recommended in Refs. [3, 5] are used for comparison.

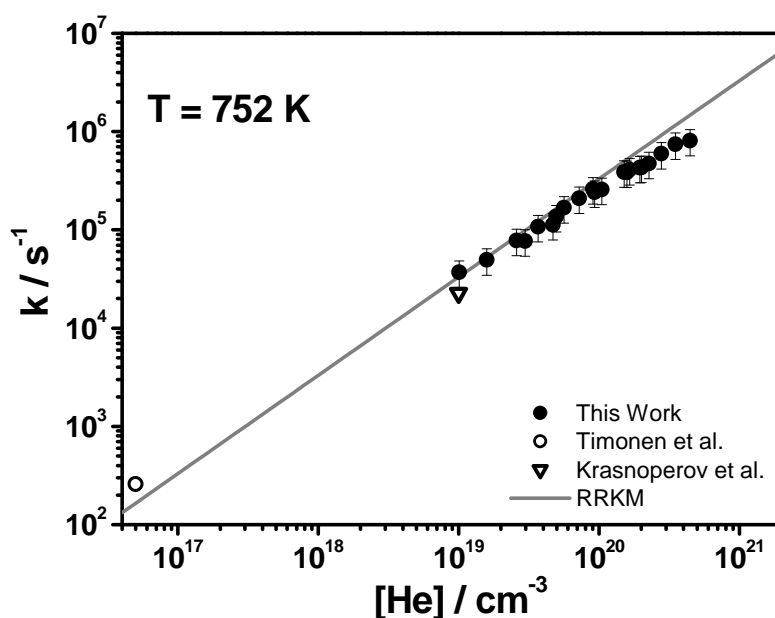


Figure 5.5: Comparison of experimental data at 752 K with theoretical models. RRKM.

The model predicts a linear pressure dependence of $k(T, [M])$ in the range of the measurements, and hence deviates from the experimental observations.

In order to check if the reason for the disagreement is the approximations made in this model (see Sec 4.2.1), particularly concerning the treatment of the weak collision effects, some more detailed approaches have been applied as well.

Troe Formalism

Troe [37, 38, 25] developed a different approach (see Sec. 4.2.2). In this model, the macroscopic coefficients in the limiting ranges are parametrized.

The low pressure rate constant. As stated in the theoretical part of this work (Sec. 4.2.1), in the low pressure limit the reaction rate is governed by the energy transfer processes (see Eq. 4.7).

In this model one first calculates the low pressure strong collision rate constant (Eq. 4.12), approximating the density of states with its value at the dissociation threshold (E_0). The anharmonic and rotational effects are considered with correction factors, and have no influence on the shape of the falloff curves. The value of the calculated strong collision low pressure rate constant $k_0^{sc}(752 \text{ K}) = 2 \times 10^{-13} \text{ cm}^3 \text{ s}^{-1}$.

High-pressure decomposition rate of $4.6 \times 10^8 \text{ s}^{-1}$ is calculated with the standard transition state expression (see Eq. 4.9).

In order to interpolate the falloff curve between this two ranges (high- and low-pressure limits) one needs information on the broadening factor (see Sec. 4.2.2).

Weak collision effects. In this model the weak collision effects are extracted by a comparison of $k_0^{sc}(T)$ with experimental data on this. For this the low pressure rate constant from Timonen et al. [3], extracted from measurements at pressures of a few mbar has been used, since the measurements in Refs. [4, 5] were performed at higher pressures. The collision efficiency $\beta_c = k_0^{\text{exp}}(T)/k_0^{sc}(T) = 0.03$ is used to determine the weak collision broadening factor ($F_c^{wc} = \beta^{0.14} = 0.6$). The strong collision broadening factors is calculated as described in Ref. [35], which yielded a value of 0.8 for F_c^{sc} . Hence the overall broadening factor if $F_c = F_c^{wc} \times F_c^{sc} = 0.5$. A falloff simulation with Eq. 4.14 and these parameters (k_0^{exp} , F_c , k_{inf}) is presented in Fig. 5.6.

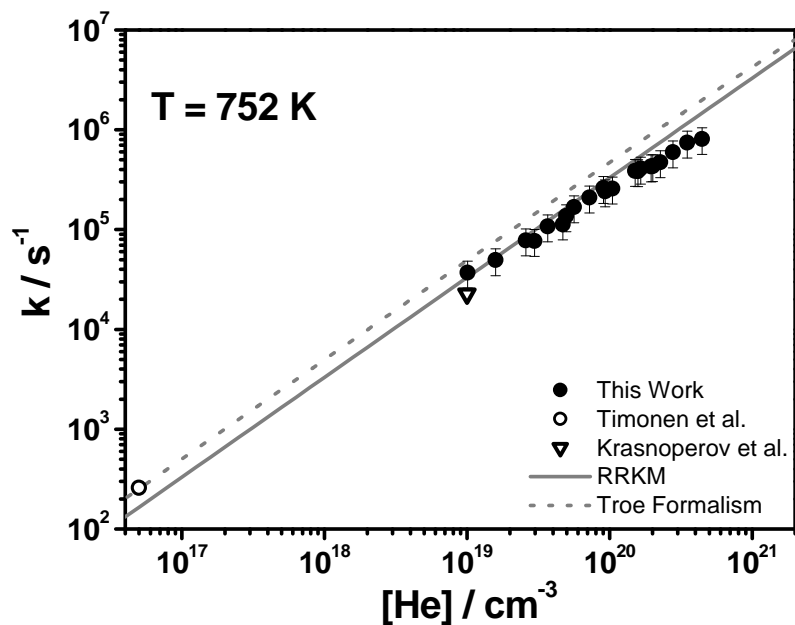


Figure 5.6: Comparison of experimental data at 752 K with theoretical models. Troe Formalism.

The falloff simulation, presented in Fig. 5.6 fits well to the measurement of Timonen et al. [3], since the experimental low pressure rate determined from this work has been used to extract the collision efficiency. However the pressure dependence of the decomposition rate is not correctly predicted.

Master Equation Analysis

The most detailed approach, concerning the treatment of the weak collision effects is the Master Equation analysis (see Sec. 4.2.3).

The reaction step. $k(E)$ is calculated as described in Section 4.1.1, where the sum and density of states are counted with the Beyer-Swineheart algorithm [26]. In this work the calculations are performed for $J = 0$, since, as stated in Secs. 4.1 and 4.1.1, this has a minor influence on the rate constant for reactions with tight transition states. The K rotor has been treated as an adiabatic degree of freedom (see sec 4.1.1), in [70] the same calculations are done for an active K rotor. No

significant differences in the results from the analysis are observed.

Weak collision effects. The probability for energy transfer processes (see Sec. 4.2.3) has been approximated with the exponential down model (see Eq. 4.16). Based on comparison with the experimental data, the energy transferred downward per collision is found to be $\alpha = 220 \text{ cm}^{-1}$.

More details on the theoretical background of the calculations are given in [26] as well as in the theoretical part of this work. For these the program package UNIMOL has been used [42]. The parameters for the calculation are given in the appendix.

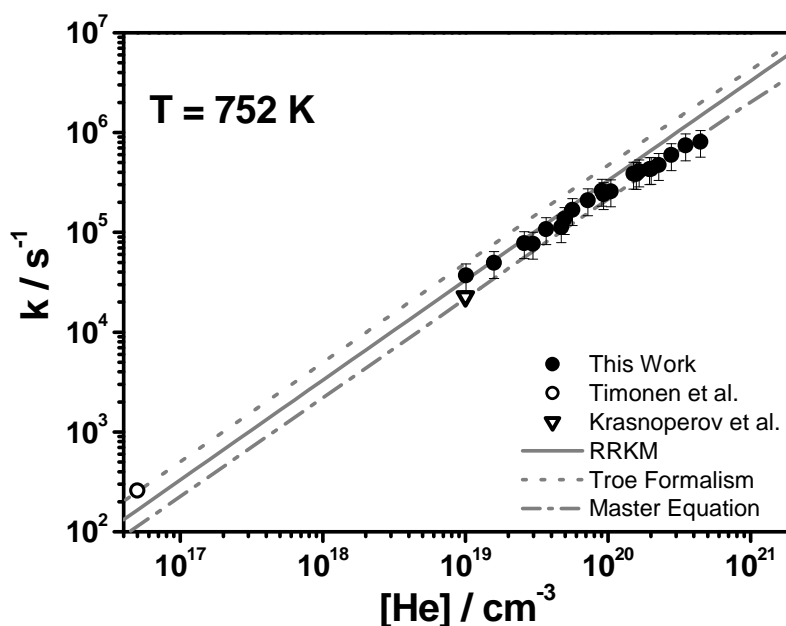


Figure 5.7: Comparison of experimental data at 752 K with theoretical models. Master Equation.

One can see (Fig. 5.7), that even with this approach, the shape of the calculated falloff curve is in poor agreement with the experimental data.

The applied statistical models predict linear dependence of the $k(T,[M])$ on pressure in the range of the measurements, which contradicts the experimental results.

5.4.1.2 Non - Statistical Model

The model applied in this work is shortly presented in Sec. 4.2.5. In this the integral in the RRKM expression is exchanged with summation over the resonance lifetimes calculated in Ref. [2]. As in the previous sections, first discussions on the rate of the reaction step will be presented. Finally, the thermal rate constant will be calculated and compared to the experimental results.

The reaction step.

Since this work focuses on the investigation of the decomposition rates of HCO and DCO, a comparison between the microscopic decomposition rates of the two radicals is presented in the following section. As stated above, the exchange of the H atom with D results in higher density of states in DCO. In Fig. 5.8 a comparison of the energy levels (from Ref. [2]) of HCO and DCO is presented.

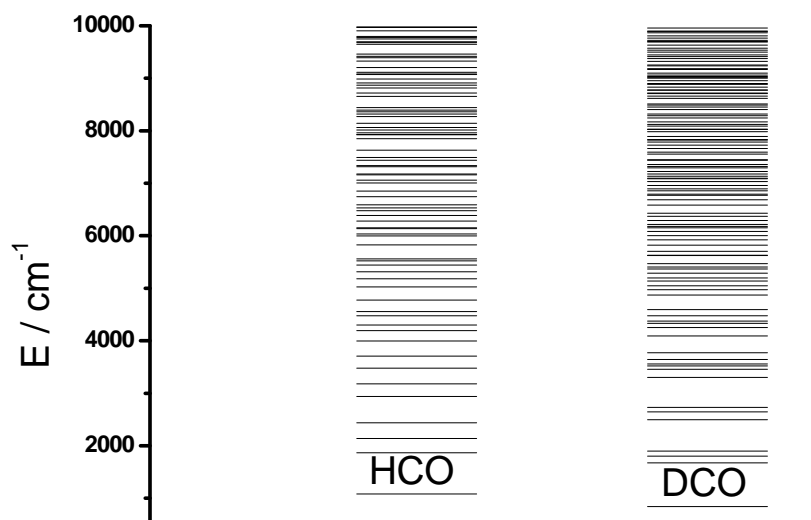


Figure 5.8: Comparison between the energy levels of DCO and HCO, based on the quantum mechanical calculations from Ref. [2]

Only the resonance states of the radicals which are significantly populated under the respective external conditions contribute to the macroscopic decomposition rate at these. For temperatures up to 1000 K and pressures to 1000 bar, these are the states up to 10000 cm^{-1} , so only these will be further discussed.

In order to check if the number of states characterized in the Ref. [2] is sufficient, in Fig. 5.9 a comparison of the sum of states of HCO between a harmonic count (Beyer-Swinehart algorithm [42]) and quantum mechanical calculation (Ref. [2]) is presented. One can see that the number of states calculated quantum mechanically exceeds the harmonic count. This is due to anharmonic effects, which are not accounted for in the Beyer-Swinehart algorithm [26]. The minor differences in the sum of states proves that the anharmonic effects in HCO are not significant. This analysis proves that the quantum mechanical calculations are sufficiently accurate concerning the number of the resonance states.

The next point of the discussion is the resonances lifetimes. As stated in the introduction of this chapter, the resonance states of the formyl radical are "isolated", in the sense that the resonance widths are in general small compared to the distance between them. Hence the coupling between these is weak and the fast energy transfer between these states is restrained. The decomposition rate of each state is determined by its width:

$$k(E_i) = \frac{\Gamma_i}{\hbar} \quad (5.2)$$

where Γ_i is the resonance width and \hbar the Planck constant.

Due to the weak mode coupling, the width of the resonance depends on the distribution of the energy quanta in different vibrational modes. If the energy is initially stored in the reaction coordinate (CH stretch), fast decomposition is observed. On the other hand, energy accumulation in the CO vibration results in a long resonance lifetime. In other words, HCO shows strictly mode specific behavior.

The resonance lifetimes are presented in Fig. 5.10.

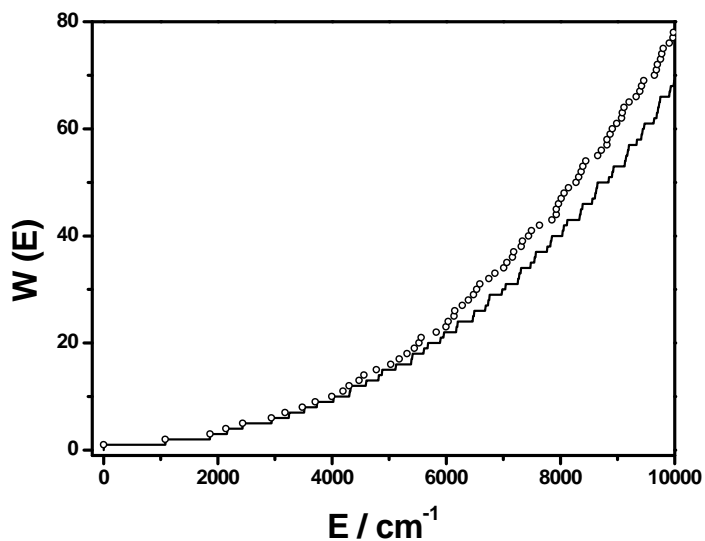


Figure 5.9: Sum of states of HCO. Solid line - harmonic count (Beyer-Swinehart algorithm), open circles - QM calculations from Schinke and co. [2]

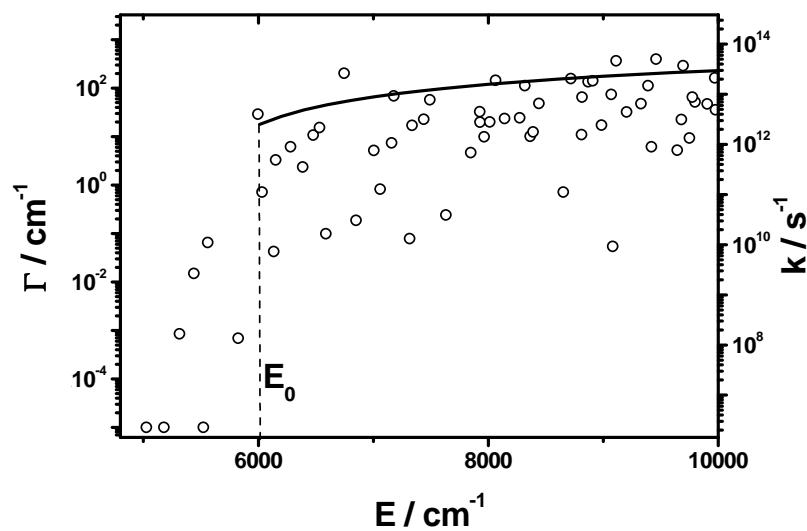


Figure 5.10: State specific rate constants of HCO. Solid line - Whitten-Rabinovitch Approximation, open circles - QM calculations from Schinke and co. [2].

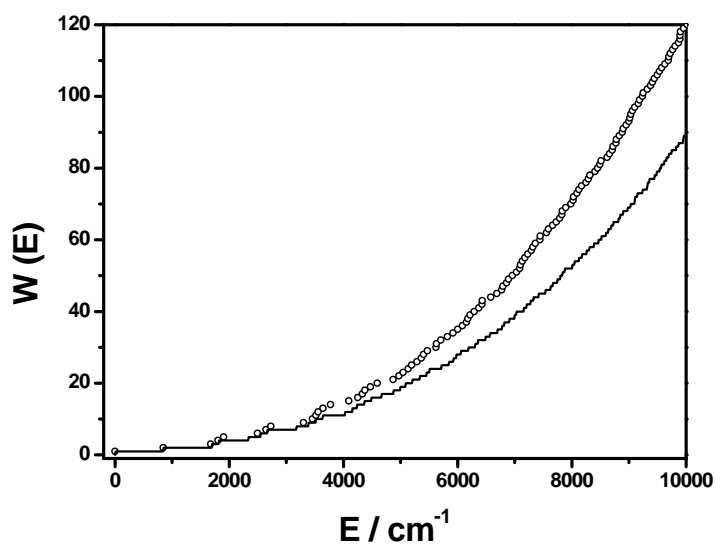


Figure 5.11: Sum of states of DCO. Solid line - harmonic count (Beyer-Swinehart algorithm), open circles - QM calculations from Schinke and co. [2].

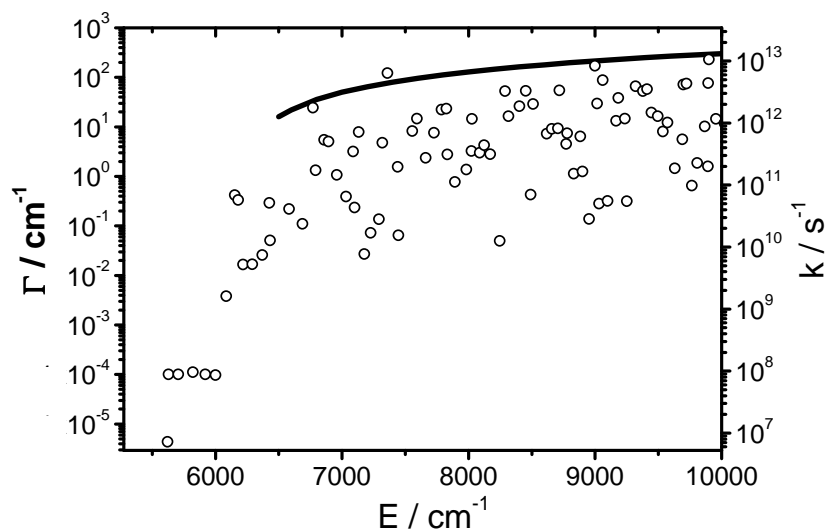


Figure 5.12: State specific rate constants of DCO. Solid line - Whitten-Rabinovitch Approximation, open circles - QM calculations from Schinke and co. [2].

Some complications in the characterization of the resonance states occur in the case of DCO. Basically, its higher density of states is associated with stronger anharmonic effects. As seen from Fig. 5.11, the deviations between the quantum mechanical calculations and the harmonic count in DCO are larger than these in HCO. Though the sum of states calculated quantum mechanically exceeds the harmonic count, an open question remains whether all resonance states important for the kinetics of the radical have been characterized.

The magnitude of the vibrational frequencies of the reaction species determines the position of their energy levels. The resonance between the frequencies of the DCO vibrations

$$\text{CD} : \text{CO} : \text{CDO} = 847 \text{ cm}^{-1} : 1795 \text{ cm}^{-1} : 1910 \text{ cm}^{-1} \text{ [55]} \approx 1 : 1 : 2$$

causes additional coupling between these (the so called Fermi resonance). So in general the mode coupling is weak, due to the relatively low density of states, but there are additional vibrational coupling effects, due to which the resonance states in DCO are not assignable (mode specific).

Comparison of the quantum mechanical calculations from Ref. [2] on the specific rate constant with statistical approximation is given in Fig. 5.12. In this case the average overestimation of the decomposition rate from the statistical model is higher than in HCO. One of the possible reasons is that not all of the resonance states have been characterized.

The microscopic decomposition rates of DCO show strong fluctuations despite its higher density of states. The fluctuations are not mode specific due to the coupling effects discussed above.

Higher density of states, stronger mixing between them, and, possible influence of rotational and anharmonic effects, which in general enables the energy transfer processes, poses the question if the unimolecular decomposition rate can be described with statistical theories.

The fluctuations of the resonance lifetimes in HCO and DCO are associated with the distribution of energy quanta in different vibrational modes and the weak coupling between them. The calculations of the specific rate constants used in this work (from Ref. [2]) are done for $J = 0$. Some calculations for $J > 0$ have been performed [71, 72, 73, 74], the number of states characterized in these is smaller and the rotational excitation considered is still lower than the mean J for the ex-

periments in this work. In most of the cases the resonance widths are weakly influenced by excitations of the rotational levels [71, 72, 73, 74].

As opposed to the strictly mode specific behavior of HCO, the resonance states in DCO are not assignable. A goal of this work is also to check if there are differences in the macroscopic behavior of the radicals.

The Thermal Rate Constant

As shown in the previous sections, the models using statistical averaging of the specific rate constants, are in poor agreement with the experimental data. An average function of the specific rate constants calculated quantum mechanically could improve the results to some extent (see e. g. Ref. [45, 29]), but the most realistic approach would be to introduce the "exactly" calculated specific rate constants. The simplest approach which allows this correction is a slightly modified RRKM model. Compared to the standard RRKM (Eq. 4.6), the integral is replaced with summation over the discrete decomposition rates:

$$k(T, [M]) = \frac{\beta \cdot Z \cdot [M]}{Q_{vib}} \cdot \sum_{E_i} \frac{k(E_i) \cdot \exp\left(-\frac{E_i}{k_b \cdot T}\right)}{k(E_i) + \beta \cdot Z \cdot [M]} \quad (5.3)$$

where $k(E_i)$ are the specific rate constants, calculated quantum mechanically in Ref. [2], Z is the Lennard Johnes collision number, calculated as in Ref. [37], $[M]$ the bath gas concentration, β the collision efficiency, which is used as a fit parameter, and Q_{vib} the vibrational partition function [25]. The calculated falloff is presented in Fig. 5.13:

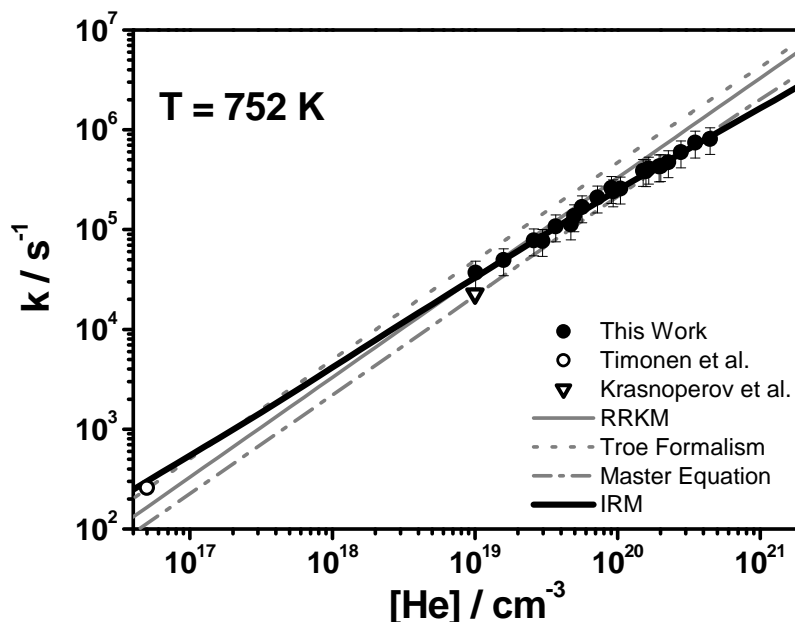


Figure 5.13: Comparison of experimental data at 752 K with theoretical models. Isolated Resonance Model.

As one can see from Fig. 5.13, there is an excellent agreement between the experimental data from this work and the isolated resonance model (IRM). A clear deviation from the linear regime in the experimental range in this work is observed, with $k \sim [M]^{0.85}$. The agreement between this model and the data from the other two direct measurements [3, 5] is satisfactory.

In Fig. 5.13 the IRM falloff is calculated with the values of $k(E)$ from Ref. [2], since the highest number of resonances have been characterized there. Several sets [46, 2, 47, 75] of quantum mechanically calculated $k(E)$ have been used and no significant differences in the falloffs were observed (see e.g. Ref. [70], where the specific rate constants are taken from Ref. [46]). In Ref. [46] spectra have been calculated and thus it was not possible to characterize some of the broader resonances. In Ref. [2] a variational calculation of resonance Siegert states based on the Kohn variational principle have been performed. Some broader resonances have been additionally characterized, but these are not important for the reaction kinetics due to their positions (high energies) and short lifetimes.

The isolated resonance model allows a test for the importance of different resonances on the thermal decomposition by taking only them into the summation in Eq. 5.3. In Fig. 5.14 the falloff curve which includes only the resonance states with excitation in the reaction coordinate (CH stretch), is compared to the one in which the rest of the resonance states are included, and the "exact" falloff.

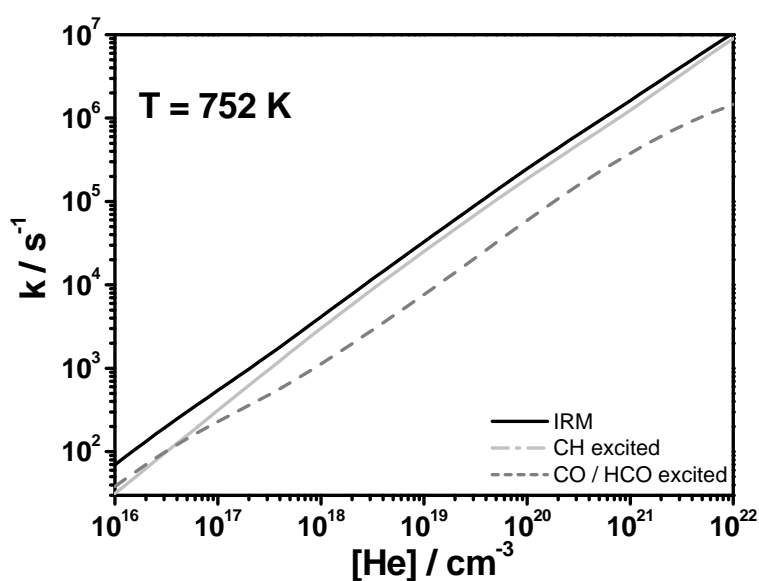


Figure 5.14: Comparison of experimental data at 752 K with IRM including different sets of resonance states.

For this calculation the resonance lifetimes from Ref. [46] have been used, since in this work the assignments of the modes which are excited are given in the paper. The resonances in which the CH vibration is excited, i. e. there is at least one energy quantum in this, contribute up to more than 80 % of the decomposition rate at pressures higher than 1 bar. The reason is the increasing with pressure stabilization rate, due to which the short living resonances became rate determining. The best way to visualize the deviations between the models is to plot these in reduced falloff curves, as shown in Fig. 5.15.

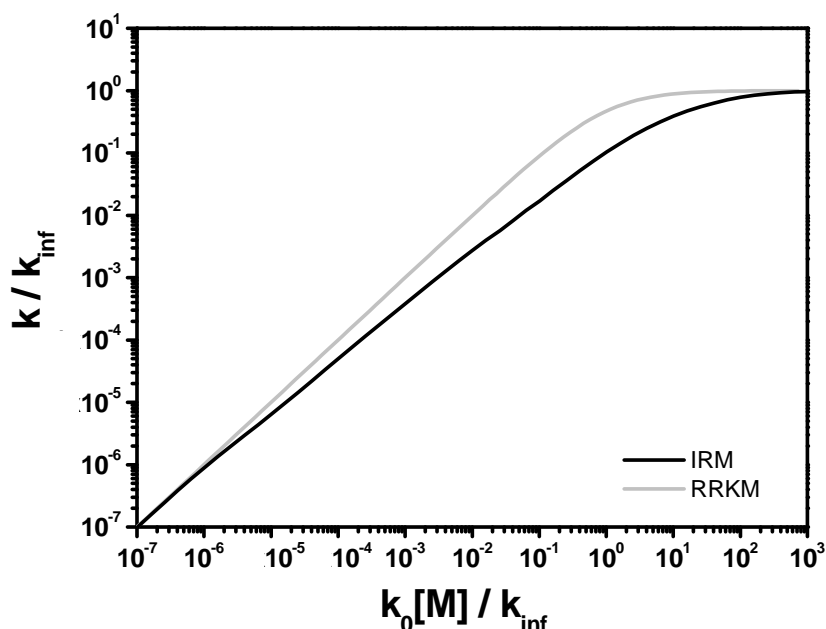


Figure 5.15: Reduced strong collision falloff curves. Comparison of statistical model (RRKM) with the isolated resonance model.

Deviations from the linear range are observable at pressures of a few tens of μbar . Furthermore an asymmetric broadening of the falloff curves is observed. The reason is the fluctuations of the specific rate constants, which are not represented with a smooth function, as in statistical theories. The strong collision falloff curves calculated with these are, in general, almost identical due to the similar energy dependence of the specific rate constant.

These effects can be explained if one considers the fluctuations of the specific rate constants of HCO. The dependence of $k(T, [M])$ on pressure (see Eq. 4.6) is determined from the competition between the collisional stabilization rate ($\beta Z[M]$) and the rate of the reaction step ($k(E)$). In the low pressure range $\beta Z[M] \ll k(E)$, or the time between collisions is longer than the time for unimolecular decay. The rate in the falloff range is determined from the competition between these processes, and in the high-pressure limit the reaction step is rate determining. In the formyl radical, from resonance to resonance, the specific rate constants vary by orders of magnitude, so resonances with shorter lifetimes can reach their high-

pressure limit at low pressures, while the broader resonances are still in their low pressure limit [7]. This causes the deviations from the linear range already in the μbar range, since the time between collisions must be sufficient for all the resonance states to be in their low pressure limit. The asymmetric broadening of the falloff curves is also a result of the fluctuations of $k(E_i)$, which determines the dominating processes (stabilization / reaction) in the falloff range and when the high-pressure limit is reached.

A question which received attention in the discussions of the decomposition of HCO is the effects of tunneling on the rate constant [6, 7, 62, 63]. The first 8 quasi bounded resonance states with finite lifetime calculated from Ref. [2] lie below the classical threshold for dissociation. These must tunnel in order to decompose and the tunneling probability is included in the resonance lifetime. In Fig. 5.16 a calculation including only the tunneling resonances is compared to the exact falloff curve.

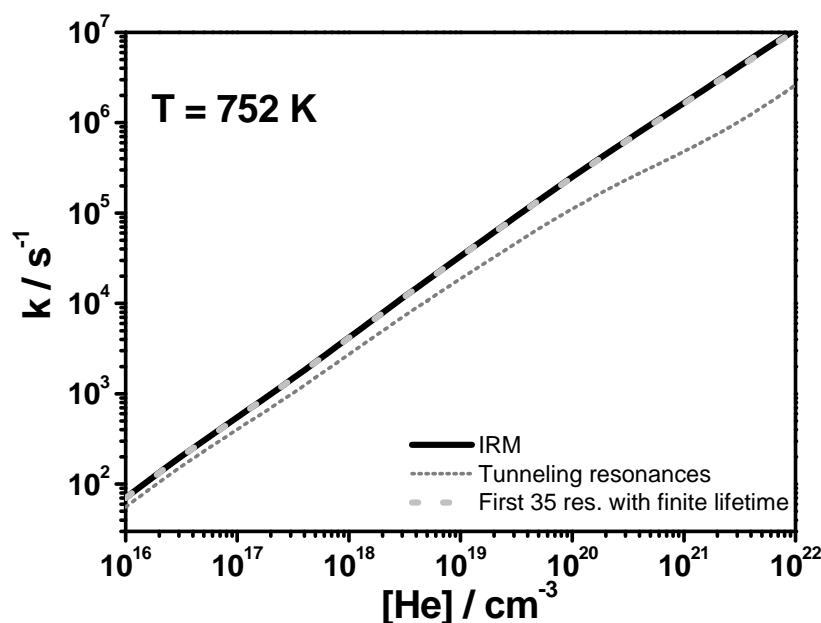


Figure 5.16: Comparison of experimental data at 752 K with IRM including different sets of resonance states.

As obvious from Fig. 5.16, at low pressures these contribute to more than 80 % of the thermal rate constant.

Including the first 35 resonance states (up to $\approx 8300 \text{ cm}^{-1}$) results in a deviation of max 5 % (for $p < 1000 \text{ bar}$, $T < 1000 \text{ K}$) from the rate calculated with 348 states (up to $\approx 20000 \text{ cm}^{-1}$). These are well characterised and can be considered as isolated, due to the large energy separation between them.

After proving the accuracy of the model, this is applied for modeling of further experimental data.

5.4.2 Falloff in Different Bath Gases

The broad range covered in the measurements in He ($T = 590 - 800 \text{ K}$, $p = 1 - 230 \text{ bar}$) allowed for an estimation of the temperature dependence of the collision efficiency, which is the only fit parameter in the calculations.

For a comparison with literature data [4] some measurements in Ar as a bath gas were performed.

The environment in flames and motors contains mainly Nitrogen, so experiments in this collision partner were performed as well. High-pressure measurements with LIF in Nitrogen are associated with some difficulties (see Sec. 5.2.2), hence it was not possible to extend the experimental ranges as much as in He. Still, as shown above the theoretical model is in good agreement with the experimental data and allows to extract reliable data of the measurements in N_2 as well.

5.4.2.1 Falloff in He

The experimentally observed pressure dependence of the rate constant at 752 K in He is in good agreement with the IRM. In this section we compare further measurements in He with the same model, in order to extract the temperature dependence of the rate constant and the collision efficiency.

The only study of the thermal decomposition rate constant in a broader pressure range is the work from Krasnoperov et. al. [5]. For comparison some direct measurements from Ref. [5] are compared to the IRM, calculated for 580 K. These are shown in Fig. 5.17 together with measurements from this work and from Timonen et al. [3] in similar temperature ranges.

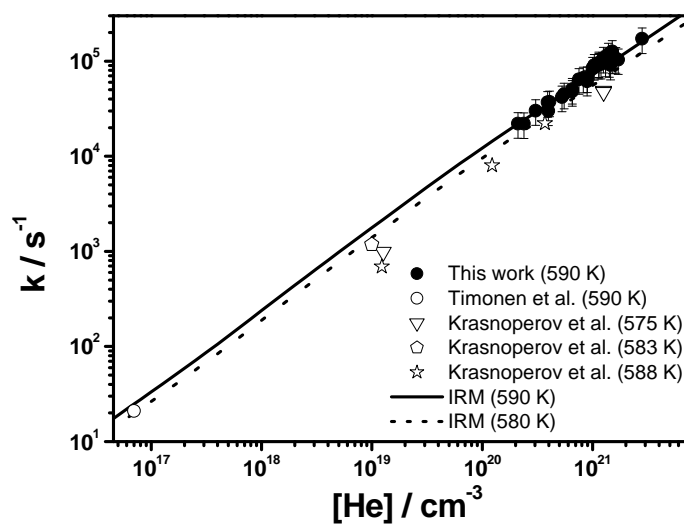


Figure 5.17: Comparison of experimental data in He with IRM, β is estimated from Eq. 5.4.

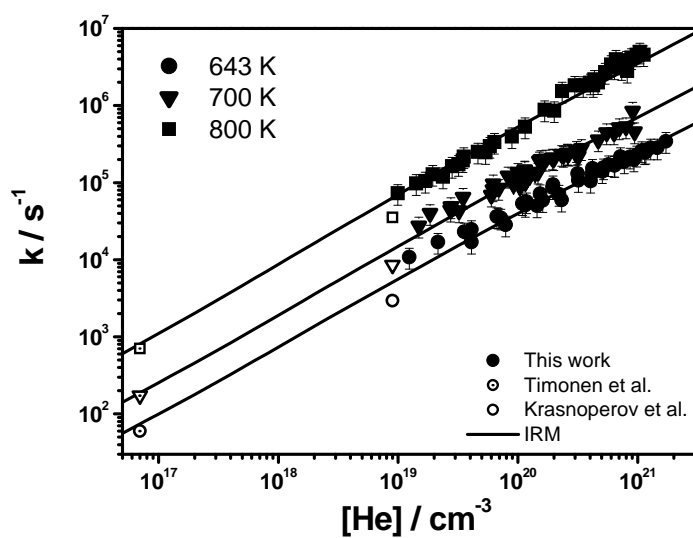


Figure 5.18: Comparison of experimental data in He with IRM, β is estimated from Eq. 5.4.

As one can see from Fig. 5.17, the agreement between the model and the available experimental data is satisfactory, as opposed to the deviations reported in [5] between the results from Refs. [3,4,5]. The statement of Ref. [5] can be partly due to the comparison of second order rate constants obtained from measurements at different pressures in Arrhenius plot, without considering possible falloff effects. To examine the temperature dependence of the rate constant and the collision efficiency some further measurements at different temperatures were performed. These are presented in Fig. 5.18. In the figure the expressions recommended in [3,5] are taken since there are only a few measurements in similar temperature ranges.

In order to prove the validity of the model and to extract information on the collision efficiency parameter in broader temperature range, the model was applied to the recombination of H and CO, which is related to the HCO decomposition by the principle of detailed balance. The direct measurements from Ahumada et al. [61] at room temperature have been used for the comparison, since no other direct measurements in He at low temperatures were available.

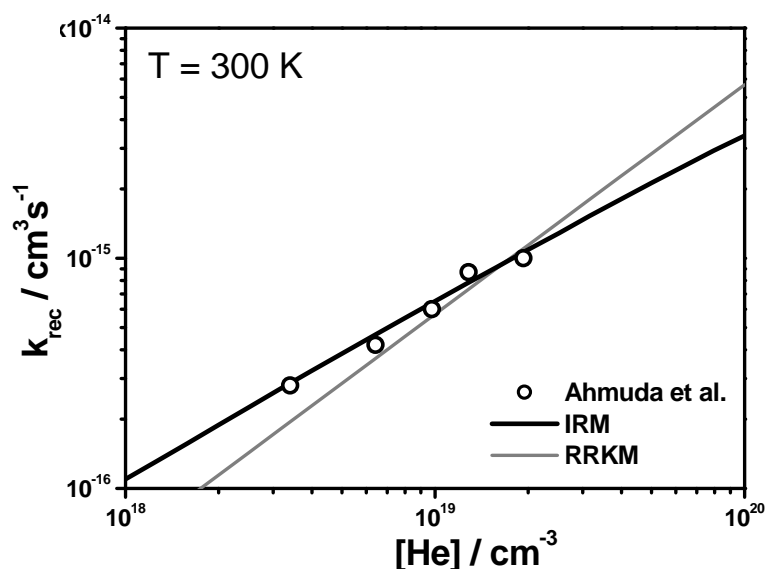


Figure 5.19: Comparison of experimental data of the recombination of H and CO [61] in He with IRM.

The experimental data is well represented from the model (Fig. 5.19). Comparison with the RRKM is also presented, and one can see that in this case the agreement is worse.

In spite that there are some studies concerning the estimation of the energy transferred per collision, till now no generally valid model is found. Hence in this study the collision efficiency has been adjusted to the experimental results. The comparison of the model to the measurements from this work, as well as the ones from Ahumada et al. [61], allow a fair estimation for the dependence of the collision efficiency in He on temperature. Furthermore, the results from the experiments performed in this work in N₂ and Ar, which will be presented later yield additional information on the collision efficiency in different collision partners. The results are presented in Fig. 5.20:

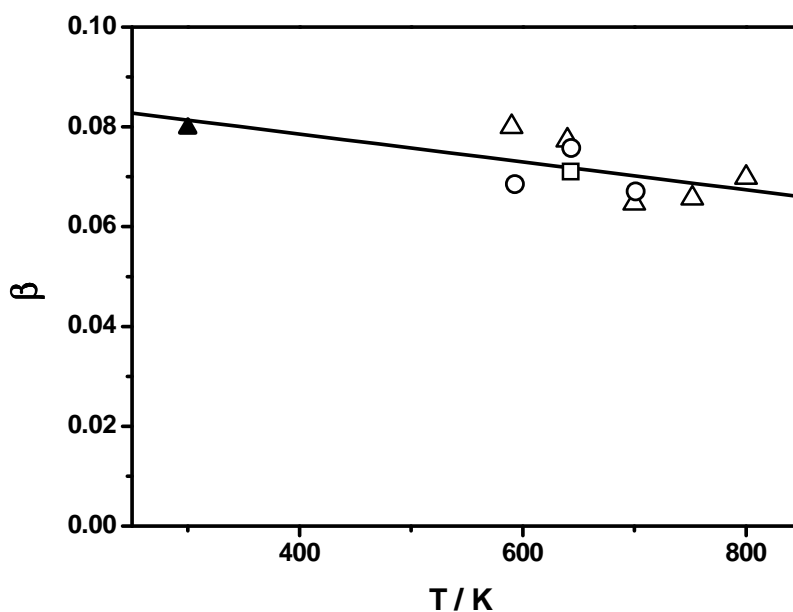


Figure 5.20: Collision efficiency obtained by fitting experimental data from this work to Eq. 5.3. Open triangles - He, open circles - N₂, open square - Ar. Filled triangle - fit of the results from Ref. [61] to Eq. 5.3. The line is linear regression of the results in all the three collision partners.

The symbols in this figure represent the values obtained by fitting the experimental

data with Eq. 5.3, where the only fit parameter is β . Slightly negative temperature dependence of the collision efficiency is observed (Fig. 5.20). As seen from the Fig. 5.20, the dependence of β on the collision partner is not significant. Linear regression of β for the three collision partners yields the following expression:

$$\beta = 0.0897 - 3 \cdot 10^{-5} \cdot \frac{T}{K} \quad (5.4)$$

Subsequently the values obtained from this fit (Eq. 5.4) are used for the calculations of the falloff curves in He presented above. The results from the fit of Eq. 5.3 to the experimental results are presented in Table 5.2.

Table 5.2: Results for the collisional efficiency, obtained by fitting the experimental data to Eq. 5.3.

T / K	300	590	593	643	700	752	800
He	0.080	0.080		0.077	0.065	0.066	0.070
N ₂			0.067	0.076	0.068		
Ar				0.071			

Considering the experimental uncertainty, a temperature independent collision efficiency of 0.07 for T = 300 - 800 K is probably a good approximation as well. In general the mean energy transferred per collision $\langle \Delta E \rangle$ is related to β , but in this case no efforts are made to extract information on this quantity. The reason is the mode specific nature of the radical, due to which, the mean energy transferred per collision depends on the mode which participates in the collision process. Hence one should consider the state specific nature of both the decomposition and activation processes and treat all these processes on microscopic level. Further more rotational effects are not considered.

Based on a fit of the isolated resonance model, the following expression is recommended for modeling:

$$k(T, [He]) = 7 \cdot 10^9 (T/K)^{-0.18} \left[\frac{[He]}{10^{19} \text{ cm}^{-3}} \right]^{0.85} \exp \left(-\frac{16.6 \frac{\text{kcal}}{\text{mol}}}{RT} \right) \text{ s}^{-1} \quad (5.5)$$

This represents the falloff curve calculated with the isolated resonance model within 30 % for $T = 500 - 1000$ K and $p = 0.01 - 200$ bar.

The temperature dependence of the rate constant at different pressures is presented in Fig. 5.21.

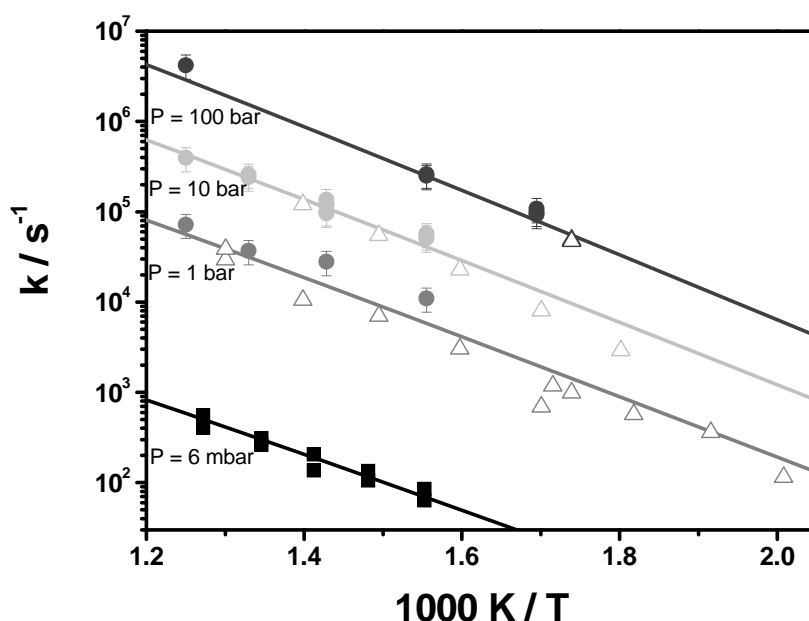


Figure 5.21: Isobar Arrhenius representation of the formyl decomposition rate constant. The lines are calculated with the IRM for the respective pressures (given below the curves). The filled circles are results from this work, open triangles - Krasnoperov et al. [5], filled squares - Timonen et al. [3].

The agreement between the model and the available experimental data is pleasing. The IRM explains the reason for the discrepancies between the low pressure rate constants reported from Refs. [3, 4, 5] and confirms the effects of the non-statistical microscopic dynamics of HCO on its macroscopic kinetics. The temperature dependence of the collision efficiency determined above allows reliable extrapolation of the results for $k(T, [M])$. The results on the dependence of this parameter on the collision partner are presented below.

5.4.2.2 Falloff in Ar

For comparison with further measurements on the formyl decomposition from the literature [3,4] some measurements in Ar were done. They are presented in Fig. 5.22:

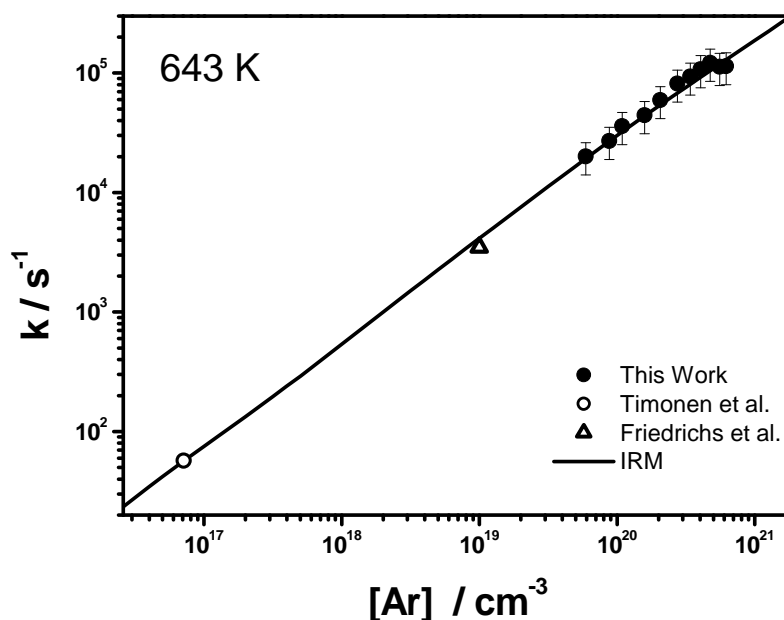


Figure 5.22: Comparison of experimental data on the decomposition of HCO in Ar with IRM.

In this case also good agreement is observed, adopting the collision efficiency obtained from Eq. 5.4. The results from this work show that the weak collision effects are similar in He and Ar in the range under consideration.

The model is also applied to the measurements of the recombination at room temperature from Ahumada et. al. [61]. The results are presented in the following figure:

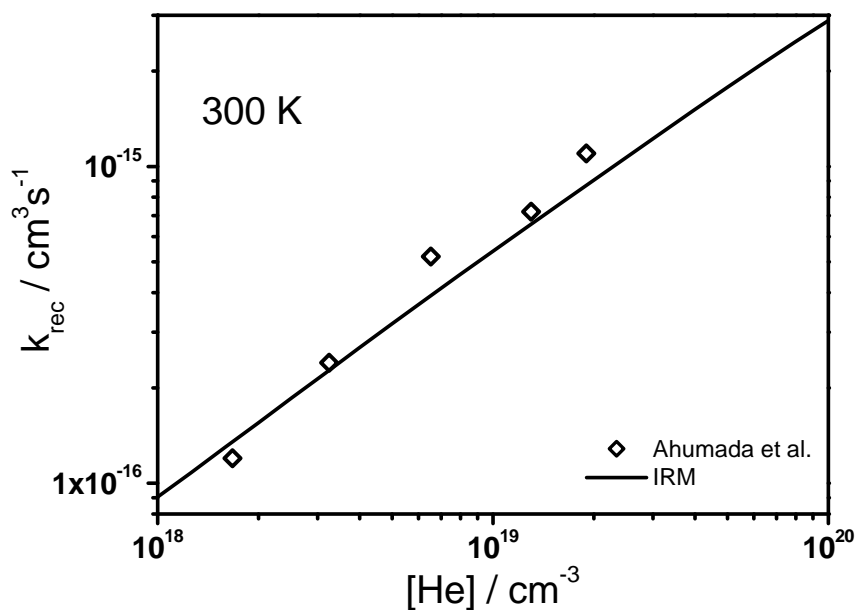


Figure 5.23: Comparison of experimental data of the recombination of H and CO [61] in Ar with IRM.

As seen from Fig. 5.23 a satisfactory agreement between the experimental data from Ref. [61] with the IRM is observed.

5.4.2.3 Falloff in N_2

After proving the accuracy of the model we present some measurements in N_2 , which are interesting for combustion modeling. As a fit parameter the uncertainty of the collision efficiency depends on the range in which the experiments are performed. The collision efficiency from Eq. 5.4 is adopted for the falloff curves in N_2 , since no significant deviations of this from the one in He are observed as discussed above. The results are presented in Fig. 5.24.

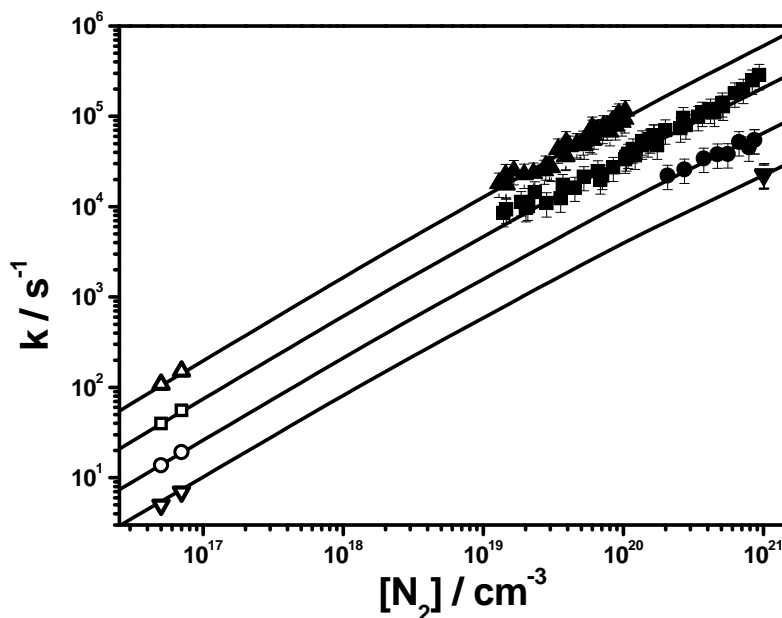


Figure 5.24: Falloff curve for the rate constant in nitrogen as bath gas. Solid symbols: experimental results from this work, open symbols: results from the expression recommended in Ref. [3], down triangles: $T = 546$ K, circles: $T = 593$ K, squares: $T = 643$ K, up triangles: $T = 700$ K, solid line: rate constant calculated from 5.3, adopting the collision efficiency from Eq. 5.4.

The following analytical expression (Eq. 5.6), extracted from the calculated with the IRM falloff curves is recommended for combustion modeling:

$$k(T, [N_2]) = 6 \cdot 10^9 (T/K)^{-0.18} \left[\frac{[N_2]}{10^{19} \text{ cm}^{-3}} \right]^{0.85} \exp \left(-\frac{16.6 \frac{\text{kcal}}{\text{mol}}}{RT} \right) \text{ s}^{-1} \quad (5.6)$$

The rate constant calculated with this expression represents the falloff calculation with the IRM within 30 % in the temperature range 500 - 1000 K and pressures 0.01 - 300 bar.

The goal of this work was to find a theoretical approach able to represent the experimental results in broad pressure and temperature ranges. Deviations of the rate constant from the low pressure range are observed in the μbar range. Extrapolation of the "low pressure" rate constants reported until now with statistical

theories, which predict linear pressure dependence of the rate constant up to $p > 100$ bar, is associated with significant uncertainty. For comparison in Fig. 5.25 the expression from Ref. [3], which is widely used in combustion models, is compared to the pressure dependence extracted from this work (IRM, Eq. 5.6).

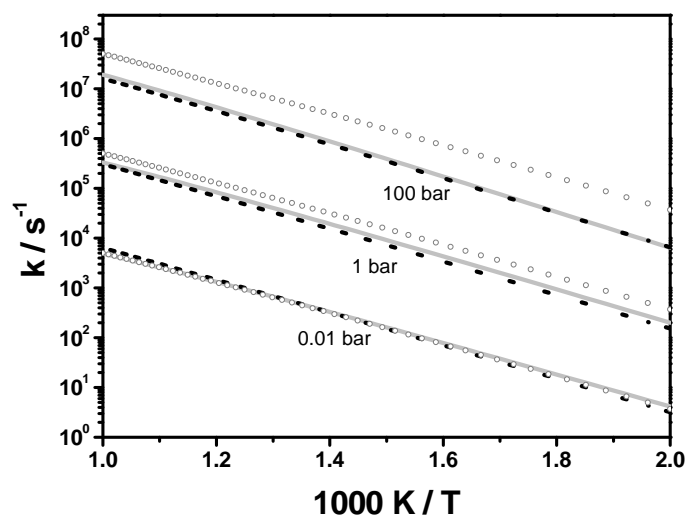


Figure 5.25: Comparison of the rate constants calculated with: isolated resonance model (gray line), Eq. 5.6 (black dashed line), expression recommended from Ref. [3] (open gray circles).

One sees that at lower pressures the expressions from Ref. [3] (performed at a few mbar) and this work give similar values for the rate constant, but the differences are significant at higher pressures. The curves are calculated for 0.01, 1 and 100 bar as indicated in the Fig. 5.25.

Extrapolation of Eq. 5.6 beyond the given ranges, especially considering the temperature range is not recommended.

5.4.3 Isotope Effect

The DCO radical is considered in the literature to be an intermediate case between statistical and non statistical behavior. As stated above, the fluctuations of its state specific rate constants are not mode specific. The macroscopic decomposition

rate of the radical is of a considerable interest for the theoretical modeling, since this analysis would show if the thermal decomposition is influenced only by the fluctuations of the microscopic rate coefficient, or if the non - statistical behavior is just a consequence of the mode specific dynamics of the HCO radical. This question is important for modeling of other mode specific / non - regular species with strong fluctuating specific rate constants.

A comparison of the results from the RRKM model and the IRM to the experimentally observed pressure dependence of the rate constant is shown in Fig. 5.26.

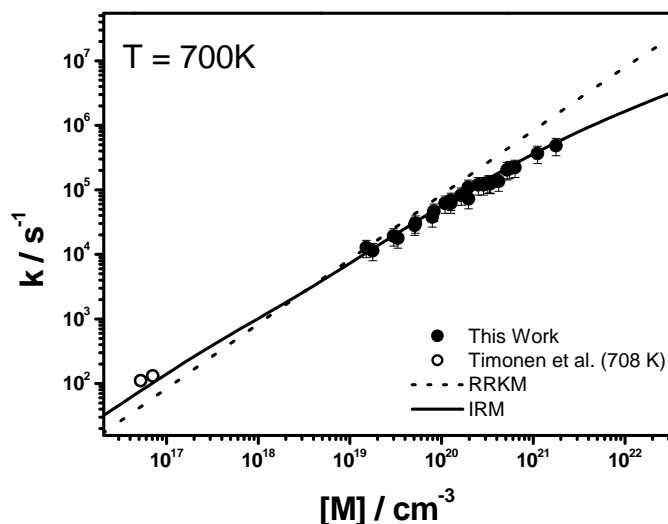


Figure 5.26: Comparison between predictions of statistical theories and the IRM for DCO.

The RRKM model predicts a linear pressure dependence of the rate constant in the experimental range on this work (> 100 bar), which is not supported from the experimental results. In Fig. 5.26 direct measurements from Ref. [3] are used for comparison with the models, since for the DCO decomposition no expression is recommended in Ref. [3]. No comparison of $k(T,[M])$ with further statistical models for DCO are performed, since no significant effects on the shape of the falloff curve calculated with other statistical approaches are expected, as shown for the HCO decomposition.

Since the structures of the two radicals are similar, the differences in β are expected to be insignificant. For this reason, as well as because of the narrower experimental range of the measurements on the DCO decomposition, we adopt the collision efficiency from Eq. 5.4 for both radicals.

In Fig. 5.27 a comparison between the decomposition rates of HCO and DCO at 700 K is presented.

The formyl radical (HCO) decomposes faster compared to DCO, which has a higher density of states. This is in agreement with the predictions of statistical theories (see Eq. 4.2), although neither of the radicals fulfills the assumptions of statistical theories. In both cases good agreement between the IRM and the experimental results is observed. Further results of the DCO decomposition at different temperatures are presented in Fig. 5.28.

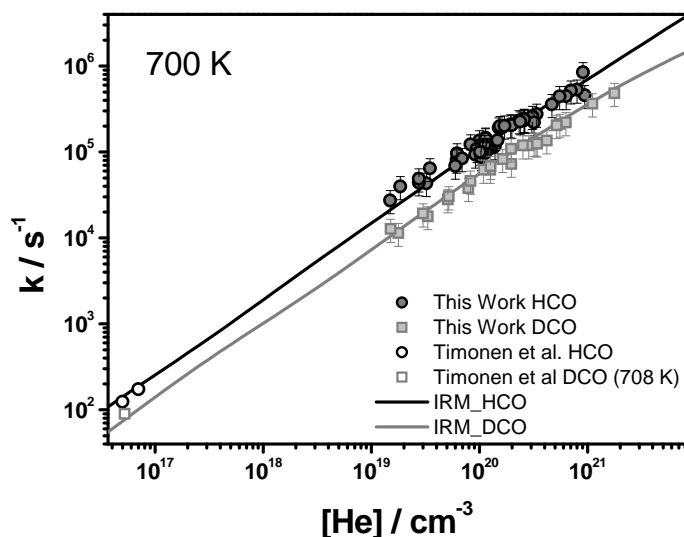


Figure 5.27: Isotope effect on the thermal decomposition of formyl radical.

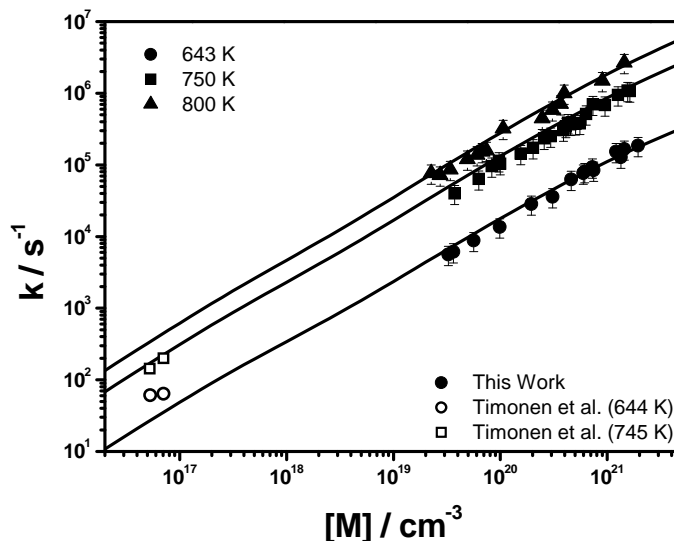


Figure 5.28: Comparison of experimental data on the thermal decomposition of DCO in He with IRM (Black Line). Filled symbols - this work, open symbols - Timonen et al. [3].

In order to check which of the resonance states are important for the kinetics of this radical, calculations including different sets of resonance states have been performed as well. The first 85 resonances (up to 8700 cm^{-1}) are found to be important for its kinetics for $T < 1000\text{ K}$, $p < 1000\text{ bar}$.

Concerning the number of resonances characterized, one should say that the calculations and the experiments on the specific rates of DCO are much more complicated than the ones of HCO. Due to the higher density of states and the stronger anharmonic effects in DCO, the obtained spectra are difficult to interpret. In [2] the resonances are calculated from a variation of Siegert states and more states are found in comparison with other studies, where the resonances are mainly characterized from the calculated spectrum. The falloff curves for DCO have also been calculated with the specific rates from [54], where 173 resonance states have been characterized, but a few broader resonances (actually 2 resonances with widths 24 and 122 cm^{-1}) at relative low energies (respectively 6770 and 7360 cm^{-1}) were missing in Ref. [54]. Differences between the calculated falloff curves were observed at pressures higher than 200 bar, but these are within 30% for $p < 1000\text{ bar}$.

The basic difference between the HCO and DCO radicals is that HCO shows a regular (mode specific) microscopic dynamics, while the resonance states in DCO can not be unambiguously assigned. The results from this work show that the thermal rate constant depends basically on the resonance lifetimes.

The IRM allows good representation of the experimental data from this work and the literature. Further improvements of the model would be considering the influence of rotational excitation on the reaction step. Concerning the activation process, one should examine the dynamics of the energy transfer processes depending on the mode which is excited. These processes are poorly understood till now and no data on these is found in the literature for any non - statistical reactions.

5.5 Conclusions

Extensive experimental studies on the thermal decomposition of formyl radical (HCO) and its heavier isotope DCO ($p = 1 - 230$ bar, $T = 590 - 800$ K) in different collision partners have been performed. Comparison of statistical models to the experimental results from this work show that these are in poor agreement.

The state specific dynamics of both the HCO and DCO radicals have been extensively studied [2, 46, 47, 48, 49, 50, 51, 52, 54, 55]. This allowed to implement the "exact" resonance lifetimes, calculated quantum mechanically, in an RRKM based approach. The extended range of experimental conditions allowed to determine the dependence of the collision efficiency, which was the only fit parameter in the calculations, on the temperature and the collision partner. This model allowed to represent the observed temperature and pressure dependence of the rate constant for both HCO and DCO radicals. A comparison of the thermal rate of the mode specific HCO and the non - regular DCO show that the deviations from statistical models result from the fluctuations of the specific rate constants, or the mode specificity is not critical for the macroscopic decomposition of the radicals.

Significant broadening of the falloff curves is observed compared to the predictions of statistical theories. Deviations from the linear dependence of the rate constant on pressure (low pressure limit) are observed in the μ bar range. This discards the assumptions that at 1 bar the rate constant is still in the low pressure

range. Extrapolations of the rate constant, based on measurements of the "low pressure" rate assuming linear dependence of the pressure, which have been used till now in combustion modeling, can introduce significant uncertainties.

The following expression is recommended for combustion modeling:

$$k(T, [N_2]) = 6 \cdot 10^9 T^{-0.18} \left[\frac{[N_2]}{10^{19} \text{ cm}^{-3}} \right]^{0.85} \exp \left(-\frac{16.6 \frac{\text{kcal}}{\text{mol}}}{RT} \right) \text{ s}^{-1} \quad (5.7)$$

Further improvements of the model would be to consider the influence of rotational excitation on the microscopic dynamics of the radical. Till now no systematic studies on the specific rate constants for higher J are available. Another point is that if one treats the decomposition as a state specific phenomena, one could anticipate the same for the activation / deactivation processes. There are no studies on this matter up to now.

This work is the first experimental evidence for measurable non statistical effects of the macroscopic kinetics of a radical. The IRM predicts higher low pressure and lower high-pressure rate constants, or broader falloff curves than the ones calculated with statistical models.

5.6 Outlook

The non - statistical effects in the microscopic dynamics of small reaction species have been widely investigated in the last few years. Nowadays it is known that the microscopic decomposition rates of all the molecules fluctuate to some extent [1], though in most of the cases their specific rate constants can be described with a proper average function with sufficient accuracy.

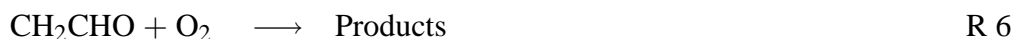
Except for HCO and DCO, non - statistical effects are reported as well for the specific rate constants of HOCl [65], HO₂ [66], H₂S [76], NO₂ [77], HNO [78] and others. These are more pronounced in molecules with low density of states in the energy regime relevant for their kinetics (close to the barrier for dissociation). The question where is the limit of statistical theories and in which cases the non - statistical microscopic dynamics is important for their macroscopic decomposition rate, which is of practical relevance.

Chapter 6

The Recombination of CH₂CHO and O₂

6.1 Introduction

The investigations presented in this chapter are concentrated on the recombination of vinoxy radicals, CH₂CHO, with O₂ in He as a bath gas.



Vinoxy radicals are important intermediates in photochemical processes in the atmosphere. They are formed in the alkene ozonolysis [9, 79], which is a sink for unsaturated hydrocarbons in atmospheric environments. They have been found as major products of reactions of oxygen atoms with primary olefins [10, 80]. As product of the reactions of C₂H₄, C₂H₃ or C₂H₂ with O(³P) (see Ref. [11, 81, 82] and references cited therein), CH₂CHO is an important intermediate in the combustion of hydrocarbons. For example the formation of CH₂CHO by the recombination of O(³P) with C₂H₄ [11, 83] is a critical step for fuel consumption in ethylene flames.

Due to the relatively high oxygen concentrations in combustion and atmospheric environments, R 6 is the main oxidation pathway for vinoxy radicals. Hence its kinetics is of considerable interest for atmospheric and combustion modeling.

There are some experimental data on the recombination of vinoxy radicals with

O₂ [12, 13, 14, 15] at room temperature and pressures up to 400 Torr. In Refs. [12, 13, 14], the radicals were generated by laser photolysis (193 nm) of methyl vinyl ether (MVE) and detected by laser induced fluorescence (337 nm).

Gutman and Nelson [12] measured the recombination rate at pressures between 1.5 and 100 Torr in N₂ and SF₆ as collision partners ($T = 298$ and 476 K). The data were not compared to a theoretical model due to the narrow experimental range and the weak pressure dependence observed. As most probable mechanism for the reaction, the simple recombination to a stable O₂CH₂CHO was inferred. It was suggested that a pressure independent pathway (see Fig. 6.1), namely the 1,4 H atom migration in the complex followed by a fast fragmentation can not be excluded. The mechanism was supported by a product analysis, in which OH and CH₂O were detected as reaction products.

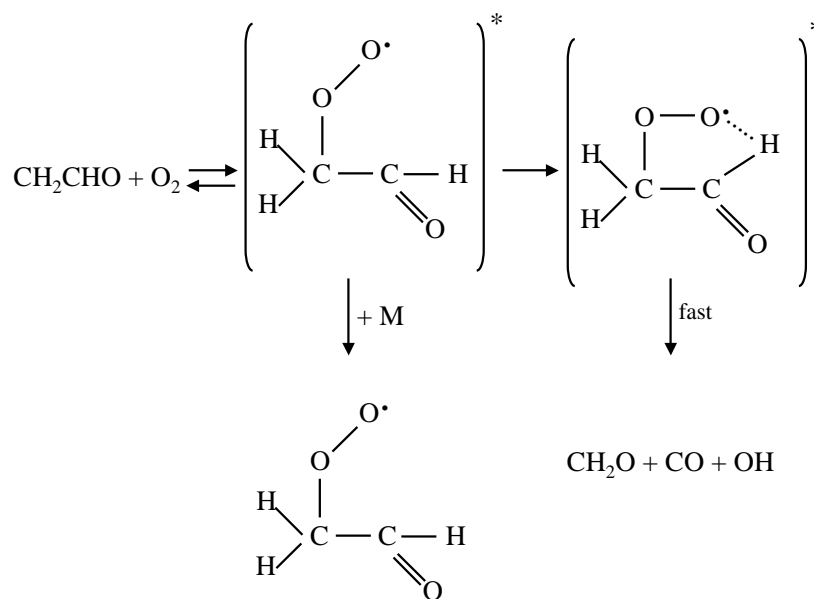


Figure 6.1: Reaction mechanism for the recombination of vinyloxy radicals with oxygen as proposed in Ref. [12].

According to this mechanism, the pressure dependence of the rate constant is determined by the sum of a pressure dependent addition and a pressure indepen-

dent fragmentation. However, it was not possible to support this mechanism, since the product analysis experiments were inconclusive. Investigations on the rate constant at lower pressures, where this mechanism is expected to have a stronger impact on the falloff behavior, were beyond the accessible experimental range. Hence the authors concluded that the simple addition is the most probable reaction pathway.

Applying a similar experimental approach, Lorenz et al. [13] performed measurements in He as collision partner at 298 K ($p = 7.5 - 210$ Torr). The results were analyzed assuming a simple recombination mechanism, despite that OH radicals were identified as a reaction product in this work as well.

Oguchi et al. [14] performed experiments in He as bath gas ($p = 3 - 200$ Torr, $T = 298$ K). Although that the recombination to the adduct has been found to play a dominant role under these experimental conditions, OH radicals have been identified as a direct reaction product as well. The OH product yields decreased from 20 to 10 % in the pressure range from 10 to 200 Torr. Theoretical modeling of the observed pressure dependence has not been presented.

Zhu et al. [15] applied CRDS to monitor the decay of the vinoxy radicals, generated by laser photolysis of MVE. The experiments were performed at 298 K and $p = 2.5 - 400$ Torr with N_2 , SF_6 and CF_4 as collision partners. Time resolved measurements of glyoxal ($(CHO)_2$) revealed a slow formation rate, which excludes $(CHO)_2$ as a direct reaction product. It was not possible to examine the appearance rate of H_2CO , which was detected as a product as well.

For the data analysis in Refs. [12, 13, 15] it is assumed that the recombination leads entirely to the formation of a stabilized complex. Hence the Troe formalism (see Sec. 4.2.2) for simple recombination reactions has been applied in order to represent the experimental results in Refs. [13, 15], but this does not account for the formation of a complex with a finite lifetime. In the last case S - shaped falloff curves are observed, and the formalism presented in Sec. 4.2.2 must be modified, as discussed in Sec. 4.2.4.

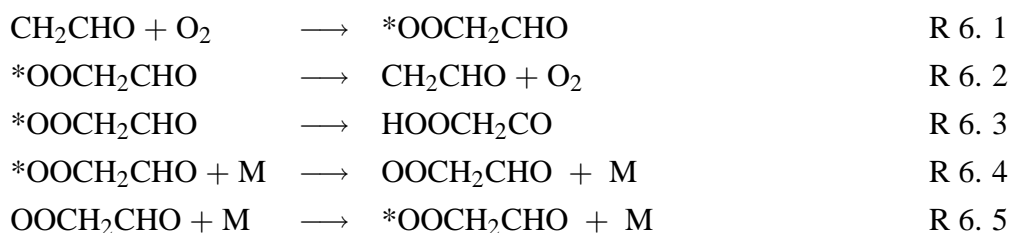
The present work was performed in collaboration with the group of C. Fittschen (see Ref. [84]). In this study laser photolysis / laser induced fluorescence (347.4 nm) has been employed to monitor the temporal decay of CH_2CHO at $T = 298 - 550$ K and $p = 1.4 - 5000$ mbar. More details on the experimental setup and the

evaluation of the signal time profiles are given in Ref. [16, 84], and the results will be discussed later in this work.

The only theoretical study in which a comparison with experimental results from Ref. [15] is presented is the work from Oguchi et al. [85]. The Master Equation analysis performed postulated a simple recombination mechanism. The molecular parameters for this are calculated at the B3LYP/6-31G(d) level of theory. The threshold energy for the recombination and the downward transferred energy have been adjusted to the experiments from Ref. [15] ($E_0 = 3.6$ kJ / mol). The experimental data reported from Ref. [15] are limited to room temperature and pressures above 2.5 Torr.

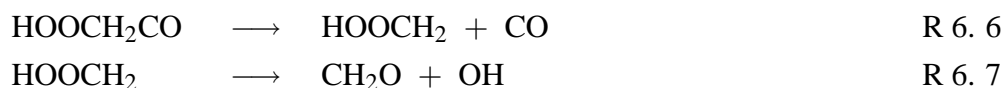
Extended theoretical analysis of the energetics and the kinetics of the title reaction were performed by Kuwata et al. [79, 86] and Lee et al. [82]. However, no comparison with experimental data was presented.

The detailed reaction mechanism can be represented with the following scheme:



The asterisk of the complex, *OOCH₂CHO, indicates rotational / vibrational excitation from the chemical activation, M is the collision partner.

Theoretical calculations (see e. g. Ref. [79, 82]) predict that HOOCH₂CO decomposes further on a very fast time scale, so that R 6. 3 can be considered as irreversible under practical relevant temperature and pressure environments ($T < 1000$ K, $p > 10$ mbar). The lowest possible fragmentation pathways are:



In order to reveal the reaction mechanism one needs information on the potential energy surface (PES). The barrier heights of the entrance and exit channel barriers are critical for the pressure dependence of the rate constant, as well as for the reac-

tion mechanism. In general, *ab initio* methods yield reliable data on the molecular structure and frequencies, but the reaction barriers, which are rate determining, are associated with great uncertainty.

Fig. 6.2 represents a simplified schematic PES of the title reaction.

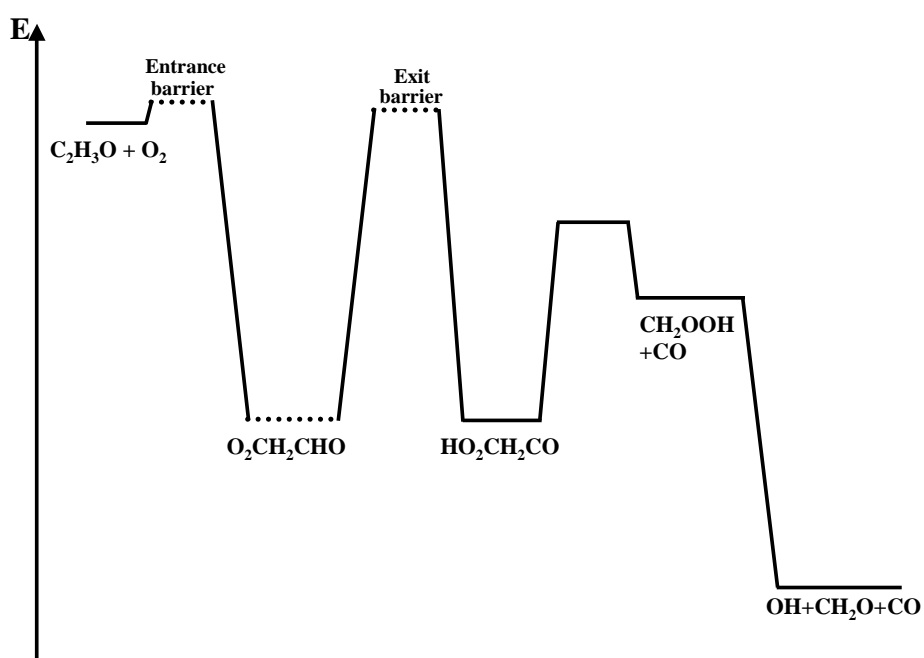


Figure 6.2: Schematic representation of the energy diagram for the recombination of CH_2CHO and O_2 .

The simple addition mechanism (to stable O_2CH_2CHO), postulated from the experimental studies till now, supposes a high exit barrier. In this case the channel to products is closed and in the low pressure limit the rate constant is pressure dependent (third order). The pressure dependence of the rate constant can be represented with the formalism presented in Sec. 4.2.2.

For a low exit barrier the reaction is pressure independent and leads to fragmentation. The lifetime of the complex in this case is too short to allow for stabilization. For comparable entrance / exit barrier heights competition between the reaction

(re-dissociation / isomerization) and stabilization is expected. The rate constant is pressure independent in the low pressure limit, in which the forward reaction is faster than the collisional stabilization. This is determined by the ratio between the rate constants of the competing reaction processes, which introduces a complicated temperature dependence. The lifetime of the complex determines the falloff behavior of the rate constant. In the high-pressure limit the reaction is pressure independent and is governed by the addition step. Hence for this class of reactions S - shaped falloff curves are expected [18,44], as discussed in Sec. 4.2.4.

Information on the rate determining barriers can be obtained from investigations of the temperature dependence of the rate constant in the high-pressure limit. It is difficult to extract information on the entrance barrier from experiments in the low pressure range, since in this several reaction channels play a role. Under certain external conditions, the complex can become thermally unstable and one can investigate its thermodynamical properties. Information on further reaction channel barriers can be obtained if the experimentally accessible temperature and pressure ranges are broad enough.

The goal of this work is to obtain experimental information on the rate determining barriers, as well as on the thermodynamic stability of the complex. The aim is to model the rate constant of the title reaction at various external conditions and provide simple expressions for it, which can be directly used for combustion and atmospheric modeling.

6.2 Experimental Details

Laser photolysis of ethyl vinyl ether at 193 nm (Lambda Physik, Compex 102, ArF) has been employed to generate the vinyloxy radicals:



In order to estimate the radical concentrations, the absorption coefficient of ethyl-vinyl ether is assumed to be identical to the one of methyl-vinyl ether $\sigma(193\text{nm}) = 8 \times 10^{-18} \text{ cm}^2$ [87, 88] ($\Phi = 1$ [89]). The laser fluence of the photolysis laser was varied between 2.5 and 25 J cm⁻² leading to radical concentrations from

10^{13} to 10^{14} cm^{-3} . Information on the precursor concentrations are given in the appendix. All experiments were performed under pseudo - first order conditions under excess concentrations of oxygen ($[\text{CH}_2\text{CHO}] \ll [\text{O}_2]$). Low initial radical concentrations were employed in order to suppress the influence of secondary reactions. These were found to be insignificant under the experimental conditions in this work, which was proved as described in Sec. 5.3.

The vinoxy radicals were excited by an excimer (Compex 102, Lambda Physik, XeCl) pumped dye laser (Scanmate 2E, Lambda Physik, p - Terphenyl), operating at 337 nm. The fluorescence signal was passed through a monochromator (Zeiss, M4 QIII) at (400 ± 20) nm and detected with a photomultiplier tube (Hamamatsu R212). The experiments were performed in He as collision partner. More details on mixture preparation, precursor, reaction partner and bath gas purities are given in Sec. 3.2.2.

6.3 Experimental results

In this work the rate constants of the different reaction channels have been investigated by variation of the external conditions. The measurements were performed in the high-pressure limit, so the rate determining factors were temperature and the $[\text{O}_2]$ concentration. The investigations at different temperatures are presented in the following sections.

6.3.1 Low Temperature Range

Theoretical calculations predict that the adduct, $\text{O}_2\text{CH}_2\text{CHO}$, is thermodynamically stable at low temperatures (e.g. $\Delta H(0 \text{ K}) = -112 \text{ kJ / mol}$ Ref. [14]). Therefore the collisional activation of OOCH_2CHO (R 6. 5.) can be safely considered to be insignificant at temperatures up to 470 K. Applying the steady state approximation for $[\text{*OOCH}_2\text{CHO}]$ one can solve the rate equations for the mechanism presented in Sec. 6.1. Hence the temporal decay in the vinoxy concentrations is given with the following expression:

$$-\frac{1}{[\text{O}_2]} \frac{d \ln [\text{CH}_2\text{CHO}]}{dt} = k_{6.1} \frac{k_{6.3} + k_{6.4} [M]}{k_{6.2} + k_{6.3} + k_{6.4} [M]} = k_6 \quad (6.1)$$

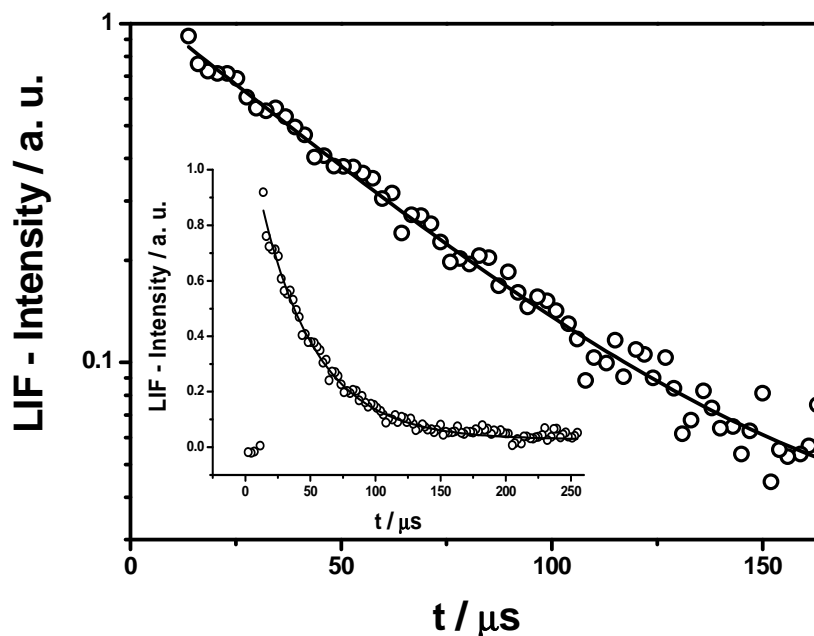


Figure 6.3: Typical time profile for the recombination of vinoxy and O₂ at 298 K and 14.6 bar. The fit with Eq. 6.2 gives a pseudo-first order rate constant of $2.4 \times 10^4 \text{s}^{-1}$. With an oxygen concentration of $7.9 \times 10^{16} \text{cm}^{-3}$ the recombination rate constant is $k_{6,1} = 3 \times 10^{-13} \text{cm}^3 \text{s}^{-1}$.

The obtained signal time profiles (see Fig. 6.3) were evaluated with a mono exponential fit function:

$$[\text{CH}_2\text{CHO}] = [\text{CH}_2\text{CHO}]_0 \exp(-k_6[\text{O}_2]t) \quad (6.2)$$

where in the high-pressure limit k_6 is equal to $k_{6,1}$ (see also Sec. 4.2.4).

Considering the reaction mechanism, employing higher oxygen concentrations shifts the reaction to the products. Hence $[\text{O}_2]$ was increased by raising the temperature, in order to suppress the thermal re-dissociation. The recombination rate constant was investigated in the temperature range of 298 - 473 K and pressures from 4 to 46 bar.

6.3.2 Intermediate Temperature Range

At temperatures higher than 470 K, OOCH_2CHO becomes thermodynamically unstable, since its thermal lifetime is comparable to the timescale of the recombination. This is supported from the experimental signal time profiles at these conditions. In the temperature range 470 - 530 K a relaxation to equilibrium was observed (see Fig. 6.4). Hence the collisional activation at temperatures above 470 K should be accounted for. The measurements were performed close to the high-pressure limit, which is necessary in order to assure that collisional stabilization is reached [90], in other words that the pressure independent route (isomerization and further fragmentation) do not play a role $k_{6,3} \ll k_{6,4}[\text{M}]$. In any case the contributions from the pressure independent route are minor (less than 5 %).

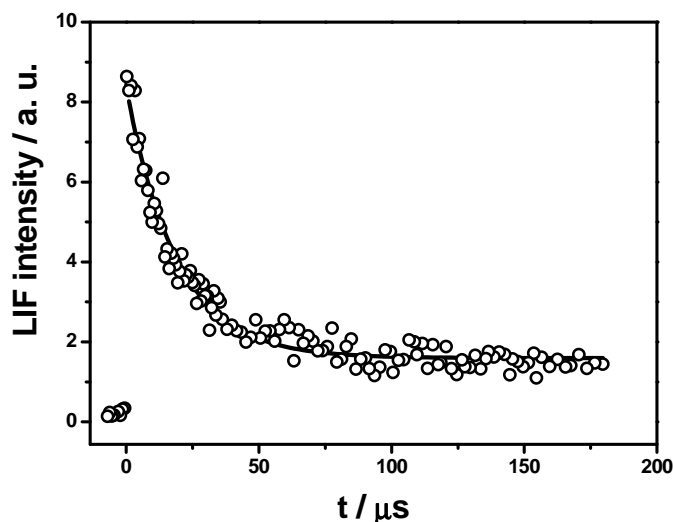


Figure 6.4: Typical time profile for the equilibrium $K = k_{6,1} / k_{6,2}$ at 516 K and 5.3 bar. The fit with Eq. 6.5 gives $k_{6,1} = 3.6 \times 10^{-13} \text{cm}^3 \text{s}^{-1}$ and $K = 3.6 \times 10^{-17}$ with an oxygen concentration of $1.2 \times 10^{17} \text{cm}^{-3}$.

The relatively long time in which the vinoxy concentration stays constant allows for the assumption that under these conditions $k_{6,3}$ is small compared to $k_{6,2}$, so for the data interpretation it was assumed that $k_{6,3} = 0$. Applying the steady state approximation for the concentration of $[\text{*OOCH}_2\text{CHO}]$ with the mechanism

presented in Sec. 6.1, one obtains:

$$-\frac{d[\text{CH}_2\text{CHO}]}{dt} = \frac{k_{6.1}k_{6.4}[\text{O}_2][M][\text{CH}_2\text{CHO}] - k_{6.2}k_{6.5}[M][\text{OOCH}_2\text{CHO}]}{k_{6.2} + k_{6.4}[M]} \quad (6.3)$$

$$-\frac{d[\text{OOCH}_2\text{CHO}]}{dt} = \frac{k_{6.2}k_{6.5}[M][\text{OOCH}_2\text{CHO}] - k_{6.1}k_{6.4}[\text{O}_2][M][\text{CH}_2\text{CHO}]}{k_{6.2} + k_{6.4}[M]} \quad (6.4)$$

These equations can be solved with standard methods (e. g. Laplace Transform Method [30]). The solution (Eq. 6.5) has been used to fit the obtained signal time profiles in this temperature range.

$$\frac{[\text{CH}_2\text{CHO}]_t}{[\text{CH}_2\text{CHO}]_0} = \frac{\frac{1}{K} + [\text{O}_2] \exp(-([\text{O}_2] + \frac{1}{K})(\frac{k_{6.1}k_{6.4}[M]}{k_{6.2} + k_{6.4}[M]})t)}{\frac{1}{K} + [\text{O}_2]} \quad (6.5)$$

where in the high-pressure limit $\frac{k_{6.1}k_{6.4}[M]}{k_{6.2} + k_{6.4}[M]}$ is equal to $k_{6.1}$ and the equilibrium constant K is:

$$K = \frac{k_{6.1}k_{6.4}}{k_{6.2}k_{6.5}} \quad (6.6)$$

This fit function enabled us to extract the equilibrium constant and rate constant for the recombination of vinoxy and O₂ from each signal. The values obtained for the recombination rate constant $k_{6.1}$ with Eq. 6.5 at 473 K are consistent with the ones received by the monoexponential decays, performed at higher [O₂] concentrations (see Sec. 6.3.1).

Information on the equilibrium constant was extracted at $T = 473 - 530$ K, $p = 2 - 25$ bar.

On longer time scales loss of vinoxy (bi - exponential decays) was observed. There is not a straightforward way to determine if the loss is due to the isomerization or to other competing processes (e. g. pseudo first order reaction with the precursor, impurities etc.). Since it is difficult to estimate the rates of all the possible competing processes, this experimental range was not evaluated. Considering the time profiles under these experimental conditions, one can speculate that the barrier for the isomerization is not much higher than the one for the re-dissociation. In general one could extract information from these bi - exponential decays on $k_{6.3}$, assuming that the loss is entirely due to the isomerization (see e.

g. Ref. [16]). In this work investigations on $k_{6,3}$ have been performed at higher temperatures (see Sec. 6.3.3).

At lower temperatures (respectively higher oxygen concentrations), the equilibrium is shifted to the product side and was not observed on the experimental time scale. The rate of thermal decomposition of the adduct ($k_{6,1}/K$) increases strongly with temperature, so at higher temperatures the relaxation in equilibrium was too fast for the time resolution in this work.

6.3.3 High Temperature Range

Above 570 K thermodynamical equilibrium between the reactants and the stabilized adduct is reached on a time scale faster than the time resolution of this work. The observed mono exponential decays of $[\text{CH}_2\text{CHO}]$ (see Fig. 6.5) were assumed to be entirely due to the isomerization channel.

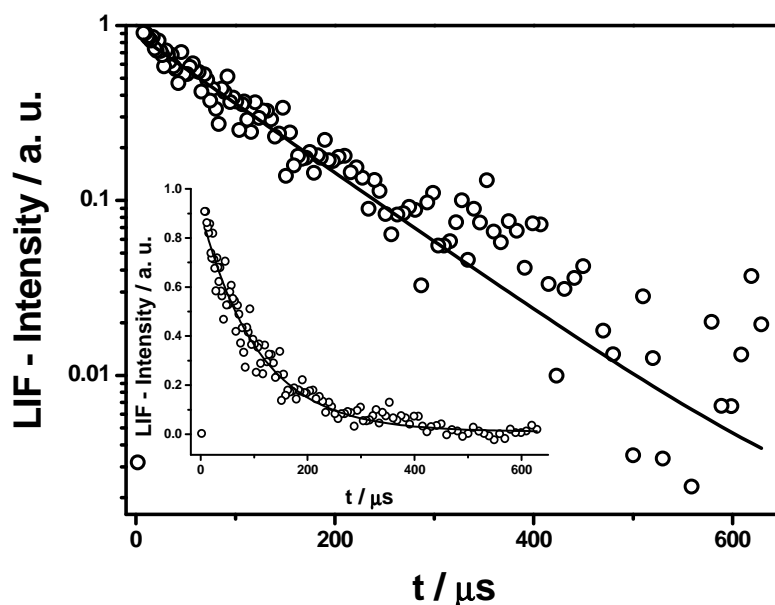


Figure 6.5: Typical time profile for the complex decomposition at 618K and 2.7 bar. The fit with Eq. 6.10 gives a pseudo-first order rate constant of $9.2 \times 10^3 \text{ s}^{-1}$. With an oxygen concentration of $1.2 \times 10^{17} \text{ cm}^{-3}$ and equilibrium constant of $7.9 \times 10^{-19} \text{ cm}^3$ the isomerization rate constant is $k_{6,3} = 9.7 \times 10^4 \text{ s}^{-1}$.

The equilibrium constant, which has been determined in the previous section relates the concentrations of the reaction species:

$$\frac{d[OOCH_2CHO]}{dt} = K[O_2] \frac{d[CH_2CHO]}{dt} \quad (6.7)$$

Applying the principle of detailed balance,

$$\frac{d[CH_2CHO]}{dt} + K[O_2] \frac{d[CH_2CHO]}{dt} + \frac{d[HOOCH_2CO]}{dt} = 0 \quad (6.8)$$

solving the rate equation for R 6.3 and substituting Eq. 6.8, one obtains:

$$\frac{d[CH_2CHO]}{dt} + K[O_2] \frac{d[CH_2CHO]}{dt} = -k_{6.3}K[O_2][CH_2CHO] \quad (6.9)$$

Hence the decays in the vinyloxy concentrations were fitted with the following expression:

$$[CH_2CHO] = [CH_2CHO]_0 \exp \left\{ - \left(k_{6.3} \frac{K[O_2]}{1 + K[O_2]} \right) t \right\} \quad (6.10)$$

No pressure dependence of the isomerization rate constant was observed in the pressure range 2 - 28 bar, which points out that R 6.3 was in the high-pressure limit under these experimental conditions. The temperature range covered was 570 - 660 K.

6.4 Discussions

The literature data (Refs. [12, 13, 15, 14]) on the rate constant of the above reaction are in poor agreement. Two of the studies [13, 15] give expressions for the falloff behavior of the rate constant at room temperature, based on modeling with the Troe formalism for simple addition reactions. As discussed above, this mechanism is not complete. In order to get a reliable data on the kinetics of the title reaction, one needs information in broad experimental ranges and detailed theoretical modeling.

The goal of this work is to extract information of the reaction mechanism and the

kinetics of the recombination of CH_2CHO and O_2 .

At low temperatures the kinetics is determined by the recombination to a stable adduct, $\text{O}_2\text{CH}_2\text{CHO}$. This becomes thermodynamically unstable at higher temperatures, which allows to extract information on the equilibrium constant for the recombination / back dissociation. Third law analysis of the results yields the reaction enthalpy at 0 K. The isomerization rate constant has been extracted at still higher temperatures.

The experiments performed in this study allowed for determination of the rate constants for addition, re-dissociation and isomerization channels of the title reaction in the high-pressure limit. The results provide information on the reaction channel barriers, which are compared to the calculations on the potential energy surface, performed by B. Viskolcz [16]. The information on the energetics of the title reaction allows a reliable modeling of the falloff behavior of the rate constant of the title reaction. The data reported from Ref. [84] in the falloff range have been used for the preformed Master Equation analysis (Ref. [16]). The results from this are further parametrized with the formalism presented in Sec. 4.2.4. The extracted analytical expressions allow for extrapolation of the rate constant for $T = 298 - 500$ K.

6.4.1 The Reaction Threshold

The complicated kinetics of the title reaction requires accurate data on its potential energy surface.

The *ab initio* calculations performed by B. Viskolcz have been compared to the experimental results in this work and used for the calculations (presented in Ref. [16]). The molecular parameters have been calculated on the MP2/6-311G(d,p) level of theory [91]. In general *ab initio* methods yield reliable data on the vibrational frequencies and the rotational constants. Only a fine tuning of these has been made when necessary [16], in order to represent the experimental results. The uncertainty in the calculated barriers, which have a major influence on the rate constants, is higher. The theoretical methods used to calculate these will not be further discussed, since in this work the barrier heights have been adjusted to the experimental data. The high-pressure rate constants have been calculated

from the standard transition state expression (Eq. 4.9). The entropy contributions to these are accounted for by the partition functions, calculated with the molecular parameters from Ref. [16]. The experimentally determined threshold barriers for the respective temperature ranges are presented in the following sections.

6.4.1.1 The Recombination Barrier.

The experiments performed in this work allowed to extract information on the temperature dependence of the high-pressure addition rate constant ($k_{6,f}^{\infty} = k_{6,1}^{\infty}$ see Sec. 4.2.4). The experimental results signify that the reaction barrier for the recombination is very small (about 1 kJ / mol), i. e. the transition state is quite loose. The *ab initio* calculations on the molecular parameters for "looser" transition states are associated with higher uncertainty. In this case the entropy contribution (determined by the molecular geometry and frequencies) to the rate constant can be significant. Due to the weak T - dependence of the recombination rate constant, and the narrow temperature range, determination of the reaction barrier only from the experimental data is difficult as well. Hence the kinetics of the R 6 in the whole falloff range has been modeled by a Master Equation analysis, which allowed to extract the entrance threshold barrier. The results from this will be discussed later in this work, since in order to obtain reliable data with this approach, one needs accurate information on potential energy surface, which has been obtained as described below.

6.4.1.2 The Reaction Enthalpy

At higher temperatures the adduct becomes thermodynamically unstable. The relaxation into equilibrium in the intermediate temperature range (see Sec. 6.3.2) points out that in this the energetically favorable pathway is the re-dissociation (compared to the isomerization). In this work data on the equilibrium constant have been extracted in the temperature range 470 - 530 K. Comparison with the data obtained in Ref. [84] allow to extend the experimental range to T = 420 - 530 K.

In order to obtain the reaction enthalpy at 0 K, a third law analysis has been performed. The entropy contributions to the equilibrium constant were calculated

with the molecular parameters calculated *ab initio* [16]. A good agreement between these and the experimental data was found (see Fig. 6.6). The reaction enthalpy at 0 K was adjusted to the experimental data, which yielded

$$\Delta H_R^\theta(0K) = -97 \text{ kJ/mol} \quad (6.11)$$

The thermodynamical data needed for the analysis are given in the appendix. A van't Hoff plot of the equilibrium constant K_p is presented in Fig. 6.6.

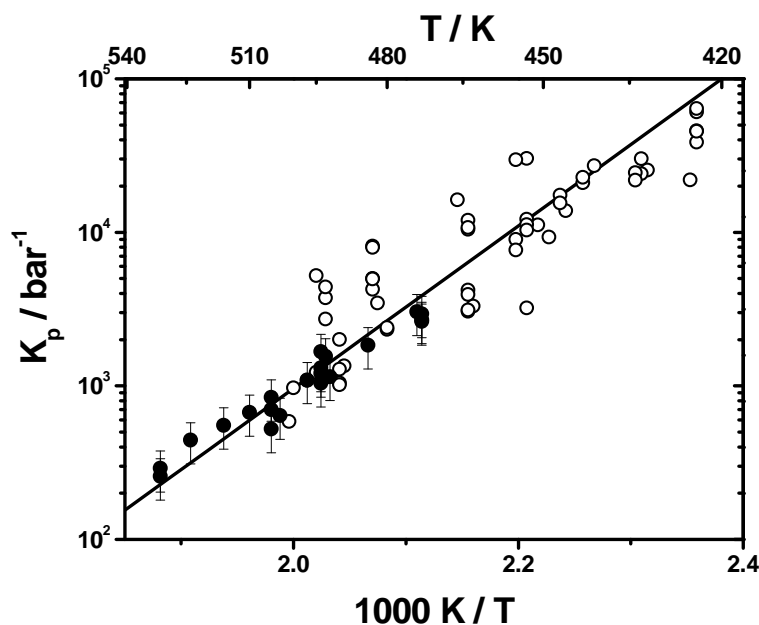


Figure 6.6: van't Hoff plot of the equilibrium constant. Filled circles - this work, open circles - Ref. [84], solid line - results from the third law analysis. For further discussions see text.

The equilibrium constant for the temperature range 420 - 530 K can be represented with the following expression:

$$K_P(T) = 1.2 \times 10^{-4} \left(\frac{T}{\text{K}} \right)^{-1.2} \exp \left(\frac{97 \text{ kJ/mol}}{RT} \right) \text{ bar}^{-1} \quad (6.12)$$

As stated in Sec. 6.1 the only study in which theoretical calculations are compared to experimental data from Ref. [15] is the work from Oguchi et al. [14].

In Ref. [14] G2 method has been used to estimate the bond dissociation energy $\Delta H_R^\theta(0K) = -112$ kJ/mol. The scarce experimental data from Ref. [15] did not allow for a validation of the theoretically predicted value.

6.4.1.3 The Isomerization Barrier

The rate of thermal decomposition of the adduct ($k_{6,2}$) shows a strong positive temperature dependence. Hence at higher temperatures a fast pre - equilibrium has been established on the experimental time scale (see Sec. 6.3.3). $k_{6,3}$ was determined from the loss of vinoxy observed experimentally with the equilibrium constant, calculated with the parameters obtained in the previous section.

The results for the isomerization rate constant are presented in the following Arrhenius plot.

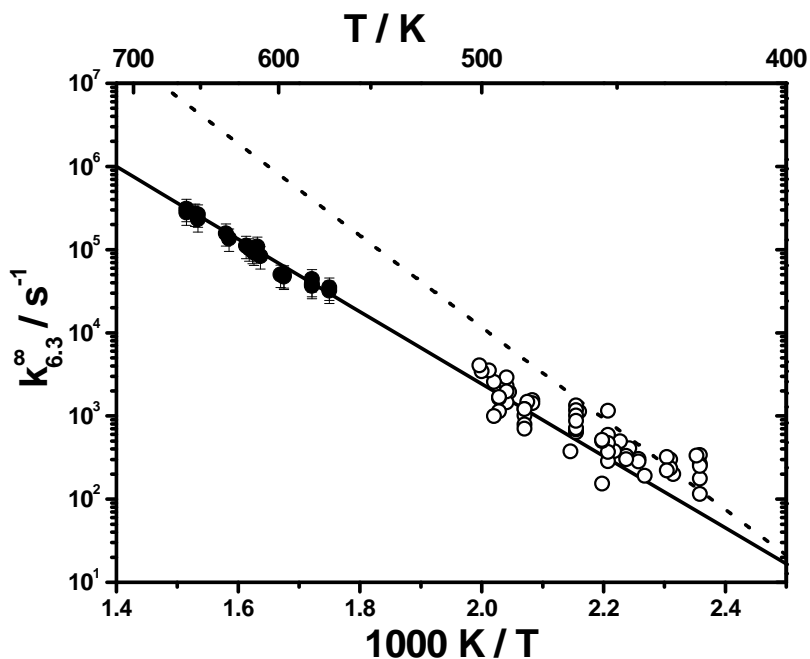


Figure 6.7: Arrhenius plot of the isomerization rate constant. The filled circles are results from this work, open circles - from Ref. [84]. The lines are result of TST calculations, respectively: solid - for $k_{6,3}^{\infty}$, dashed - for $k_{6,2}^{\infty}$. See text for further discussions.

The fluctuations in the results from Ref. [84] observed in Fig. 6.7 can be partly due to the data evaluation. In [84] the rate coefficients were extracted by fitting biexponential signal time profiles with a complicated fit function, which yields a relation between the rate coefficients for the re-dissociation and the isomerization. Since in this temperature range these have similar magnitude (see Fig. 6.7), the results are very sensitive to the noise and to the experimental uncertainty. The threshold barrier at 0 K for the isomerization (Eq. 6.13) is determined by a comparison of the experimental results to a transition state theory (TST) calculation (Eq. 4.9) with the molecular parameters calculated *ab initio* in Ref. [16]:

$$\Delta E(0K) = 82 \text{ kJ/mol} \quad (6.13)$$

The parameters for the analysis are listed in the appendix. The temperature dependence of the isomerization rate constant in the temperature range 420 - 660 K can be represented with the following expression:

$$k_{6.3}^{\infty}(T) = 1.2 \times 10^{12} \exp\left(-\frac{83 \text{ kJ/mol}}{RT}\right) \text{ s}^{-1} \quad (6.14)$$

The barrier for the re-dissociation equals the sum of the reaction enthalpy $\Delta H(0K) = 97 \text{ kJ/mol}$ and the recombination barrier (1 kJ/mol). Hence with a re-dissociation barrier of about 98 kJ/mol and the parameters listed in the appendix, one can calculate the temperature dependence of $k_{6.2}^{\infty}$. The results from a TST calculations on this are presented in Fig. 6.7, and a linear fit of these yields the following expression for the rate constant in the temperature range 420 - 660 K:

$$k_{6.2}^{\infty}(T) = 1.2 \times 10^{15} \exp\left(-\frac{105 \text{ kJ/mol}}{RT}\right) \text{ s}^{-1} \quad (6.15)$$

The comparison of the rate constants show, that in spite of the lower enthalpy barrier, the back dissociation is favored compared to the isomerization at temperatures above 400 K. The reason is the larger entropy contributions to the re-dissociation rate constant. In other words the transition state for the re-dissociation is looser than the one for the isomerization.

$k_{6.3}^{\infty} \ll k_{6.2}^{\infty}$ was a necessary assumption for the investigation on the equilibrium

constant performed in this work. These were performed above 470 K, where $k_{6.3}^{\infty}$ is more than 5 times smaller than $k_{6.2}^{\infty}$. Furthermore, one should compare the time scale on which the equilibrium is established, which depends on [O₂], to the experimental time scale. The temporal decay of [CH₂CHO] allow for the assumption, that the loss of [CH₂CHO] due to the isomerization was insignificant under the experimental conditions applied for investigations of the equilibrium constant. The experimentally determined barrier heights have been used for the Master Equation analysis [92] of the falloff curves of the title reaction.

6.4.2 Pressure Dependence of the Rate Constant

In spite of the postulated simple addition mechanism, the product analysis performed in Refs. [12, 13, 15] signifies that a direct fragmentation route exists. Unfortunately the investigations concerning this possible reaction pathway were inconclusive, but signify that the entrance and the exit channel barriers have comparable heights. This is supported by the results from Ref. [14], in which investigation of the OH product yields were performed, but in this study no modeling of the rate constant has been presented.

The experimental results from this work show clearly that the reaction proceeds via a complex formation. It was not possible to apply directly the Troe Formalism for complex - forming reactions presented in see Sec. 4.2.4, since the information on the rate constant in the falloff- and low pressure- ranges were not sufficient. Hence a steady state Master Equation analysis [43, 93, 9], which accounts for the population distribution maintained by the chemical activation, reaction and stabilization processes had to be performed (Ref. [16]).

As stated above, the heights of the entrance- and exit- channel barriers are crucial for the reaction kinetics. These are adjusted to represent the experimental data from this work and Ref. [84]. The barrier for re-dissociation of the adduct is determined to be $\Delta E(0 \text{ K}) = 98 \text{ kJ / mol}$ and for the exit channel - $\Delta E(0 \text{ K}) = 82 \text{ kJ / mol}$. These have been used as input parameters for the further analysis. In spite of the low barrier for the recombination ($\Delta E(0 \text{ K}) = 1 \text{ kJ / mol}$), the transition state is tight, hence RRKM / ME calculations have been performed (Ref. [16]). The specific rate constants have been calculated with a direct count procedures (see Sec.

4.1, Ref. [16]). The calculations were performed for $J = 44$, which is the average quantum number for $\text{O}_2\text{CH}_2\text{CHO}$ for room temperature. This was not varied for different temperatures, since due to the tight character of the transition states it is expected that the uncertainty introduced from this parameter is insignificant [16]. For the falloff calculations (Ref. [16]) the vibrational frequencies and rotational constants calculated *ab initio* [16] for reactants, products and transition states have been slightly adjusted to the experimental results. The ME analysis yields a ratio between the high- and low- pressure limiting rate coefficients [16]. In order to represent the experimental data adopting a threshold barrier for the recombination of 1 kJ / mol, it was necessary to scale down the last three frequencies of the entrance transition state with a factor of 0.55. More discussions on the matter are given in Ref. [16]. This resulted in a higher re-dissociation rate constant, due to the introduced additional looseness of the transition state, and subsequently lower low-pressure rate constant for R 6.

The steady state population distribution of the complex has been calculated with a stepladder model [16, 20]. The mean down transferred energy per collision has been adjusted to the experimental results from this work and the literature data. These are best represented with $\Delta E_{SL} = 500 \text{ cm}^{-1}$, temperature-independent [16]. Due to the great experimental uncertainty, considering the weak p- and T- dependence of the rate constant, it was not possible to examine the dependence of this parameter on the collision partner.

The results are presented in the following figures.

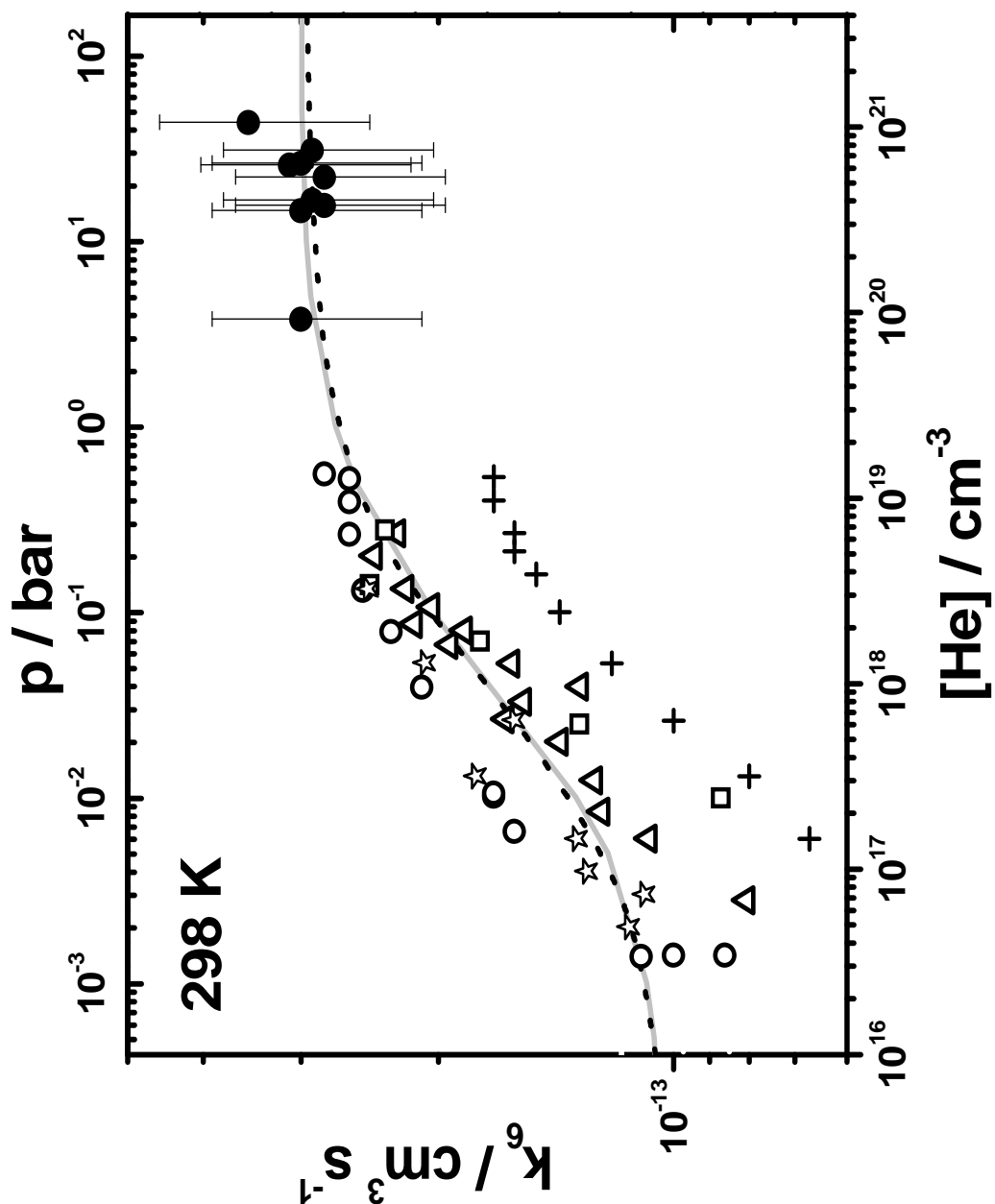


Figure 6.8: Falloff curve for reaction R 6 at $T = 298 \text{ K}$. The solid gray line represents the results from the Master Equation analysis (Ref [92]), the black dashed line - the best fit with Eq. 4.20. The symbols are experimental results as follows: filled circles - this work, open circles - Fittschen and co. [16], open stars - Gutman et al. ([N₂]) [12], open triangles - Oguchi et al. [14], open squares - Lorenz et al. [13], black cross - Zhu et al. ([N₂]) [15].

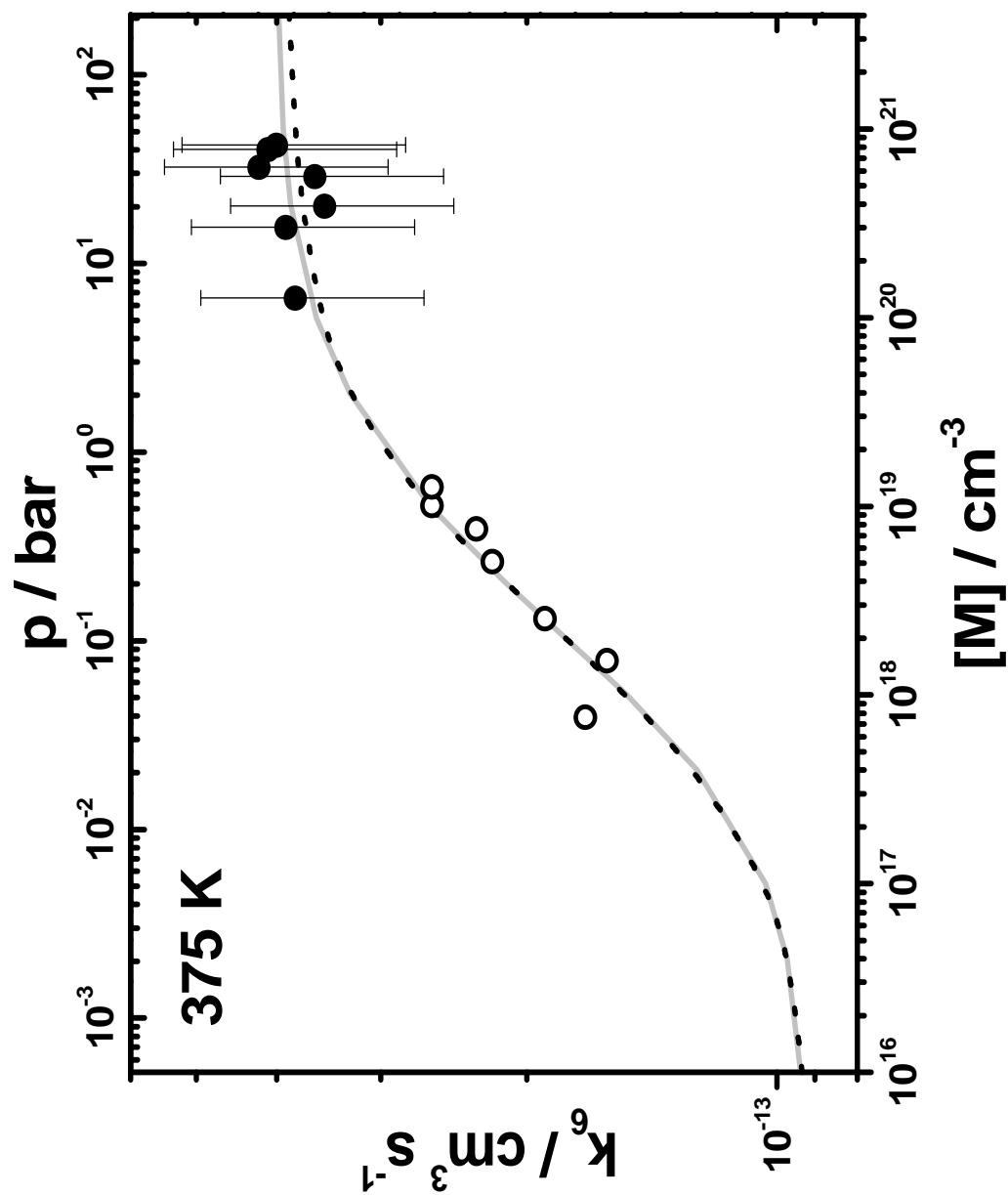


Figure 6.9: Falloff curve for reaction R 6 at $T = 375 \text{ K}$. The solid gray line represents the results from the Master Equation analysis (Ref [92]), the black dashed line - the best fit with Eq. 4.20. The symbols are experimental results as follows: filled circles - this work, open circles - Fittschen and co. [16].

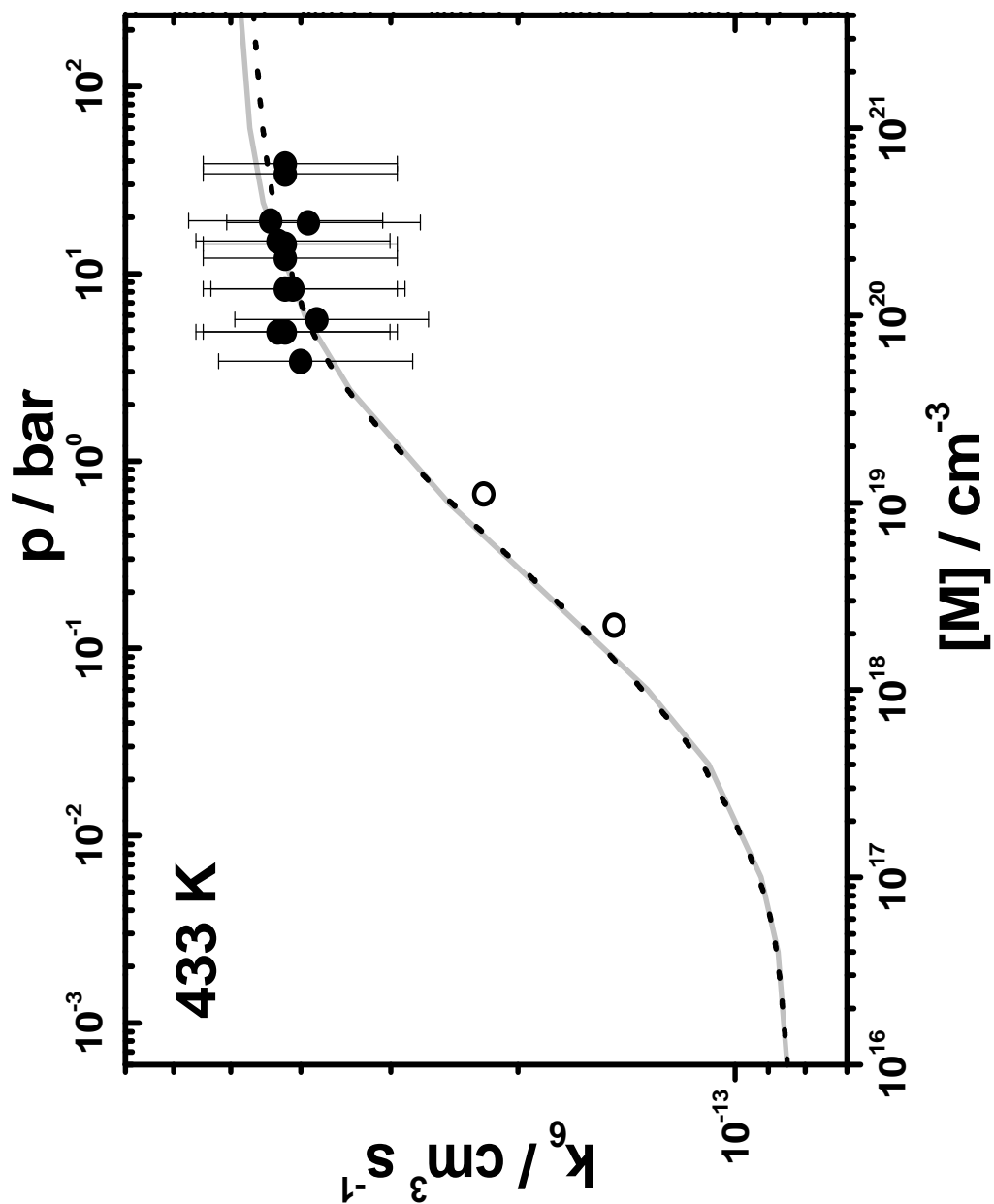


Figure 6.10: Falloff curve for reaction R 6 at $T = 433 \text{ K}$. The solid gray line represents the results from the Master Equation analysis (Ref [92]), the black dashed line - the best fit with Eq. 4.20. The symbols are experimental results as follows: filled circles - this work, open circles - Fittschen and co. [16].

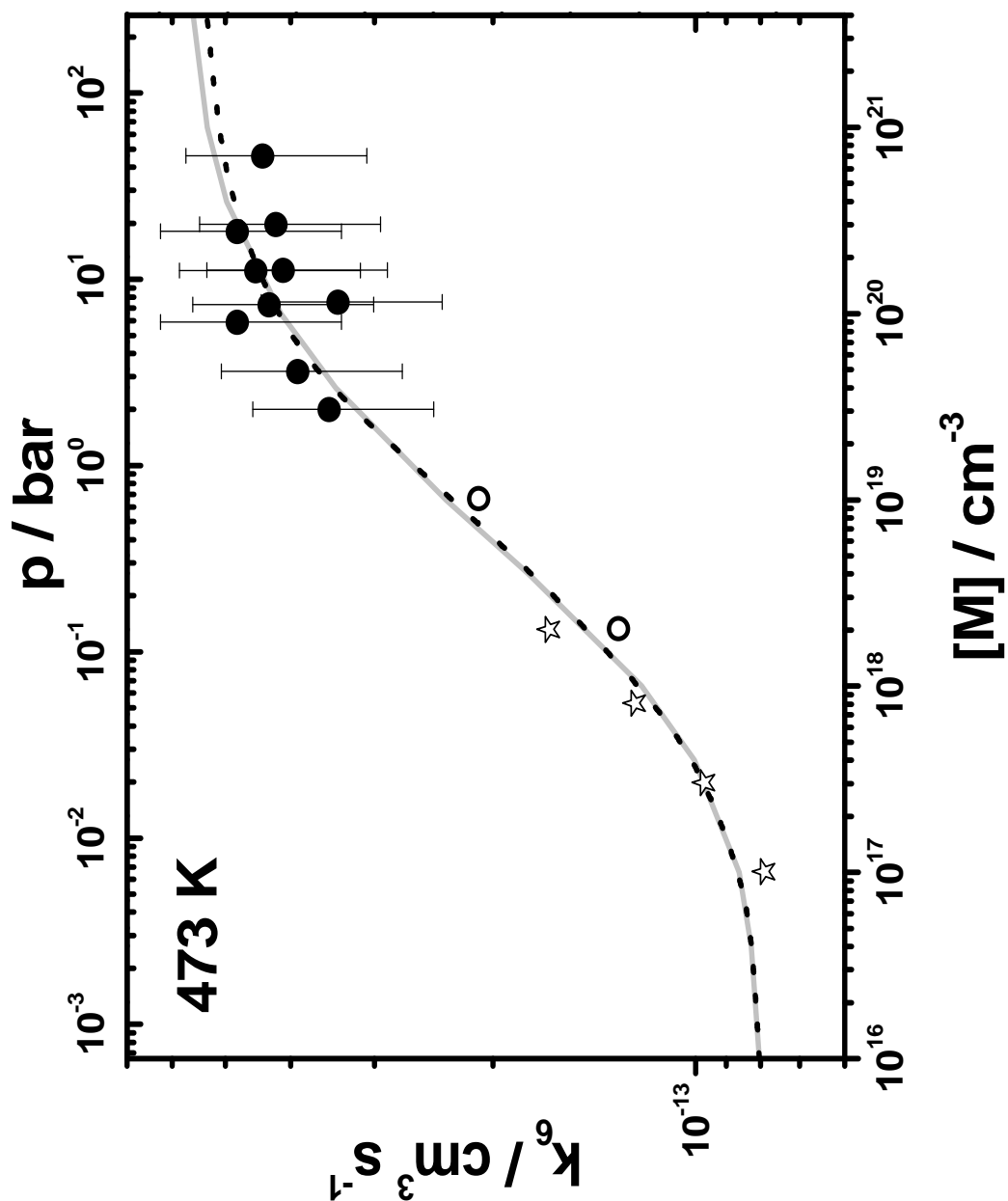


Figure 6.11: Falloff curve for reaction R 6 at $T = 473 \text{ K}$. The solid gray line represents the results from the Master Equation analysis (Ref [92]), the black dashed line - the best fit with Eq. 4.20. The symbols are experimental results as follows: filled circles - this work, open circles - Fittschen and co. [16], open stars - Gutman et al. ($[\text{N}_2]$) [12].

One can see that the rate constant of the title reaction shows very weak pressure dependence. In the whole falloff range the rate constant changes less than 1 order of magnitude (e. g. a factor of three at room temperature). The experimental results are associated with significant uncertainty, for this work this is 30 %. There is no reason to believe that the uncertainty of the experiments performed in the falloff range (Refs. [12, 13, 15, 14, 16]) is much smaller. Hence it is difficult to obtain reliable data on the pressure dependence of the title reaction based only on experimental results. The agreement between these and the analysis performed with the experimentally determined structure and enthalpy parameters is pleasing. The obtained falloff curves are further parametrized with the formalism described in Sec. 4.2.4. The fitting of all four parameters ($k_{6,f}^\infty, k_{6,f}^0, k_{6,D}^0, F_c$) is associated with great uncertainty. Hence the values of $k_{6,f}^\infty$ and $k_{6,D}^0$ obtained from the Master Equation analysis have been adopted for the fit with Eq. 4.20. $k_{6,f}^0$ and F_c have been adjusted to the results from the Master Equation analysis. The results from this study, as well as comparison with literature data are presented in Tab. 6.4.

Table 6.4: Parameters for simulation of the falloff behavior of R 6 with Eq. 4.20.

Literature	T / K	$k_{6,f}^\infty / 10^{-13}$ cm ³ s ⁻¹	$k_{6,f}^0 / 10^{-32}$ cm ⁶ s ⁻¹	$k_{6,D}^0 / 10^{-14}$ cm ³ s ⁻¹	F_c
This work	298	3.0	22.5	10.4	0.67
Ref. [13]	298	2.6	200		0.60
Ref. [15]	298	1.9	160		0.50
This work	375	4.0	13.4	9.2	0.60
This work	433	4.9	9.5	8.4	0.54
This work	473	5.7	6.8	8.0	0.52

The temperature dependence each of the parameters listed in Tab. 6.4 will be discussed below.

6.4.2.1 The High Pressure Range

As seen from the falloff curves presented above, the high-pressure rate constant shows a weak positive temperature dependence. In order to represent the experimental results in the falloff range with a reaction barrier of about 1 kJ / mol it was necessary to adjust the vibrational frequencies calculated *ab initio* (from Ref. [16]), as discussed above. The correction introduces additional looseness in the entrance transition state and hence increases the re - dissociation rate constant and decreases the low pressure rate constant for R 6. More discussions on this topic are given in Ref. [16]. The results from the Master Equation calculations are presented in Fig. 6.12.

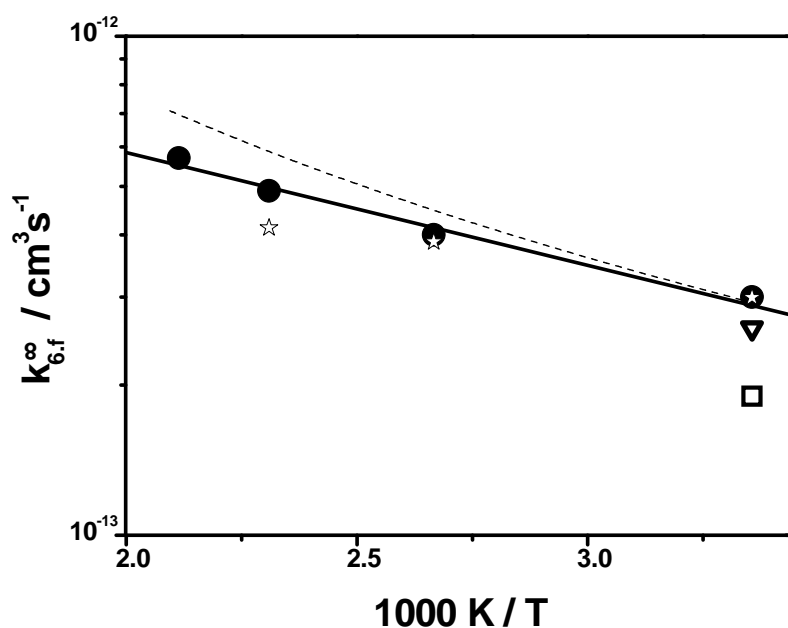


Figure 6.12: Temperature dependence of the high-pressure rate constant for the recombination of CH_2CHO and O_2 . The symbols are respectively: filled circles - results from the Master Equation (ME) analysis, open stars - mean value of the experiments from this work, open triangle Ref. [13], open square Ref. [15]. The solid line is a linear fit of the results from the Master Equation analysis (Eq. 4.8), the dashed line - TST calculation.

The mean values from the measurements on the recombination performed in this work are presented in Fig. 6.12. At low temperatures (298 - 375 K), the measurements were performed in the high-pressure limit. Increasing the temperature causes a shift of the falloff transition regions to higher pressures. Hence some of the measurements were done close to the high-pressure limit, as seen from the lower values of the rate constant at 433 K. At 473 K most of the measurements are performed in the falloff range and are not shown in Fig. 6.12.

A transition state calculation (Eq. 4.9) with the parameters obtained from the ME analysis is presented in Fig. 6.12 as well. The Master Equation analysis is performed for $J = 44$, which is the mean J for O₂CH₂CHO at room temperature, so some deviations between this and the TST calculations are observed at higher temperatures. The reason is that the rotational contributions to the rate constant in the Master Equation analysis are underestimated, but the results are consistent within 30 %.

The values of $k_{6,f}^{\infty}$ are listed in Table 6.4, and the parameters for the analysis are given in the appendix. A linear fit of the results from the Master Equation analysis [16] yields the following expression for the recombination rate constant:

$$k_{6,f}^{\infty} = k_{6.1} = 1.7 \times 10^{-12} \exp\left(-\frac{4.3 \text{ kJ/mol}}{RT}\right) \frac{\text{cm}^3}{\text{s}} \quad (6.16)$$

The positive temperature dependence of $k_{6.1}$ is associated with the small barrier at the entrance channel, which is a consequence of the loss of resonance stabilization of CH₂CHO by the recombination.

The complex forming mechanism of R 6 has no impact on its high-pressure rate coefficient. In this limit the rate constant does not depend on the collision partner, so a comparison with literature data is presented in Fig. 6.16 as well. The results from this work at 298 K are consistent with the ones from Ref. [13]. The data reported from Ref. [15] are about 40 % lower than the ones obtained in this work. The reasons for the disagreement are not clear, but these still agree within the combined experimental uncertainty.

6.4.2.2 The Low Pressure Range

The kinetics of the title reaction in this limit is governed by the *low pressure (fragmentation) rate constant* ($k_{6,D}^0$). This can be presented as a product of the maximal (high-pressure) association rate constant $k_{6,1}$ (see Eq. 4.19), and a yield factor Y , which depends on the branching ratio between the product formation and re-dissociation [94]:

$$k_{6,D}^0 = \frac{k_{6,1}k_{6,3}}{k_{6,2} + k_{6,3}} = k_{6,1} \frac{1}{\frac{k_{6,2}}{k_{6,3}} + 1} = k_{6,1}Y \quad (6.17)$$

The temperature dependence of $k_{6,1}$ has already been discussed above. The theoretical analysis performed in Ref. [92] allows for a determination of the yield factor Y as well. This requires information on the energy dependence of the kinetics of the complex along the isomerization and re-dissociation channels. The results on this obtained by Ref. [92] are presented in Fig. 6.13.

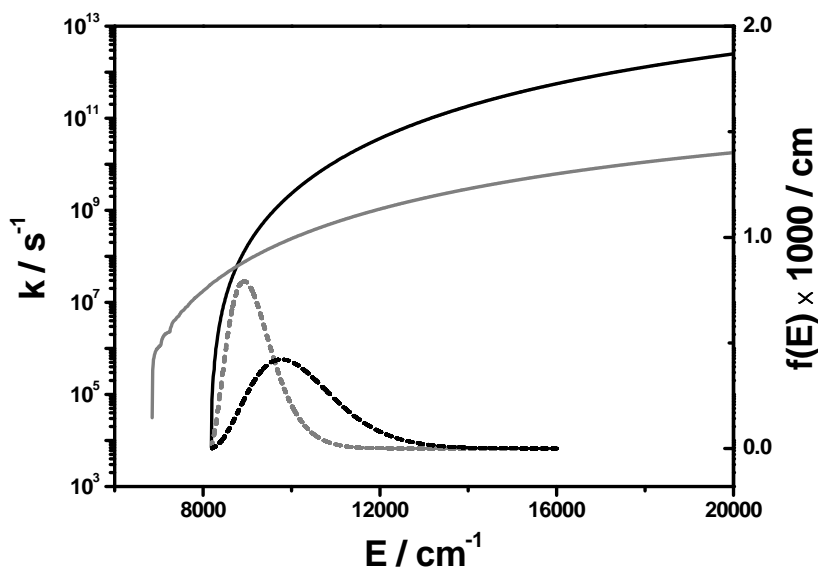


Figure 6.13: Energy dependence of the specific rate constants from Ref. [92] for the re-dissociation (black solid curve) and isomerization (gray solid curve). The dashed lines represent the initial population for 298 K (gray dashed curve) and 473 K (black dashed curve).

As seen from Fig. 6.13, vibrational channel switching [20] is observed at about 8700 cm^{-1} . Since the energy dependence of the density of states for the two channels is equal, the results show that the number of open channels at the entrance increases with energy faster than the one at the exit. The population distribution, obtained by the chemical activation is presented in Fig. 6.13 as well. According to this, the domination of the re-dissociation channel (and hence the ratio $k_{6,2}/k_{6,3}$) increases with the temperature, since the population distribution shifts to higher energies. Hence the falloff curves at high temperatures became closer to those by simple recombination reactions.

The exact results from Ref. [92] yield $Y(298\text{ K}) = 0.345$ and $Y(473\text{ K}) = 0.141$. This corresponds (see Eq. 6.17) to a branching ratio $k_{6,2}/k_{6,3}$ of ≈ 2 at 298 K and ≈ 6 at 473 K. Considering the slightly increasing with temperature $k_{6,1}$ one can see that the ratio re-dissociation / isomerization ($k_{6,2}/k_{6,3}$) compensates this effect and introduces even negative temperature dependence of $k_{6,D}^0$, shown in Fig. 6.14.

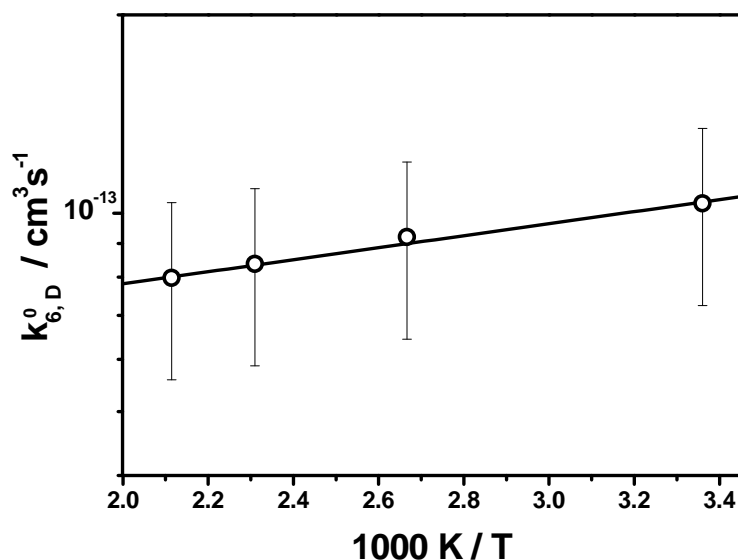


Figure 6.14: The temperature dependence of the low pressure rate constant $k_{6,D}^0$, obtained from Ref. [16].

The temperature dependence of the low pressure rate constant of R 6 can be described by the following expression:

$$k_{6,D}^0 = k_6^0 = 5.14 \times 10^{-14} \exp\left(\frac{210\text{K}}{T}\right) \frac{\text{cm}^3}{\text{s}} \quad (6.18)$$

In this limit the reaction rate is determined from the competition between individual reaction channels. Hence from the extracted expressions no interpretation on the thermodynamical properties (activation energies, entropy contributions etc.) of the rate constants are made.

6.4.2.3 The Low Pressure Addition Rate Constant

The *low pressure addition rate constant* is given by the product of the high-pressure association rate constant and the ratio between the stabilization and reaction processes:

$$k_{6,f}^0 = k_{6.1} \frac{k_{6.4}[M]}{k_{6.2} + k_{6.3}} \quad (6.19)$$

$k_{6,f}^0$ decreases with temperature, since at higher temperatures the complex formed possesses more energy, hence its lifetime is shorter. The negative T- dependence introduced by the faster reaction processes (the denominator in Eq. 6.19) compensates the increasing with temperature $k_{6.1}$. At the same time, the shorter lifetime of the complex shifts the transition between the limiting- and the falloff- ranges to higher pressures.

Information on the temperature dependence of $k_{6,f}^0$ has been extracted from the parametrization of the results obtained by the Master Equation analysis [16] with Eq. 4.20. The results are graphically presented in Fig. 6.15. The temperature dependence of $k_{6,f}^0$ can be described by Eq. 6.20:

$$k_{6,f}^0 = 1.0 \times 10^{-32} \exp\left(\frac{923\text{K}}{T}\right) \frac{\text{cm}^6}{\text{s}} \quad (6.20)$$

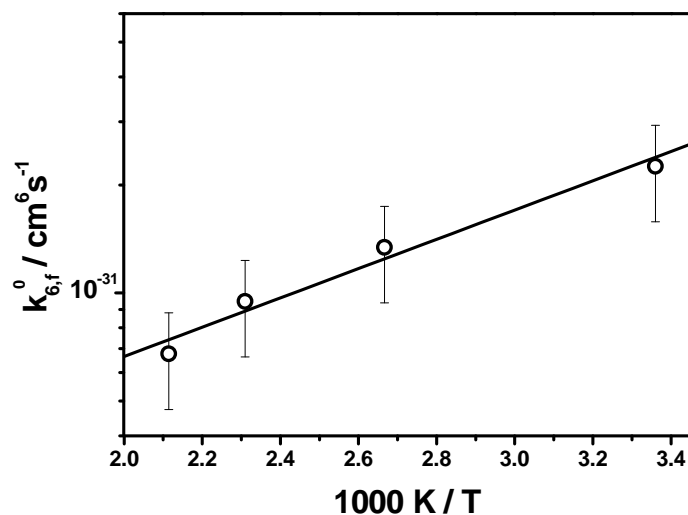


Figure 6.15: The temperature dependence of the low pressure recombination rate constant. The open symbols are results from the parametrization of the results from the ME [16] with Eq. 4.20, the solid line - linear fit of these.

Comparison of the literature data to the results from this work is given in Table 6.4. For the data evaluation in previous studies on the title reaction [13, 15] a simple recombination mechanism has been adopted. This ignores the contributions of the direct reaction channel at lower pressures, where these could be significant. Hence the discrepancies between the literature data and the results from this work, which are nearly a factor of 10, are not unexpected.

6.4.2.4 The Broadening Factor

The broadening of the falloff curves depends on the energy transfer processes, which influence the branching ratio between the competing reaction and stabilization processes. In general at higher temperatures the lifetime of the complex is shorter, i. e. the reaction processes are faster. The temperature dependence of the stabilization rate constant is positive as well. In this work the broadening factor, which determines the pressure dependence of the rate constant, has been treated as a fit parameter, so no further discussion on its detailed temperature dependence are made. The parametrization of the results from the Master Equation analysis with

Eq. 4.20 yields the temperature dependence of the broadening factor presented in Fig. 6.16.

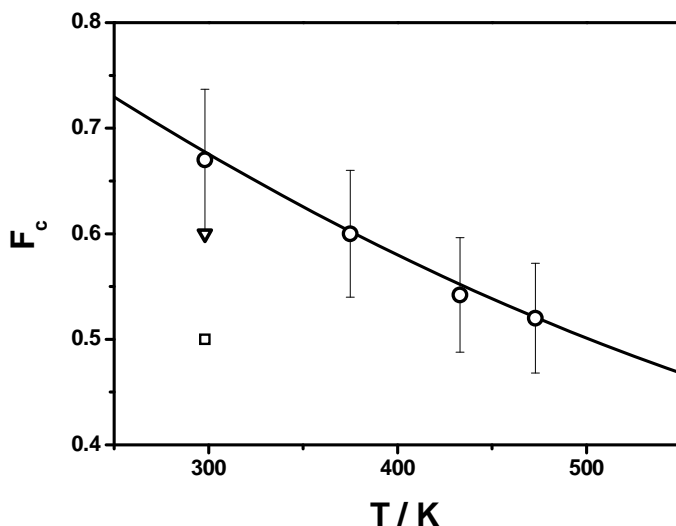


Figure 6.16: The temperature dependence of the broadening factor for reaction 6. The symbols are respectively: open circles - this work, open triangle Ref. [13], open square Ref. [15]. The solid line is a fit of the results from this work with Eq. 6.21.

In general the broadening factor shows negative temperature dependence at lower temperatures, and increases finally at high temperatures. Some expressions which account for this effect are purposed in Ref. [36]. In order to represent the broadening factor (which accounts for the weak collision effects as well) obtained in this work, a two parameters fit function was sufficient. The temperature dependence of F_c is given with the following expression:

$$F_c = \exp\left(-\frac{T}{730 \text{ K}}\right) + \exp\left(-\frac{3000 \text{ K}}{T}\right) \quad (6.21)$$

The deviations between the results from this work and the literature data [13, 15] are caused by the simple addition mechanism adopted in previous studies, as well as the narrow experimental range in these.

6.5 Conclusions

The results from this work confirm that the recombination of CH₂CHO with O₂ proceeds via a complex formation. Reliable data on the reaction kinetics have been obtained by a comparison of experimental results in broad temperature and pressure ranges with *ab initio* calculations and detailed kinetics modeling.

Based on experiments performed in the high-pressure range, information on the reaction channel barriers can be won with relatively simple (e. g. TST) theoretical models. The parameters needed for the TST analysis are obtained from *ab initio* calculations performed in Ref. [16].

The investigations at low temperatures yielded a reaction barrier for the recombination of about 1 kJ / mol. In order to reproduce the experimental results in the falloff range, slight modification of the vibrational frequencies calculated *ab initio* (see Sec. 7.6) was necessary [16].

At higher temperatures the adduct became thermally unstable. The investigations showed that in this temperature range the re - dissociation channel opens, due to which relaxation of the [CH₂CHO] in equilibrium was observed. Third law analysis of the extracted equilibrium constants yielded a reaction enthalpy of $\Delta H_R^{\theta}(0K) = 97$ kJ/mol. The entropy contributions to the equilibrium constant were calculated from *ab initio* structures and frequencies [16], no modifications of these were needed.

Information on the barrier height of the exit channel has been extracted at still higher temperatures. This has been determined to be 82 kJ / mol at 0 K.

In spite of the smaller enthalpy barrier for the isomerization, the re-dissociation is favored at lower temperatures. This results from the significant entropy contributions to $k_{6,2}$, due to the "looser" transition state. The parameters used for the analysis are listed in the appendix.

The potential energy surface, with the rate determining barriers, obtained by the high-pressure experimental data is presented in Fig. 6.17. The further reaction channel barriers, calculated on a CCSD(T)/cc-pVDZ // QCISD/6-311G(d,p) [95,16] are presented as well, in order to show that these channels are insignificant under the experimental conditions in this work.

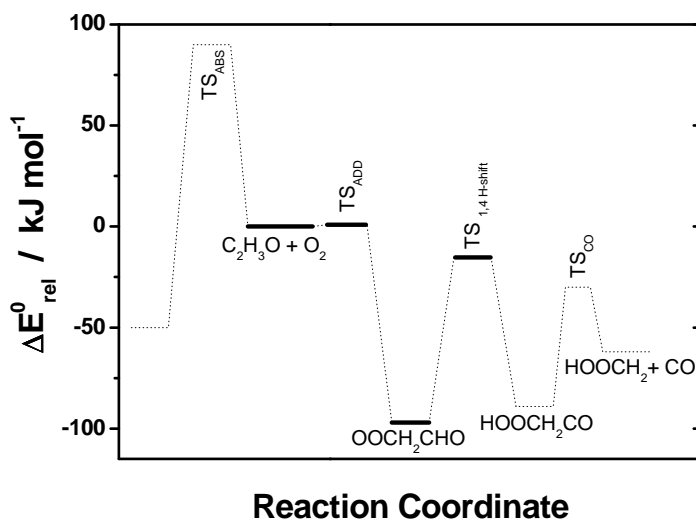


Figure 6.17: Potential energy surface of the vinoxy oxidation. The solid lines represent the experimentally determined barriers, the dashed - the results from the calculations, performed by B. Viskolcz [95].

In Fig. 6.17 the reaction barriers (relatively to the vinoxy + O₂ level) at 0 K are plotted against the reaction coordinate. The barrier heights determined in this work are presented with solid black lines. The barriers determined in this work for the respective reaction channels relatively to the reactants level are listed below:

R 6.1	$\Delta E_{rel}(0 \text{ K}) = 1 \text{ kJ / mol}$
R 6.2	$\Delta E_{rel}(0 \text{ K}) = 98 \text{ kJ / mol}$
R 6.3	$\Delta E_{rel}(0 \text{ K}) = 82 \text{ kJ / mol}$

Parametrization of the results obtained from the Master Equation analysis with the formalism presented in Sec. 4.2.4 allows reliable extrapolation of the rate constant of R 6. For the temperature range 298 - 470 K the falloff curves can be simulated with Eq. 4.20 and the following parameters:

$$k_{6,f}^{\infty} = k_{6.1} = 1.7 \times 10^{-12} \exp\left(-\frac{4.3 \text{ kJ/mol}}{RT}\right) \frac{\text{cm}^3}{\text{s}} \quad (6.22)$$

$$k_{6,f}^0 = 1.0 \times 10^{-32} \exp\left(\frac{923\text{K}}{T}\right) \frac{\text{cm}^6}{\text{s}} \quad (6.23)$$

$$k_{6,D}^0 = k_6^0 = 5.14 \times 10^{-14} \exp\left(\frac{210\text{K}}{T}\right) \frac{\text{cm}^3}{\text{s}} \quad (6.24)$$

$$F_c = \exp\left(-\frac{T}{730\text{K}}\right) + \exp\left(-\frac{3000\text{K}}{T}\right) \quad (6.25)$$

The obtained parameters are recommended for atmospheric and combustion modeling. The falloff curves of R 6 at different temperatures, simulated with Eq. 4.20 and the parameters listed above, are presented in Fig. 6.18.

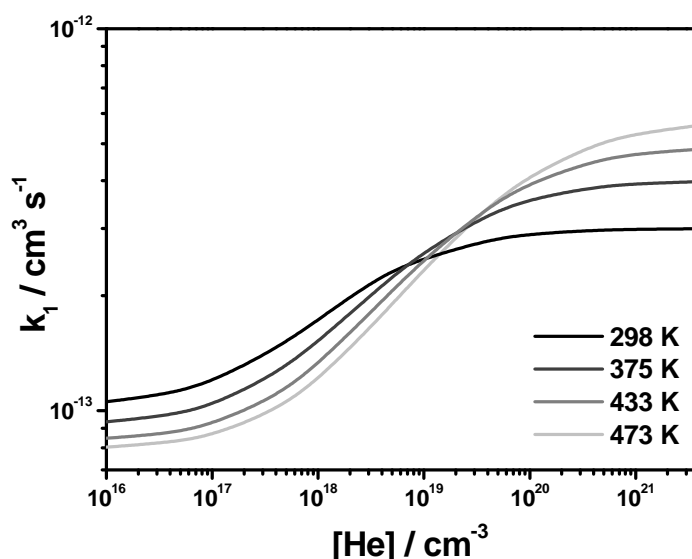


Figure 6.18: Falloff curves at different temperatures, simulated with Eq. 4.20 with the parameters from the equations given above.

The results from this work show that at atmospheric relevant pressures the rate constant shows very weak temperature and pressure dependence.

The investigation on the recombination of vinoxy radicals with oxygen reveal the complexity of the reaction kinetics. The rate constant of the title reaction in wide experimental range, combined with accurate theoretical modeling yielded reliable data on the title reaction. The simple analytical expressions presented above can be directly used for atmosphere and combustion modeling.

Chapter 7

Appendix

7.1 Experimental Results for the HCO Decomposition

Table. 7.1 Experimental results for the HCO decomposition in He at 590 K.

T / K	$p(\text{He})/\text{bar}$	$p(\text{CH}_3\text{CHO})/\text{mbar}$	$k_{\text{uni}}/10^4 \text{ s}^{-1}$	N_{exp}
590	17.3	0.4	2.2	3
590	19.5	0.2	2.2	3
590	25.0	0.2	3.0	3
590	32.0	0.3	3.7	3
590	32.5	0.7	3.0	3
590	33.1	0.7	3.7	3
590	43.2	0.4	4.2	3
590	45.0	0.9	4.5	3
590	53.4	0.4	5.1	3
590	53.5	1.1	4.8	3
590	61.5	0.5	6.4	3
590	67.3	1.4	6.7	3
590	73.0	1.5	6.1	3
590	73.2	0.6	6.7	3
590	81.6	1.7	8.4	3
590	84.7	0.7	9.0	3

T / K	$p(\text{He})/\text{bar}$	$p(\text{CH}_3\text{CHO})/\text{mbar}$	$k_{\text{uni}}/10^4 \text{ s}^{-1}$	N_{exp}
590	92.7	1.9	9.6	3
590	93.0	1.9	9.3	3
590	97.1	0.8	9.3	3
590	102.2	2.1	10.8	2
590	107.0	0.9	9.8	3
590	113.6	2.3	11.8	3
590	115.7	1.0	9.7	3
590	119.0	2.5	9.1	3
590	123.0	1.0	10.6	3
590	123.0	2.5	12.6	3
590	132.6	1.1	10.7	3
590	139.2	1.2	10.3	3
590	230.0	3.0	17.1	1

Table. 7.2. Experimental results for the HCO decomposition in He at 643 K.

T / K	$p(\text{He})/\text{bar}$	$p(\text{CH}_3\text{CHO})/\text{mbar}$	$k_{\text{uni}}/10^4 \text{ s}^{-1}$	N_{exp}
643	1.1	0.2	1.1	3
643	1.9	0.2	1.7	3
643	3.6	0.4	1.7	3
643	3.7	0.3	2.5	3
643	5.9	0.8	3.6	3
643	6.1	0.5	3.6	3
643	6.4	0.2	3.5	3
643	7.0	0.8	2.8	2
643	9.7	1.4	5.4	3
643	10.2	0.3	5.1	3
643	10.5	0.9	5.7	3
643	13.0	0.4	5.0	3
643	13.6	1.9	7.2	3
643	14.3	0.4	5.9	3
643	17.3	1.5	8.6	3
643	17.5	2.5	9.4	3
643	19.6	0.5	7.1	3
643	20.4	0.7	5.9	3

T/K	$p(\text{He})/\text{bar}$	$p(\text{CH}_3\text{CHO})/\text{mbar}$	$k_{\text{uni}}/10^4 \text{ s}^{-1}$	N_{exp}
643	28.1	2.5	13.1	3
643	28.5	0.8	10.7	3
643	31.2	1.1	10.5	3
643	36.9	0.9	13.0	3
643	37.3	3.3	15.3	3
643	45.2	1.5	13.9	3
643	46.1	1.2	15.6	2
643	50.7	1.3	17.1	3
643	56.6	1.5	16.8	3
643	57.3	1.9	16.8	4
643	64.0	1.7	21.5	3
643	69.0	2.3	18.7	4
643	76.7	2.0	21.5	3
643	82.5	2.7	19.8	4
643	87.5	2.3	22.9	3
643	95.7	2.5	26.0	3
643	102.0	3.4	24.6	7
643	104.2	2.8	25.0	3
643	113.5	3.0	28.2	3
643	130.0	3.0	28.2	3
643	153.0	2.0	34.3	3

Table. 7.3. Experimental results for the HCO decomposition in He at 700 K.

T / K	$p(\text{He})/\text{bar}$	$p(\text{CH}_3\text{CHO})/\text{mbar}$	$k_{\text{uni}}/10^4 \text{ s}^{-1}$	N_{exp}
700	1.5	0.7	2.8	3
700	1.8	0.3	4.0	3
700	2.7	0.1	4.4	3
700	2.7	0.5	4.9	3
700	3.1	0.2	4.3	3
700	3.4	0.6	6.4	3
700	6.0	0.4	6.9	3
700	6.0	0.4	8.1	3
700	6.0	1.0	9.6	3
700	6.7	0.3	8.4	3

T/K	$p(\text{He})/\text{bar}$	$p(\text{CH}_3\text{CHO})/\text{mbar}$	$k_{\text{uni}}/10^4 \text{ s}^{-1}$	N_{exp}
700	7.4	0.8	10.0	3
700	8.0	1.4	12.2	3
700	8.9	1.6	9.3	1
700	9.0	1.6	10.8	1
700	9.7	1.7	13.6	3
700	9.8	1.8	11.9	3
700	10.1	0.8	9.6	3
700	10.4	0.8	10.0	3
700	10.6	1.9	12.3	3
700	10.8	0.8	12.8	3
700	11.0	0.7	14.6	3
700	11.0	0.5	14.4	3
700	11.2	0.2	10.0	3
700	11.2	2.0	11.4	3
700	11.2	0.5	14.0	3
700	11.4	0.2	10.8	3
700	12.1	0.9	11.0	3
700	13.5	1.0	13.3	8
700	14.0	0.5	19.1	3
700	14.0	1.0	13.7	3
700	14.6	1.0	19.2	3
700	15.1	0.7	19.9	3
700	16.6	0.7	20.2	4
700	18.9	1.3	20.9	3
700	19.3	0.9	20.6	3
700	22.5	1.5	23.3	3
700	23.0	1.7	22.6	3
700	25.1	1.2	24.2	3
700	25.2	1.2	23.9	6
700	25.5	1.8	23.5	3
700	29.6	2.2	23.7	3
700	29.9	1.5	26.2	3
700	31.1	0.5	22.0	3
700	32.9	1.6	27.7	3

T/K	$p(\text{He})/\text{bar}$	$p(\text{CH}_3\text{CHO})/\text{mbar}$	$k_{\text{uni}}/10^4 \text{ s}^{-1}$	N_{exp}
700	45.4	0.8	36.0	3
700	53.4	0.9	44.4	3
700	61.4	1.0	44.5	3
700	68.1	1.1	51.7	3
700	77.3	1.3	53.0	3
700	88.1	1.5	84.5	3
700	91.3	1.5	45.8	3

Table. 7.4. Experimental results for the HCO decomposition in He at 752 K.

T / K	$p(\text{He})/\text{bar}$	$p(\text{CH}_3\text{CHO})/\text{mbar}$	$k_{\text{uni}}/10^4 \text{ s}^{-1}$	N_{exp}
752	1.1	0.2	3.7	3
752	1.7	0.3	5.0	4
752	2.7	0.6	7.8	3
752	3.1	0.9	7.7	3
752	3.8	0.9	10.8	3
752	4.9	0.3	11.3	3
752	5.2	0.3	13.6	3
752	5.9	1.2	16.8	3
752	7.5	1.5	21.0	3
752	9.4	0.7	26.2	3
752	9.7	1.9	24.2	3
752	10.9	0.5	25.8	3
752	15.7	0.8	38.8	3
752	16.4	1.1	38.5	3
752	17.2	1.0	40.9	3
752	20.4	1.0	43.0	3
752	20.9	1.5	43.2	3
752	23.6	1.6	47.4	3
752	29.0	1.5	59.5	3
752	36.4	1.8	74.5	4
752	46.3	2.3	80.8	3

Table. 7.5. Experimental results for the HCO decomposition in He at 800 K.

T / K	$p(\text{He})/\text{bar}$	$p(\text{CH}_3\text{CHO})/\text{mbar}$	$k_{\text{uni}}/10^4 \text{ s}^{-1}$	N_{exp}
800	1.1	0.5	7.2	3
800	1.6	0.2	9.8	3
800	1.9	0.8	10.5	3
800	2.2	0.2	12.8	3
800	2.6	1.1	11.9	3
800	3.1	0.3	16.4	3
800	3.5	0.6	17.3	3
800	3.8	1.6	19.4	3
800	3.9	0.4	21.8	3
800	5.0	0.4	21.1	4
800	5.1	0.6	25.0	3
800	5.9	1.0	24.7	3
800	6.5	2.5	29.7	3
800	7.0	0.8	33.5	3
800	8.0	0.8	31.1	3
800	9.9	1.1	39.5	3
800	12.7	1.4	53.1	3
800	13.0	1.2	42.0	4
800	18.5	2.1	88.0	3
800	22.0	2.1	83.3	3
800	22.2	2.5	89.0	3
800	25.8	1.4	153.7	3
800	33.0	1.8	182.6	3
800	38.7	2.1	182.0	2
800	44.6	1.0	196.9	3
800	47.1	2.5	182.0	3
800	48.1	2.4	218.0	3
800	51.1	1.2	199.5	3
800	59.3	1.4	271.2	3
800	66.5	1.6	340.2	3
800	70.7	1.2	309.2	3
800	72.7	1.7	397.7	3
800	81.3	1.9	304.0	3

T/K	$p(\text{He})/\text{bar}$	$p(\text{CH}_3\text{CHO})/\text{mbar}$	$k_{\text{uni}}/10^4 \text{ s}^{-1}$	N_{exp}
800	89.2	2.1	386.8	3
800	90.2	1.5	279.7	3
800	98.3	2.3	419.2	2
800	108.5	2.5	456.0	3
800	115.4	2.7	495.1	3
800	124.1	2.9	457.3	3

Table 7.6. Experimental results for the HCO decomposition in Ar at 643 K.

T / K	$p(\text{Ar})/\text{bar}$	$p(\text{CH}_3\text{CHO})/\text{mbar}$	$k_{\text{uni}}/10^4 \text{ s}^{-1}$	N_{exp}
643	5.3	0.2	2.0	3
643	7.8	0.3	2.7	8
643	9.7	0.4	3.6	3
643	14.1	0.6	4.4	3
643	18.4	0.8	5.9	6
643	24.3	1.0	8.2	3
643	30.3	1.3	9.3	5
643	35.9	1.5	10.8	4
643	42.2	1.8	12.2	6
643	49.4	2.0	11.3	5
643	55.2	2.3	11.4	5

Table 7.7. Experimental results for the HCO decomposition in N_2 at 546 K.

T / K	$p(\text{N}_2)/\text{bar}$	$p(\text{CH}_3\text{CHO})/\text{mbar}$	$k_{\text{uni}}/10^4 \text{ s}^{-1}$	N_{exp}
546	75.9	2.4	2.2	3
546	76.0	2.4	2.3	3
546	76.3	2.4	2.3	3

Table 7.8. Experimental results for the HCO decomposition in N_2 at 593 K.

T/K	$p(\text{N}_2)/\text{bar}$	$p(\text{CH}_3\text{CHO})/\text{mbar}$	$k_{\text{uni}}/10^4 \text{ s}^{-1}$	N_{exp}
593	17.0	0.5	2.2	3
593	22.3	0.7	2.3	2
593	30.7	1.0	3.4	4
593	38.5	1.2	3.8	3

T/K	$p(\text{N}_2)/\text{bar}$	$p(\text{CH}_3\text{CHO})/\text{mbar}$	$k_{\text{uni}}/10^4 \text{ s}^{-1}$	N_{exp}
593	45.6	1.4	3.8	3
593	54.9	1.7	5.2	3
593	64.4	2.0	4.5	4
593	70.6	2.2	5.5	4

Table 7.9. Experimental results for the HCO decomposition in N_2 at 643 K.

T/K	$p(\text{N}_2)/\text{bar}$	$p(\text{CH}_3\text{CHO})/\text{mbar}$	$k_{\text{uni}}/10^4 \text{ s}^{-1}$	N_{exp}
643	1.2	0.1	0.9	3
643	1.3	0.1	0.9	3
643	1.7	0.1	1.1	3
643	1.8	0.1	1.0	3
643	1.9	0.1	1.0	3
643	2.1	0.2	1.5	4
643	2.5	0.1	1.1	3
643	3.2	0.1	1.2	3
643	3.3	0.2	1.8	3
643	4.0	0.2	1.6	3
643	4.6	0.2	2.1	3
643	5.8	0.3	2.5	2
643	6.1	0.3	2.0	3
643	6.3	0.3	2.2	3
643	7.5	0.4	2.7	2
643	9.1	0.5	3.3	2
643	9.3	0.5	3.5	2
643	9.6	0.5	3.8	4
643	10.4	0.6	4.3	3
643	10.8	0.5	3.7	3
643	12.1	0.6	4.8	3
643	12.1	0.6	5.3	3
643	13.3	0.7	5.1	3
643	13.8	0.7	5.6	2
643	14.6	0.7	6.2	3
643	14.8	0.8	6.2	3
643	15.5	0.7	4.8	3

T/K	$p(\text{N}_2)/\text{bar}$	$p(\text{CH}_3\text{CHO})/\text{mbar}$	$k_{\text{uni}}/10^4 \text{ s}^{-1}$	N_{exp}
643	17.7	0.9	7.0	3
643	22.7	1.0	7.4	3
643	23.8	1.2	9.6	3
643	24.8	1.2	8.0	3
643	30.3	1.3	9.9	4
643	32.5	1.5	11.0	3
643	37.2	1.7	11.9	3
643	39.6	1.7	11.0	3
643	45.1	2.1	14.0	3
643	45.8	2.0	12.9	4
643	55.4	2.6	18.0	4
643	63.7	3.0	19.8	4
643	74.0	3.5	25.1	4
643	82.7	3.9	28.6	4

Table 7.10. Experimental results for the HCO decomposition in N_2 at 700 K.

T/K	$p(\text{N}_2)/\text{bar}$	$p(\text{CH}_3\text{CHO})/\text{mbar}$	$k_{\text{uni}}/10^4 \text{ s}^{-1}$	N_{exp}
700	1.3	0.1	1.3	3
700	1.4	0.1	1.8	4
700	1.4	0.1	2.3	3
700	1.4	0.2	1.7	3
700	1.6	0.1	1.6	3
700	1.9	0.1	2.3	3
700	2.2	0.2	2.4	3
700	2.6	0.2	2.5	3
700	2.7	0.4	2.8	2
700	2.9	0.2	2.8	4
700	3.0	0.3	2.7	3
700	3.3	0.3	4.3	4
700	3.7	0.3	3.6	3
700	3.8	0.3	5.2	4
700	3.8	0.3	3.7	3
700	4.0	0.6	4.7	3
700	4.5	0.3	5.0	3

T/K	$p(\text{N}_2)/\text{bar}$	$p(\text{CH}_3\text{CHO})/\text{mbar}$	$k_{\text{uni}}/10^4 \text{ s}^{-1}$	N_{exp}
700	4.8	0.4	5.3	4
700	5.0	0.4	5.3	4
700	5.1	0.4	4.8	3
700	5.6	0.5	5.7	3
700	5.8	0.5	5.5	2
700	5.8	0.5	7.0	3
700	5.8	0.9	7.6	4
700	6.0	0.3	6.2	3
700	6.3	0.5	6.7	3
700	6.3	0.5	7.0	3
700	6.9	0.4	7.1	5
700	7.0	0.6	7.8	4
700	7.4	0.5	7.7	4
700	7.7	0.6	6.7	3
700	8.1	0.7	8.8	4
700	8.5	0.6	7.8	3
700	8.7	0.7	9.9	3
700	9.0	0.8	10.6	3
700	9.5	0.7	8.6	3
700	9.9	1.5	11.5	3
700	10.3	0.9	9.4	5

7.2 Parameters for Analysis of the HCO Decomposition

$$\text{Reaction Enthalpy / cm}^{-1}: \quad \Delta H^0_r(0 \text{ K}) = 5001 \quad [46]$$

$$\text{Threshold Energy / cm}^{-1}: \quad E_0 = 6009 \quad [46]$$

HCO:

$$\text{Frequencies / cm}^{-1}: \quad \nu = 1081, 1868, 2435 \quad [46]$$

$$\text{Moments of Inertia / amu. \AA}^2: \quad I = 0.71, 11.61, 12.32 \quad [6]$$

$$\text{Electronic Partition Function:} \quad Q_{el} = 2$$

HCO[≠] :

$$\text{Frequencies / cm}^{-1}: \quad \nu = 400, 2120, 589i \quad [6]$$

$$\text{Moments of Inertia / amu. \AA}^2: \quad I = 2.01, 11.96, 13.97 \quad [6]$$

$$\text{Electronic Partition Function:} \quad Q_{el} = 2$$

Lennard - Jones Parameters:

$$\text{He} \quad \sigma_{LJ} = 2.55 \cdot 10^{-10} \text{ m} \quad [96]$$

$$\text{He} \quad \varepsilon_{LJ}/\text{K} = 10 \text{ K} \quad [96]$$

$$\text{Ar} \quad \sigma_{LJ} = 3.47 \cdot 10^{-10} \text{ m} \quad [96]$$

$$\text{Ar} \quad \varepsilon_{LJ}/\text{K} = 114 \text{ K} \quad [96]$$

$$\text{N}_2 \quad \sigma_{LJ} = 3.9 \cdot 10^{-10} \text{ m} \quad [96]$$

$$\text{N}_2 \quad \varepsilon_{LJ}/\text{K} = 71 \text{ K} \quad [96]$$

$$\text{HCO} \quad \sigma_{LJ} = 3.70 \cdot 10^{-10} \text{ m} \quad [4]$$

7.3 Experimental Results for the DCO Decomposition

Table 7.11. Experimental Results for the DCO decomposition in He at 643 K.

T / K	$p(\text{He})/\text{bar}$	$p(\text{CD}_3\text{CDO})/\text{mbar}$	$k_{\text{uni}}/10^4 \text{ s}^{-1}$	N_{exp}
643	2.9	0.1	0.5	3
643	3.2	0.1	0.6	3
643	5.0	0.1	0.9	3
643	8.8	0.2	1.4	3
643	17.4	0.4	2.8	3
643	27.5	0.7	3.6	3
643	41.0	1.0	6.3	3
643	53.0	1.4	7.7	3
643	54.8	2.8	8.0	3
643	64.6	1.3	9.3	3
643	66.2	1.7	8.4	3
643	108.0	2.5	15.3	3
643	119.0	3.8	12.8	3
643	128.0	3.0	16.6	3
643	173.0	3.5	17.3	3

Table 7.12. Experimental results for the DCO decomposition in He at 700 K.

T / K	$p(\text{He})/\text{bar}$	$p(\text{CD}_3\text{CDO})/\text{mbar}$	$k_{\text{uni}}/10^4 \text{ s}^{-1}$	N_{exp}
700	1.5	0.2	1.3	3
700	1.7	0.1	1.1	3
700	2.9	0.4	1.9	3
700	3.2	0.1	1.8	4
700	5.0	0.2	2.8	3
700	5.0	0.7	3.0	3
700	7.7	0.3	3.8	3
700	8.0	1.2	4.6	3
700	10.6	1.8	6.2	3
700	12.2	0.6	6.2	3
700	12.3	1.8	6.9	3
700	15.9	2.3	8.3	3
700	19.0	2.8	10.9	3

T/K	$p(\text{He})/\text{bar}$	$p(\text{CD}_3\text{CDO})/\text{mbar}$	$k_{\text{uni}}/10^4 \text{ s}^{-1}$	N_{exp}
700	19.1	0.8	7.3	3
700	24.4	0.8	11.9	3
700	27.7	1.2	11.9	4
700	30.9	1.4	12.6	3
700	32.3	1.4	12.8	3
700	33.1	1.1	12.5	3
700	40.6	1.3	13.6	3
700	50.2	1.7	20.4	3
700	53.5	2.8	21.2	3
700	61.1	2.0	22.1	4
700	108.0	3.6	36.6	3
700	172.0	3.4	48.4	3

Table 7.13. Experimental results for the DCO decomposition in He at 750 K.

T / K	$p(\text{He})/\text{bar}$	$p(\text{CD}_3\text{CDO})/\text{mbar}$	$k_{\text{uni}}/10^4 \text{ s}^{-1}$	N_{exp}
750	3.9	0.2	4.0	3
750	6.5	0.4	6.3	3
750	8.6	1.3	9.6	3
750	10.1	1.6	11.4	3
750	10.4	0.6	10.4	3
750	16.1	0.9	14.4	3
750	21.0	1.2	17.3	3
750	26.7	1.5	23.4	3
750	30.6	1.9	25.1	3
750	40.3	1.2	30.4	3
750	42.6	2.5	34.3	3
750	44.6	2.0	38.9	3
750	46.9	1.4	36.6	4
750	52.4	2.3	37.3	4
750	57.5	1.7	37.9	3
750	65.8	2.0	51.2	3
750	76.2	2.3	69.7	3
750	98.6	3.0	68.4	3
750	131.0	4.7	94.5	3
750	161.0	3.2	109.0	3
750	169.4	3.4	107.0	3

Table 7.14. Experimental results for the DCO decomposition in He at 800 K.

T / K	$p(\text{He})/\text{bar}$	$p(\text{CD}_3\text{CDO})/\text{mbar}$	$k_{\text{uni}}/10^4 \text{ s}^{-1}$	N_{exp}
800	2.5	0.1	7.7	1
800	3.0	0.5	7.2	4
800	3.8	0.2	8.6	3
800	5.4	0.8	12.0	3
800	6.7	0.3	13.8	3
800	7.5	0.3	13.3	3
800	8.2	1.2	15.9	3
800	11.7	0.6	32.1	3
800	27.2	1.4	44.6	3
800	34.0	1.7	58.3	2
800	40.4	2.0	70.9	3
800	43.6	1.9	99.7	3
800	99.4	2.0	133.0	2
800	159.0	3.2	267.0	5

7.4 Parameters for Analysis of the DCO Decomposition

Reaction Enthalpy / cm^{-1} :	$\Delta H_r^0(0\text{K}) = 5478$	[55]
Threshold Energy / cm^{-1} :	$E_0 = 6561$	[55]
DCO:		
Frequencies / cm^{-1} :	$\nu = 847, 1795, 1910$	[55]
Moments of Inertia / $\text{amu} \cdot \text{\AA}^2$:	$I = 1.18, 13.50, 14.67$	[6]
Electronic Partition Function:	$Q_{el} = 2$	
DCO ‡ :		
Frequencies / cm^{-1} :	$\nu = 120, 2048, 461i$	[55]
Moments of Inertia / $\text{amu} \cdot \text{\AA}^2$:	$I = 3.00, 15.47, 18.47$	[6]
Electronic Partition Function:	$Q_{el} = 2$	
Lennard - Jones Parameters:	see Sec. 7.2	

The Lennard - Jones Parameters for DCO are estimated to be the same as the ones for HCO (see Sec. 7.2).

7.5 Experimental Results for the Reaction of CH₂CHO and O₂

Table 7.15. Experimental results for the reaction of CH₂CHO and O₂ at 298 K.

$p(\text{He})/\text{bar}$	$[\text{O}_2]/10^{16}\text{cm}^{-3}$	$[\text{He}]/10^{20}\text{cm}^{-3}$	$k_{6.1} / 10^{-13}\text{cm}^3 \text{s}^{-1}$	N_{exp}
3.8	14.8	0.9	3.0	2
14.6	7.9	3.6	3.0	3
15.6	8.4	3.8	2.8	3
16.6	15.9	4.1	2.9	3
22.1	21.3	5.4	2.8	3
25.8	22.6	6.3	3.1	4
26.4	9.8	6.4	3.0	3
30.9	11.5	7.5	2.9	3
43.6	21.6	10.7	3.5	3

Table 7.16. Experimental results for the reaction of CH₂CHO and O₂ at 375 K.

$p(\text{He})/\text{bar}$	$[\text{O}_2]/10^{16}\text{cm}^{-3}$	$[\text{He}]/10^{20}\text{cm}^{-3}$	$k_{6.1} / 10^{-13}\text{cm}^3 \text{s}^{-1}$	N_{exp}
6.6	18.0	1.3	3.8	3
15.6	12.0	3.0	3.9	3
20.2	15.4	3.9	3.5	3
29.1	18.5	5.6	3.6	3
32.5	18.5	6.3	4.2	3
40.3	15.8	7.8	4.1	3
42.7	17.2	8.3	4.0	3

Table 7.17. Experimental results for the reaction of CH₂CHO and O₂ at 433 K.

$p(\text{He})/\text{bar}$	$[\text{O}_2]/10^{16}\text{cm}^{-3}$	$[\text{He}]/10^{20}\text{cm}^{-3}$	$k_{6.1} / 10^{-13}\text{cm}^3 \text{s}^{-1}$	N_{exp}
3.4	7.3	0.6	4.0	3
4.9	5.2	0.8	4.3	3
4.9	4.2	0.8	4.2	3
5.7	6.1	1.0	3.8	3
8.3	5.2	1.4	4.2	3
8.3	8.8	1.4	4.1	3
12.1	7.0	2.1	4.2	3
14.4	8.1	2.4	4.2	3
14.9	9.8	2.5	4.3	3
18.7	4.9	3.1	3.9	3

$p(\text{He})/\text{bar}$	$[\text{O}_2]/10^{16}\text{cm}^{-3}$	$[\text{He}]/10^{20}\text{cm}^{-3}$	$k_{6.1} / 10^{-13}\text{cm}^3 \text{s}^{-1}$	N_{exp}
19.1	12.6	3.2	4.4	3
34.0	17.0	5.7	4.2	3
38.5	13.0	6.4	4.2	3

Table 7.18. Experimental results for the reaction of CH_2CHO and O_2 at 473 K.

$p(\text{He})/\text{bar}$	$[\text{O}_2]/10^{16}\text{cm}^{-3}$	$[\text{He}]/10^{20}\text{cm}^{-3}$	$k_{6.1} / 10^{-13}\text{cm}^3 \text{s}^{-1}$	N_{exp}
2.0	5.6	0.3	3.5	3
3.2	6.3	0.5	3.9	3
5.9	12.7	0.9	4.8	3
7.3	7.0	1.1	4.2	3
7.6	16.3	1.2	3.4	3
11.1	6.5	1.7	4.5	3
11.2	5.8	1.7	4.1	3
18.1	10.9	2.8	4.8	3
19.7	4.7	3.0	4.2	3
46.0	14.6	7.0	4.4	3

Table 7.19. Experimental results for the equilibrium between R 6.1 and R 6.2.

T / K	$p(\text{He}) / \text{bar}$	$[\text{O}_2] / 10^{16}\text{cm}^{-3}$	$k_{6.1} / 10^{-13}\text{cm}^3 \text{s}^{-1}$	K_P / bar^{-1}	N_{exp}
473	2.0	5.6	3.5	2695	3
473	3.2	6.3	3.9	3073	3
473	7.3	7.0	4.2	2667	3
473	11.1	6.5	4.5	2946	3
473	11.2	5.8	4.1	2624	3
484	10.6	6.0	4.4	1841	3
492	39.6	6.0	4.5	1147	3
493	6.9	6.4	4.6	1558	3
494	2.3	6.4	3.7	1170	3
494	4.6	4.2	3.6	1673	3
494	11.1	5.5	4.1	1204	3
494	11.5	6.4	3.4	1042	3
497	10.1	5.6	4.1	1093	2
503	23.8	27.0	4.9	640	3
505	3.3	18.7	3.3	701	3
505	4.5	25.8	3.8	841	3
505	9.8	17.3	4.6	524	3

T / K	$p(\text{He}) / \text{bar}$	$[\text{O}_2] / 10^{16}$	$k_{6.1} / 10^{-13}$	K_P / bar^{-1}	N_{exp}
510	6.5	14.7	3.9	671	3
516	5.4	12.1	3.6	554	3
524	6.1	13.5	3.6	444	3
531.5	9.1	15.3	4.2	290	3
531.5	24.1	26.0	4.6	258	3

Table 7.20. Experimental results for the isomerization of the addition complex.

T / K	p / bar	$[\text{O}_2] / 10^{17} \text{ cm}^{-3}$	$[\text{He}] / 10^{20} \text{ cm}^{-3}$	$K / 10^{-19} \text{ cm}^3$	$k_{6.3} / 10^4 \text{ s}^{-1}$	N_{exp}
572	10.1	1.6	1.3	36.1	2.1	4
572	26.6	2.7	3.4	36.1	1.7	3
581	3.0	1.5	0.4	26.0	2.6	3
581	23.2	2.3	2.9	26.0	2.4	3
581	8.8	1.4	1.1	26.0	3.3	3
597	4.9	2.4	0.6	15.0	3.7	3
597	27.3	2.6	3.3	15.0	3.5	3
599	10.5	1.6	1.3	14.3	4.1	3
611	22.7	2.1	2.7	9.8	6.9	3
613	7.3	1.1	0.9	9.2	9.9	3
615	8.4	1.2	1.0	8.6	8.4	3
616	21.1	2.0	2.5	8.4	8.3	3
618	2.6	1.2	0.3	7.9	9.5	2
620	2.5	1.2	0.3	7.4	10.2	2
631	20.8	1.9	2.4	5.4	12.4	3
633	2.4	1.1	0.3	5.1	14.8	2
652	2.2	1.0	0.2	3.0	25.7	2
652	20.4	1.8	2.3	3.0	22.1	2
654	2.1	0.9	0.2	2.8	26.7	2
660	20.0	1.7	2.2	2.4	27.0	3
660	1.9	0.8	0.2	2.4	30.5	2

7.6 Parameters for Analysis of the Reaction of CH₂CHO and O₂

Table 7.21: Molecular parameters used for the analysis of reaction R 6. The vibrational frequencies and rotational constants have been calculated on the MP2/6-311G/d,p level of theory (see Ref. [16]).

Species	Frequencies / cm ⁻¹	Rot. const. / cm ⁻¹
O ₂ ^a	1580	1.446
CH ₂ CHO	437, 505, 702, 974, 976, 1154, 1419, 1490, 1588, 2996, 3171, 3290	2.225, 0.3786, 0.3235
TS - Addition	54 ^b , 110 ^b , 149 ^b , 286, 524, 588, 719, 992, 1048, 1219, 1375, 1502, 1600, 1700, 3242, 3360, 3473	0.3784, 0.0843, 0.0780
O ₂ CH ₂ CHO	47, 140, 302, 445, 596, 746, 996, 1058, 1116, 1248, 1284, 1359, 1423, 1471, 1790, 3000, 3126, 3200	0.5708, 0.0981, 0.0891
TS - 1,4 H shift	203, 401, 440, 531, 714, 742, 889, 1062, 1149, 1225, 1257, 1277, 1490, 1931, 1994, 3098, 3211	0.5413, 0.1204, 0.1006

^a - data from Ref. [97]

^b - the values were scaled with a factor of 0.55 in order to represent the experimentally observed rate constant

Bibliography

- [1] N. J. B. Green. *Unimolecular Kinetics Part 1. The Reaction Step*. Elsevier Press, King's College London, 2003.
- [2] H. M. Keller; R. Schinke. *J. Chem. Phys.*, 110:9887, 1999.
- [3] R. S. Timonen; E. Ratajczak; D. Gutman; A. F. Wagner. *J. Phys. Chem.*, 91:5325, 1987.
- [4] G. Friedrichs; J. T. Herbon; D. F. Davidson; R. K. Hanson. *Phys. Chem. Chem. Phys.*, 4:5778, 2002.
- [5] L. N. Krasnoperov; E. N. Chesnokov; H. Stark; A. R. Ravishankara. *J. Phys. Chem. A*, 108:11526, 2004.
- [6] A. F. Wagner; J. M. Bowman. *J. Chem. Phys.*, 91:5314, 1987.
- [7] S. W. Cho; A. F. Wagner; B. Gazdy; J. M. Bowman. *J. Phys. Chem.*, 95:9897, 1991.
- [8] J. J. Orlando; G. S. Tyndall; T. J. Wallington. *Chem. Rev.*, 103:4657, 2003.
- [9] M. Olzmann; E. Kraka; R. Cremer; R. Gutbrod; S. Anderson. *J. Phys. Chem. A*, 101:9421, 1997.
- [10] H. Su; R. Bersohn. *Journal of Physical Chemistry A*, 105(40):9178, 2001.
- [11] D. L. Osborn; H. Choi; D. H. Mordant; R. T. Bise; D. M. Neumark; C. M. Rohlfing. *J. Chem. Phys.*, 106(8):3049, 1997.
- [12] D. Gutman; H.H. Nelson. *J. Phys. Chem.*, 87:3902, 1983.

- [13] K. Lorenz; D. Rhasa; R. Zellner; B. Fritz. *Ber. Bunsenges. Phys. Chem.*, 89:341, 1985.
- [14] T. Oguchi; Y. Sato; H. Matsui. *18th International Symposium on Gas Kinetics, Bristol*,, page Poster B13, 2004.
- [15] L. Zhu; G. Johnston. *J. Phys. Chem.*, 99:15114, 1995.
- [16] E. Delbos; C. Fittschen; H. Hippler; N. Krasteva; M. Olzmann; B. Viskolcz. *Submitted*, xx:xxx, 2005.
- [17] A. C. Eckbreth. *Laser Diagnostics for Combustion Temperature and Species*. Abacus Press, Cambridge (MA), 1988.
- [18] R. Forster; M. Frost; D. Fulle; H. F. Hamman; H. Hippler; A. Schleppegrell; J. Troe. *J. Chem. Phys.*, 103:2949, 1995.
- [19] R. Forster. *Rekombinationsreaktionen des Hydroxyl-Radicals bei hohen Drücken: Eine Anwendung des Lasersättigungsspektroskopie*. PhD thesis, Universität Göttingen, 1999.
- [20] H. Hamann. *Kinetik und Dynamic bimolekular komplexbildender Reaktionen des Hydroxyl-Radikals*. PhD thesis, Universität Göttingen, 1995.
- [21] D. Fulle. *Untersuchungen zur Kinetik von Reaktionen des HO- und des CH- Radikals unter Hochdruckbedingungen*. PhD thesis, Georg-August-Universität zu Göttingen, 1996.
- [22] F. Striebel. *Experimentelle Untersuchungen zur Kinetik von Elementarreaktionen unter Hochdruckbedingungen - Ein Beitrag zum Verständnis unimolekularer Reaktionen*. PhD thesis, Universität Karlsruhe, 2000.
- [23] S. Nasterlack. *Bestimmung von Ausbeuten bei komplexbildenden bimolekularen Reaktionen mittels laserinduzierter Fluoreszenz*. PhD thesis, Universität Karlsruhe, 2004.
- [24] H. Hippler; S. Nasterlack; F. Striebel. *Phys. Chem. Chem. Phys.*, 4(13):2959, 2002.

- [25] M. J. Pilling; I. W. M. Smith. *Modern Gas Kinetics*. Blackwell Scientific Publications, 1987.
- [26] R.G. Gilbert; S.C. Smith. *Theory of Unimolecular and Recombination Reactions*. Blackwell Scientific Publications, 1990.
- [27] G. Z. Whitten; B. S. Rabinovitch. *J. Chem. Phys.*, 38:2466, 1963.
- [28] T. Baer; W. L. Hase. *Oxford University Press*, 1996.
- [29] W. L. Hase. *Acc. Chem. Res.*, 31:659, 1998.
- [30] J. I. Steinfeld; J. S. Francisco; W. L. Hase. *Chemical Kinetics and Dynamics*. Prentice Hall, 1999.
- [31] K. Song; W. L. Hase. *J. Phys. Chem.*, 102:1292, 1998.
- [32] M. Quack; J. Troe. *Ber. Bunsenges. Phys. Chem.*, 78:240, 1974.
- [33] J. Troe. *J. Chem. Phys.*, 75:226, 1981.
- [34] J. Troe. *J. Chem. Phys.*, 79:6017, 1983.
- [35] J. Troe. *Chemical Reviews*, 103(12):4565, 2003.
- [36] J. Troe. *Ber. Bunsenges. Phys. Chem.*, 87:161, 1983.
- [37] J. Troe. *J. Chem. Phys.*, 66:4745, 1977.
- [38] J. Troe. *J. Chem. Phys.*, 66(11):4758, 1977.
- [39] R. G. Gilbert; K. Luther; J. Troe. *Ber. Bunsenges. Phys. Chem.*, 87:169, 1983.
- [40] C. Kachiani. *Modellierung des Einflusses der Molekülrotation auf die Kinetik thermischer unimolekularer Reactionen*. PhD thesis, Universität Karlsruhe, 2004.
- [41] N. J. B. Green; P. J. Marchant; M. J. Perona; M. J. Pilling; S. H. Robertson. *J. Chem. Phys.*, 96(8):5896, 1992.

- [42] R. G. Gilbert; S. C. Smith; M. G. T. Jordan; G. P. Knight. *UNIMOL program suite (Calculations for unimolecular and Recombination Reactions Available from the authors: School of Chemistry, Sydney University, NSW 2006, Australia or by e-mail to gilbert@chem.usyd.edu.au. 1994.*
- [43] M. Olzmann. *Phys. Chem. Chem. Phys.*, 4:3614, 2002.
- [44] D. Fulle; H. F. Hamman; H. Hippler; J. Troe. *J. Chem. Phys.*, 105(3):983, 1996.
- [45] K. Song; W.L. Hase. *J. Phys. Chem.*, 102:1296, 1998.
- [46] H. M. Keller; H. Floethmann; A. J. Dobbyn; R. Schinke; H. J. Werner; C. Bauer; P. Rosmus. *J. Chem. Phys.*, 105:4983, 1996.
- [47] B. Poirier; T. Carrington. *J. Chem. Phys.*, 116:1215, 2001.
- [48] D. Wang; J. M. Bowman. *Chem. Phys. Lett.*, 235:277, 1995.
- [49] G. W. Adams; Z. Zhao; R. W. Field. *J. Mol. Spectroscopy*, 160:11, 1993.
- [50] D. W. Neyer; X. Luo; P. L. Houston; I. Burak. *J. Chem. Phys.*, 98:5095, 1993.
- [51] D. W. Neyer; X. Luo; I. Burak; P. L. Houston. *J. Chem. Phys.*, 102:1645, 1995.
- [52] J. D. Tobiason; J. R. Dunlop; E. A. Rohlfing. *J. Chem. Phys.*, 103(4):1448, 1995.
- [53] F. Renth; F. Temps; A. Trölsch. *J. Chem. Phys.*, 118:659, 2003.
- [54] H. M. Keller; M. Stumpf; T. Schröder; C. Stöck; F. Temps; R. Schinke; H. J. Werner; C. Bauer; P. Rosmus. *J. Chem. Phys.*, 106:5359, 1997.
- [55] C. Stöck; X. Li; H. M. Keller; R. Schinke; F. Temps. *J. Chem. Phys.*, 106:5333, 1997.
- [56] J. D. Tobiason; J. R. Dunlop; E. A. Rohlfing. *Chem. Phys. Lett*, 235:268, 1995.

- [57] J. M. Bowman; J. S. Bittman; L. B. Harding. *J. Chem. Phys.*, 85:911, 1986.
- [58] H. J. Werner; C. Bauer; P. Rosmus; H. M. Keller; M. Stumpf; R. Schinke. *J. Chem. Phys.*, 102:3593, 1995.
- [59] L. N. Krasnoperov; E. N. Chesnokov; H. Stark; A. R. Ravishankara. *Proc. Combust. Inst.*, 30:919, 2004.
- [60] H. Y. Wang; J. A. Eyre; L. M. Dorfman. *J. Chem. Phys.*, 59:5199, 1973.
- [61] J. J. Ahumada; J. V. Michael; D. T. Osborne. *J. Chem. Phys.*, 57:3736, 1972.
- [62] H. O. Pritchard. *J. Phys. Chem.*, 92(26):7257, 1988.
- [63] A. F. Wagner. *J. Phys. Chem.*, 92(26):7259, 1988.
- [64] K. Song; L. Sun; W. L. Hase; S.Y. Grebenshchikov; R. Schinke. *J. Phys. Chem.*, 106:8339, 2002.
- [65] J. Hausschildt; J. Weiss; C. Beck; S.Y. Grebenshchikov; R. Düren; R. Schinke; J. Koput. *Chem. Phys. Letters*, 300:569, 1999.
- [66] A. J. Dobbyn; M. Stumpf; H. M. Keller; R. Schinke. *J. Chem. Phys.*, 104:8357, 1996.
- [67] A. Horowitz; C. J. Kershner; J. G. Calvert. *J. Phys. Chem.*, 86:3094, 1982.
- [68] A. D. Hansen; E. K. C. Lee. *J. Chem. Phys.*, 63:3272, 1975.
- [69] H. Hippler; N. Krasteva; F. Striebel. *Phys. Chem. Chem. Phys.*, 7:2077, 2005.
- [70] H. Hippler; N. Krasteva; F. Striebel. *Phys. Chem. Chem. Phys.*, 6(13):3383, 2004.
- [71] U. Brandt Pollmann; J. Weiss; R. Schinke. *J. Chem. Phys.*, 115:8876, 2001.
- [72] J. Qi; J. M. Bowman. *J. Chem. Phys.*, 105:9884, 1996.
- [73] C. Y. Yang; S. K. Gray. *J. Chem. Phys.*, 107:7773, 1997.
- [74] G. S. Whittier; J. C. Light. *J. Chem. Phys.*, 107(6):1816, 1997.

- [75] D. Wang; J. M. Bowman. *Chem. Phys. Lett.*, 235:277, 1995.
- [76] H. Zhang; S. C Smith. *J. Phys. Chem.*, 106:6129, 2002.
- [77] B. Kirmse; B. Abel; D. Schwarzer; S. Y. Grebenshchikov; R. Schinke. *J. Phys. Chem.*, 104:10398, 2000.
- [78] J. Weiss; R. Schinke. *J. Chem. Phys.*, 115:3173, 2001.
- [79] K. T. Kuwata; A. S. Hasson; R. V. Dickinson; E. B. Petersen; L. C. Valin. *J. Phys. Chem. A*, 109:2514, 2005.
- [80] N. Washida; S. Inomata; M. Furubayashi. *J. Phys. Chem. A*, 102:7924, 1998.
- [81] A. M. Schmoltner; P. M. Chu; R. J. Brudzynski; Y. T. Lee. *J. Chem. Phys.*, 91:6926, 1989.
- [82] J. Lee; J. W. Bozzelli. *J. Phys. Chem.*, 107:3778, 2003.
- [83] G. Inoue; H. Akimoto. *J. Chem. Phys.*, 74:425, 1981.
- [84] E. Delbos. *Application de la photolyse laser couplée à la fluorescence induite par laser à l'étude de la réactivité de radicaux de type vinoxyle*. PhD thesis, L'universite des Sciences et Technologies de Lille, 2004.
- [85] T. Oguchi; A. Miyoshi; M. Koshi; H. Matsui; N. Washida. *J. Phys. Chem. A*, 105:378, 2001.
- [86] K. T. Kuwata; K. L. Templeton; A. S. Hasson. *J. Phys. Chem. A*, 107:11525, 2003.
- [87] E. Delbos; P. Devolder; L. ElMaimouni; C. Fittschen; K. Brudnik; J. T. Jodkowski; E. Ratajczak. *Phys. Chem. Chem. Phys.*, 4(13):2941, 2002.
- [88] A. A. Plaenckaert; J. Doucet; C. Sandorfy. *J. Phys. Chem.*, 60:4846, 1974.
- [89] M. L. Morton; D. E. Szpunar; L. J. Butler. *J. Chem. Phys.*, 115:204, 2001.
- [90] D. Fulle; H. F. Hamman; H. Hippler; C. P. Jaensch. *Ber. Bunsenges. Phys. Chem.*, 101:1433, 1997.

- [91] C. Møller; M. S. Plesset. *Phys. Rev.*, 46:618, 1934.
- [92] M. Olzmann. *Private communication*.
- [93] N. Snider. *J. Chem. Phys.*, 80(5):1885, 1984.
- [94] J. Troe. *J. Chem. Soc. Faraday Trans.*, 90(16):2303, 1994.
- [95] B. Viskolcz. *Private communication*.
- [96] R. C. Reid; J. M. Prausnitz; B. E. Poling. *The Properties of Gases and Liquids*. McGraw - Hill, New York, 4th edn., 1987.
- [97] G Herzberg. *Molecular Spectra and Molecular Structure I. Spectra of Diatomic Molecules*. Krieger Publishing Company, Malabar, Florida, 2nd edn., 1989.

Acknowledgments

The investigations presented in this script are result of a team work and I am glad that I have now the opportunity to thank everybody who has contributed to these. First of all, I am greatly indebted to my Supervisor, Prof. Dr. H. Hippler, who is except a great scientist, also a very kind person. His profoundly optimistic attitude to research has encouraged me to carry on investigations in the fascinating field of chemical kinetics.

I owe my warmest gratitude to Dr. F. Striebel for the patience and professionalism, for editing this thesis, and most of all, for guiding me to start thinking in a global way on kinetic problems.

My special thanks to Prof. Dr. M. Olzmann for keeping an eye on the progress of this work and being available whenever I needed his advises as well as for the Master Equation analysis on the reaction of CH_2CHO with O_2 . The contribution of Dr. B. Viskolcz, who performed *ab initio* calculations on this are gratefully acknowledged as well. I am obliged to Dr. R. Schießl and Dr. A. Unterreiner for their interest in this work and the valuable hints.

I had the pleasure to work with several students who did their graduation work in this lab - thank you for the assistance and the helpful discussions. I want to thank all of my colleges, especially Mel, for their help, support, and for making my stay in Germany pleasant.

Dipl. Ing. P. Hibomvschi and Dipl. Ing. D. Kelly, as well as the co-workers from the technical and electrical workshops are thanked for their prompt assistance by all types of technical problems. Special tanks to Dipl. Chem. H. Brands for writing the program used to control the experiments.

Finally, I am greatly indebted to my family for their understanding, endless patience and encouragement.

Curriculum Vitae

Personal Details:

Name: Nikolina Kirilova Krasteva

Date of Birth: 09. 12. 1977

Place of Birth: Sofia, Bulgaria

Nationality: Bulgarian

Marital Status: Single

Education:

2001 - 2005: Ph.D., University of Karlsruhe, Germany
Supervisor: Prof. Dr. Horst Hippler

1996 - 2001: Master's Degree in Chemistry and Physics
Sofia University, Bulgaria

1991 - 1996: School Education
55 High School, Sofia, Bulgaria

Talks

1. **Laboratory of physical chemistry of combustion processes CRNS, Lille, France, November 15 - 28, 2004**

Influence of Non-Statistical Effects on the Rate Coefficient of the Thermal HCO/DCO Decomposition

2. **103 Symposium of the German Bunsen-Society for Physical Chemistry, Dresden, Germany, 20 - 22 May 2004.**

The Thermal Unimolecular Decomposition of HCO

Publications:

1. The thermal unimolecular decomposition of HCO: Effects of the state specific rate constant on the thermal rate constant
H. Hippler, N. Krasteva and F. Striebel, *Phys. Chem. Chem. Phys.*, **2004**, 6(13), 3383.
2. Reply to the 'Comment on "The thermal unimolecular decomposition of HCO: Effects of the state specific rate constant on the thermal rate constant"' by L. N. Krasnoperov
H. Hippler, N. Krasteva, F. Striebel, *Phys. Chem. Chem. Phys.*, **2005**, 7(9), 2077.
3. Rate coefficients and product yields of the OH + C₂H₄ reaction
H. Hippler, M. Klinger, N. Krasteva, S. Nasterlack, M. Olzmann, F. Striebel
European Combustion Meeting, **2005**
4. Rate Coefficients and Equilibrium Constant for the CH₂CHO + O₂ Reaction System
E. Delbos, C. Fittschen, H. Hippler, N. Krasteva, M. Olzmann, B. Viskolcz
(*J. Phys. Chem.*), **2005**.
5. The thermal unimolecular decomposition of HCO: Falloff Behaviour in Different Bath Gases and Isotope Effect
H. Hippler, N. Krasteva, F. Striebel (in preparation)
6. Reaction of OH + NO₂ + M: A new Falloff Analysis
H. Hippler, N. Krasteva, S. Nasterlack, F. Striebel (in preparation)